Characterizing the Thin-Film Response of Metal Phthalocyanine-Based OTFT Cannabinoid Sensors

Halynne Lamontagne, *B.A.Sc, B.Sc.*

Thesis submitted to the University of Ottawa in partial fulfillment of the requirements for the Doctorate of Philosophy in Chemical Engineering

Department of Chemical and Biological Engineering

Faculty of Engineering

University of Ottawa

PhD in Chemical Engineering (2025)

Chemical and Biological Engineering

University of Ottawa

TITLE:	Characterizing the Thin Film Response of Metal Phthalocyanine-Based OTFT Cannabinoid Sensors
AUTHOR:	Halynne Lamontagne, B.A.Sc. (Chemical Engineering), B.Sc. (Biochemistry)
SUPERVISOR:	Benoît H. Lessard & Adam J. Shuhendler
PAGES:	169

Abstract

Metal phthalocyanine (MPc)-based organic thin-film transistors (OTFTs) provide a potentially cost-effective solution to cannabis consumers, producers and regulators alike to detect and speciate Δ^9-tetrahydrocannabinol (THC) and cannabidiol (CBD) in both solution and vapor cannabis samples. This sensing response is driven by unique coordinating interactions with MPcs and cannabinoids in solution and thin films which cause a change in the device performance upon exposure. This thesis looked to further characterize and understand these interactions to inform optimization efforts for OTFT sensors using multiple approaches, including optimization of the channel and device architecture, and molecular tuning. Through the integration of device performance data and physical characterization techniques such as atomic force microscopy (AFM), grazing incidence wide-angle X-ray scattering (GIWAXS), and Raman spectroscopy, the interactions between cannabinoids and thin films of MPcs can be characterized and correlated to improved performance. Firstly, I investigated the effect of channel dimension and film thickness on the response of chloro aluminum phthalocyanine (Cl-AlPc) based OTFT sensors, where the film roughness and thickness were found to have the greatest influence on the sensing response. Following, I performed a series of axial phenoxylations to improve the performance of R-AlPc in OTFT cannabinoid sensors. The phenoxy-AlPc compounds were found to adopt different thin film motifs from Cl-AlPc that made them more responsive to THC and/or CBD. Finally, I investigated the sensing response of the air-stable, *n*-type molecule $(F_5PhO)_2$-F_{16}-SiPc to expand our library of sensing molecules and further studied its thin film structure. In this case, substitution of the hydrogen atoms with fluorines was detrimental to its sensing response. I conclude this thesis with my additional work on other projects related to thin film characterization, physical vapor deposition, and sensor integration in our group, and detail how my expertise has shaped our lab's knowledge on structure-property relationships of a variety of materials. As the push for the commercialization of OTFTs and OTFT-based sensors continues, establishing an understanding of the thin film and electronic properties of a range of materials remains essential.

Résumé

Les transistors à couches minces (« *organic thin-film transistors* », OTFTs) à base de phtalocyanines métalliques (MPc) offrent une solution potentiellement rentable aux consommateurs, aux producteurs et aux régulateurs de cannabis qui désirent détecter et distinguer le Δ^9-tetrahydrocannabinol (THC) et le cannabidiol (CBD) dans des échantillons de cannabis sous forme de vapeur et en solution. La détection de ces cannabinoïdes est stimulée par des interactions de coordination uniques entre ces derniers et les MPc, qui provoquent des changements dans la performance des dispositifs. Cette thèse vise à caractériser davantage ces interactions et à mieux les comprendre afin de mettre au point l'optimisation des capteurs à base d'OTFT en utilisant plusieurs approches, dont l'optimisation des dimensions de canal et le réglage moléculaire des MPc. À l'aide des données de performance des dispositifs et des techniques de caractérisation physique, telles que la microscopie à force atomique (« *atomic force microscopy* », AFM), la spectroscopie des rayons X aux grands angles en géométrie d'incidence rasante (« *grazing incidence wide-angle X-ray scattering* », GIWAXS) et la spectroscopie Raman, les interactions entre les cannabinoïdes et les MPc en couches minces peuvent être caractérisées et corrélées à une performance améliorée. D'abord, j'ai évalué l'effet des dimensions de canal et de l'épaisseur des films de chlorure de phtalocyanine d'aluminium (Cl-AlPc) sur la réponse des capteurs à base d'OTFT. L'épaisseur et la rugosité des films avaient la plus grande influence sur la performance des capteurs. Par la suite, j'ai étudié une série de phénoxylations axiales afin d'améliorer la performance des R-AlPc dans les capteurs à base d'OTFT. Les motifs des couches minces de composés d'AlPc phénoxylés étaient différents de ceux du Cl-AlPc, de manière à les rendre plus sensibles au THC et/ou au CBD. Finalement, j'ai fabriqué des capteurs à base de $(F_5PhO)_2$-F_{16}-SiPc, une molécule de type N stable à l'air ambiant, afin d'élargir les options de molécules pouvant être intégrées dans des capteurs, ainsi que pour étudier sa structure en couche mince. Dans ce cas, la substitution des atomes d'hydrogène par des atomes de fluor a engendré une perte de la réponse des capteurs. Je conclue cette thèse avec mes travaux sur d'autres projets reliés à la caractérisation de couches minces, au dépôt physique en phase vapeur et à l'utilisation de capteurs dans

notre groupe de recherche, ainsi qu'une explication de comment mon expertise a contribué aux connaissances de notre laboratoire en ce qui concerne les relations entre la structure et les propriétés de divers matériaux. Alors que la commercialisation des OTFT et des capteurs à base d'OTFT se poursuit, il demeure essentiel d'établir une meilleure compréhension des propriétés électroniques de plusieurs matériaux.

Acknowledgments

I would first like to thank my supervisors, Benoît Lessard and Adam Shuhendler, for being supportive mentors and leaders throughout my undergraduate and graduate research career. Benoît rejecting me from my first co-op position lit a fire and made me want to prove him wrong, and I hope I've done that over the last six years. I am truly lucky to have had both Benoît and Adam on my team, they have guided me with compassion and understanding while pushing me to overcome personal challenges and become a successful researcher and leader in our group. But apart from the professional, I am just lucky to have worked for and with two amazing people for the last six years, and to work in the positive and supportive environments they have cultivated in their groups.

I also want to thank my family – first, my parents, Lisa and Richard. Completing 10 years of school so far from home was difficult, but you always answered my phone and video calls, listening when I cried and cheering when I succeeded. You encouraged me to keep going, to be kind to myself, and always believed that I could make it through. My sisters, Joelle, Bryn and Cassidy – I love you weirdos, but you sure keep me humble. I appreciate the love and support, even if it's always delivered via a sarcastic remark. It's us four little women against the world forever, I'll always have your backs like you've had mine.

My work family that has kept me sane through the years – Kaitlin, May, Rose, Joe, Zach, Vittoria, Sophia, Laura, Mel, Ben, Sam, and Andre. I will forever cherish the numerous office gossiping sessions where I divulged too much Halynne/Oxbow lore. My office yapping prowess is truly only rivalled by Joe and Kaitlin, but I love that everyone attempted to keep up. But through our many hours together growing deaf to the background noise of cryo pumps, I have also become a better researcher and person from spending time with you all.

My friends, Bri, Jack, Natalie, Jessie, Ashley, and Tamz – you are all the smartest, kindest, and weirdest people I know. Thank you so much for befriending that loud co-op student in 2019 and giving her an iconic nickname (my very first nickname ever). Your friendship has been the easiest and most meaningful of my life, and I wouldn't have made it through my PhD without being able to decompress and have fun with all of you.

Table of Contents

List of Figures

List of Tables

List of Key Abbreviations

AFM	Atomic Force Microscopy
BGBC	Bottom-Gate Bottom-Contact
CBD	Cannabidiol
Cl-AlPc	Chloro Aluminum Phthalocyanine
CuPc	Copper Phthalocyanine
CVD	Chemical Vapor Deposition
GIWAXS	Grazing Incidence Wide Angle X-Ray Scattering
HOMO	Highest Occupied Molecular Orbital
LUMO	Lowest Unoccupied Molecular Orbital
MPc	Metal Phthalocyanine
MOSFET	Metal-Oxide Semiconductor Field-Effect Transistor
NEXAFS	Near Edge X-Ray Absorption Fine Structure
NMR	Nuclear Magnetic Resonance
OLED	Organic Light-Emitting Diode
OPV	Organic Photovoltaic
OTFT	Organic Thin Film Transistor
PVD	Physical Vapor Deposition
R_2-SiPc	Silicon Phthalocyanine
STXM	Scanning Transmission X-Ray Microscopy
TERS	Tip-Enhanced Raman Spectroscopy
THC	Δ^9-tetrahydrocannabinol
UPS	Ultraviolet Photoelectron Spectroscopy
XRD	X-Ray Diffraction
ZnPc	Zinc Phthalocyanine

List of Key Variables

C_i	Dielectric Capacitance
E_F	Fermi Level
g_m	Transconductance
L	Channel Length
N	Defect Density
I_{On}	On Current
$I_{On/Off}$	On-Off Current Ratio
I_{SD}	Source-Drain Current
R	Dichroic Ratio
R_c	Contact Resistance
R_T	Total Resistance
S	Subthreshold Swing
V_{GS}	Gate-Source Voltage
V_{SD}	Source-Drain Voltage
V_T	Threshold Voltage
W	Channel Width
μ	Field-Effect Mobility
μ_e	Electron Mobility
μ_h	Hole Mobility

Chapter 1: Introduction

1.1 Organic Electronics and Organic Thin-Film Transistors

The field of organic electronics has seen rapid growth in recent years due to their unique properties and potential for integration into a wide range of innovative applications. These technologies rely on cost-effective, carbon-based semiconductors that can be processed under relatively mild conditions. As a result, organic electronics are increasingly being adopted in both industry and consumer markets, notably in devices such as organic light-emitting diodes (OLEDs), organic photovoltaics (OPVs) and organic thin film transistors (OTFTs). The drive to find alternatives to silicon-based electronics, seeking lower-cost, energy-efficient, and more globally accessible options, has further accelerated technological progress. Organic semiconductors are particularly well-suited to fabrication on flexible and lightweight substrates, enabling the development of bendable displays[1,2], wearable medical devices[3], and point-of-source sensors.[4] OTFTs, in particular, play a critical role in advancing the field, as they enable the construction of complex circuits composed of multiple transistors essential for logic-based displays and sensors.

OTFTs are solid-state devices that consist of four main components: a gate electrode, an insulating dielectric layer, a thin-film semiconducting layer, and source-drain electrodes. These components can be arranged in four common architectures (**Figure 1.1**). The semiconductor, often a conjugated small molecule or polymer, can be deposited by physical or chemical vapor deposition (PVD or CVD), or by solution processing techniques like spin coating or blade coating. Depending on the material and processing technique, these semiconductor films can be 2 – 500 nm thick, with most small molecule films finding optimal performance between 10 – 100 nm.[5] A voltage bias is applied across the semiconducting material at the source and drain electrodes (V_{SD}), and current flow across the channel (I_{SD}) is controlled by the voltage bias across the source and gate electrodes (V_{GS}) (**Figure 1.1a**). When the V_{GS} is applied, the dielectric is polarized and causes charge to accumulate at the interface between the dielectric and the semiconductor. When the threshold voltage (V_T) is exceeded, the semiconductor is excited and charge travels from the source to the drain, turning the device “on”. In a *p*-

type device, holes are transported through the semiconductor, and in an *n*-type device the charge carriers are electrons. If the device carries both holes and electrons, it is classified as ambipolar. There are many comprehensive review articles if readers would like more information on OTFT architectures, materials, or operation basics.[6–11]

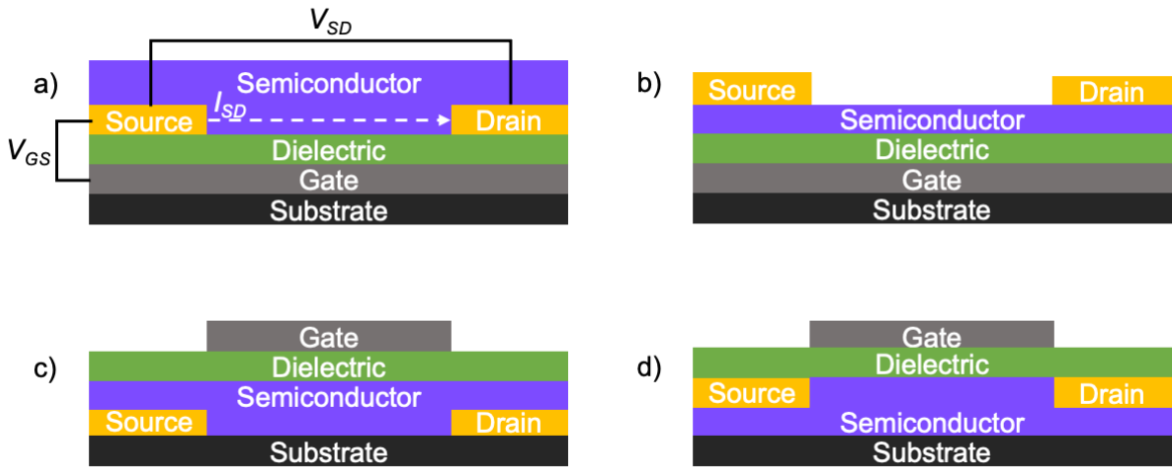

Figure 1.1 *Common OTFT device architectures, (a) bottom-gate, bottom-contact (BGBC), (b) bottom-gate, top-contact (BGTC), (c) top-gate, bottom-contact (TGBC), and (d) top-gate, top-contact (TGTC). Applied voltages (black solid lines) and measured current (white dashed arrow) during normal operation are shown.*

1.1.1 Operation and Electrical Characterization of OTFTs

To characterize an OTFT, output and transfer curves are recorded, and from these curves a variety of performance metrics can be derived. To measure an output curve, the V_{GS} is fixed while the V_{SD} is varied, and the I_{SD} is measured (**Figure 2a**). From these curves, the linear and saturation regimes can be determined. In the linear regime, $|V_{SD}| < |V_{GS} - V_T|$, and I_{SD} rapidly changes with V_{SD} as holes or electrons are mobilized. In the saturation regime, $|V_{SD}| > |V_{GS} - V_T|$, and the I_{SD} plateaus as all charge carriers have been mobilized. To generate a transfer curve, the V_{SD} is kept constant while the V_{GS} is varied while measuring I_{SD} (**Figure 2b**). From this curve, the V_T can be visualized, and a variety of performance parameters can be extracted to assess the overall performance of the OTFT and the semiconductor.

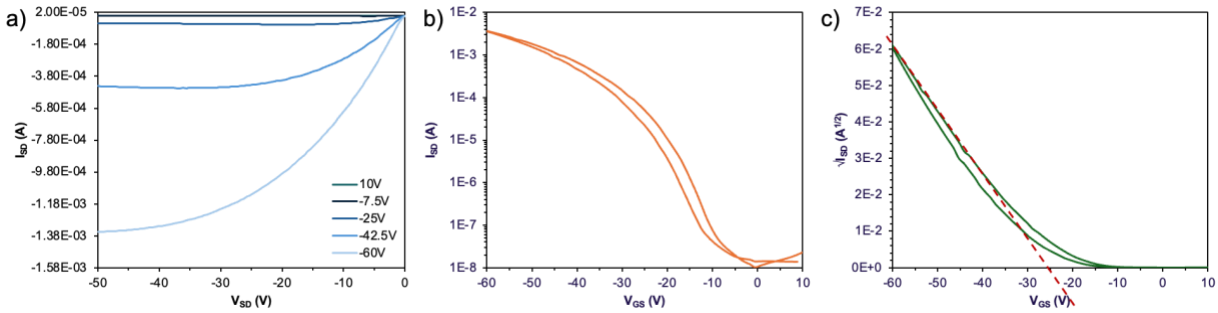

***Figure 1.2**. Sample a) output curve, b) transfer curve and the c) $\sqrt{I_{SD}}$ vs V_{GS} plot for a p-type OTFT, showing the linear fit for μ_{sat} and V_T determination.*

The performance of an OTFT is typically modelled as a metal-oxide semiconductor field-effect transistor (MOSFET) to determine its field-effect mobility (μ) and V_T. This model is often not accurate for the operation of organic devices, especially those with poor performance, due to presence of charge traps and high contact resistance in OTFTs which lead to unideal charge transport behavior.[12] While more advanced models have been developed,[12,13] data extraction can be more difficult while inconsistencies remain, so the MOSFET model remains widely used the field to approximate key performance parameters.

In the linear region, the μ can be calculated by rearranging Equation 1.1, to arrive at Equation 1.2.

$$I_{SD} = \frac{\mu C_i W}{L}\left[(V_{GS} - V_T)V_{SD} - \frac{V_{SD}^2}{2}\right] \quad (1.1)$$

$$\mu_{lin} = \frac{L}{W C_i V_{SD}}\left[\frac{\partial I_{DS}}{\partial V_{GS}}\right] \quad (1.2)$$

Where L and W are the channel length and width, C_i is the capacitance of the dielectric, calculated by $C_i = \frac{\varepsilon_0 \varepsilon_r}{d}$, where d is the dielectric thickness, ε_0 is the permittivity of free space, and ε_r is the dielectric constant of the dielectric material. This calculation assumes a perfectly linear dependence of I_{SD} through this region, with a constant μ. This is not common for OTFTs, where a voltage-dependent μ is often observed due to the disorder in the film.[10,12,14,15]

The μ in the saturation region can be calculated by arranging Equation 1.3 to yield Equation 1.4.

$$I_{SD} = \frac{\mu C_i W}{2L}(V_{GS} - V_T)^2 \quad (1.3)$$

$$\mu_{sat} = \frac{2L}{WC_i}\left[\frac{\partial\sqrt{I_{SD}}}{\partial V_{GS}}\right]^2 \quad (1.4)$$

As this calculation assumes a linear dependence on $\sqrt{I_{SD}}$ over the saturation regime, the slope of $\sqrt{I_{SD}}$ vs V_{GS} can be used to calculate μ, and the V_T can be extracted from the x-intercept (**Figure 1.2c**). Other useful parameters to calculate include the transconductance, g_m, which is a measure of the rate of current uncorrected for capacitance or channel architecture, as shown in Equation 1.5.

$$g_m = \frac{\partial I_{SD}}{\partial V_{GS}} \quad (1.5)$$

Transconductance is often a more accurate measure of the rate of charge transport because it does not rely on a model, like the MOSFET model, to fit the often imperfect data from OTFTs. However, since it is not corrected for system differences like L, W and C_i, it can be difficult to make comparisons between different devices and publications. It is therefore a measurement of the efficiency of the entire system, not only the semiconductor.

Another useful parameter is the subthreshold slope, which is taken at the point where current begins to flow but below the V_T in the log-plot of the transfer curve. This value can be used to calculate the defect density, N, of an OTFT, which is indicative of the number of charge traps that are filled before charge can continuously flow and the device turns “on”. This subthreshold slope can be affected by the film itself, where defects or impurities can act as charge traps, and the environment that the testing is performed in. As the subthreshold slope decreases, and the rate at which charge moves through the film decreases, the calculated defect density will increase, as shown in Equation 1.6.

$$N = \left(\frac{Sq}{kTln(10)} - 1\right)\left(\frac{C_i}{q}\right) \quad (1.6)$$

Where S is the subthreshold swing, the inverse of the subthreshold slope, q is the electronic charge, k is the Boltzmann constant, and T is the temperature.

An ideal OTFT will have a high ratio between its current in its on and off states ($I_{On/Off}$), and will quickly switch between these states at a low voltage, resulting in a high subthreshold slope and a low V_T. This would indicate efficient charge transport through the semiconductor with limited loss of charge through defects. This is often not the case

in organic materials, and hysteresis can be observed during characterization, where the device does not desaturate well and a difference in the current is observed while saturating and desaturating the device. Depending on the ultimate application of the OTFT, there are different performance targets. For example, for integration in complementary metal-oxide-semiconductor (CMOS) inverters, an OTFT needs a V_T near 0 V, and the *p*-type and *n*-type mobilities need to match closely.[16] For biological sensor applications, low voltage operation is key while maintaining high switching speeds and a low noise threshold.[17,18] Ultimately, the largest challenge for OTFT commercialization is their stability and consistency, as repeated operation can cause bias stress, where charge carriers become trapped in the conducting channel, leading to a shift in V_T over time.[16] The final circuit or sensor is often intolerant to these shifts, so materials and device architectures that minimize these shifts are desired.

The electrical performance of OTFTs is dependent on many factors, including the semiconductor-dielectric interface properties,[19] the charge injection efficiency,[20,21] device geometry,[7,22] and the overall semiconductor morphology.[23,24] The orientation and order of the molecules through the semiconductor film will determine how well charges are able to travel through the material. In general, if the molecules are well-aligned and tightly packed, charges will be able to more efficiently pass through the material, leading to higher electrical performance. Film properties can be engineered by controlling the surface energy and deposition conditions of the semiconductor film during device fabrication, affecting grain size and crystal orientation.

1.2 Metal Phthalocyanines as Organic Semiconductors

1.2.1 Chemical Properties of Metal Phthalocyanines

Metal and metalloid phthalocyanines (MPcs) are a class of conjugated macrocyclic molecules with a characteristically vibrant blue, purple or green color. They were historically used as commercial dyes and pigments after their discovery in 1907 and first patent in 1929.[25–27] These molecules consist of four isoindole rings joined together through nitrogen linkages around a central metal. This conjugated ring structure extensively delocalizes the π-electrons, which gives the molecule its interesting electrical and optical properties that are well-suited for organic electronic applications, including

their use as semiconducting layers in OTFTs[11,28] and OPVs.[29,30]. Additionally, MPcs are exceptionally thermally and chemically stable, and are inexpensive to manufacture on the ton-scale. They can also be easily chemically modified through substitutions at the peripheral[31] or axial positions,[32–39] or by substituting the central metal (**Figure 1.3**). This structural versatility enables the tuning of their physical properties for specific applications to achieve greater solubility,[40] new crystal polymorphs, desirable film morphologies,[32,41,42] or improved electronic properties.[31,43] The thermal stability of MPcs enables thin film fabrication by physical vapor deposition (PVD), and chemical modification can confer solubility that enables solution processing techniques, making MPcs a flexible material for efficient device fabrication.

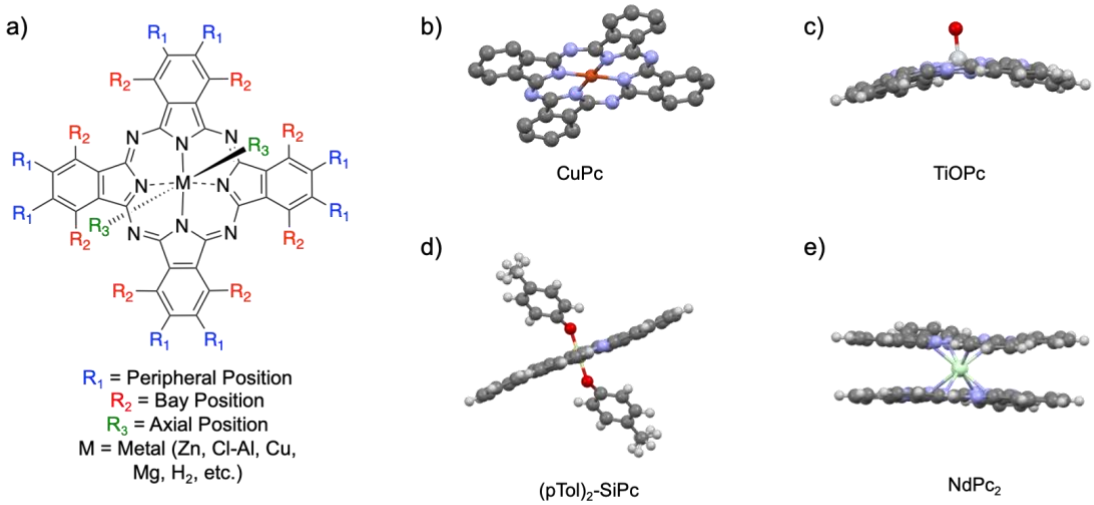

Figure 1.3. *a) The general chemical structure of a metal phthalocyanine, and the crystal structures of common phthalocyanines with different central metal valencies, including b) CuPc (CCDC# 219250),[44] c) TiOPc (CCDC# 1993686),[45] d) (pTol)$_2$-SiPc (CCDC# 1824913)[46] and e) NdPc$_2$ (CCDC# 2016006).[47]*

The central metal of MPcs influences its molecular geometry and crystal packing, as illustrated in **Figure 1.3b-e**. Metals with a smaller central radius or valency, such as divalent copper, zinc and cobalt (CuPc, ZnPc and CoPc, respectively) fit well in the center of the Pc ring and form a planar molecular geometry.[44,48] Tetravalent small metals like silicon can form two axial connections, and the Pc ring is still planar, but the ring can experience torsion or strain due to the presence of larger axial groups.[46] Larger, higher

valency metals like aluminum and titanium are still held by the ring but sit slightly outside, forming umbrella or cone-shaped molecules with a single axial connection (Cl-AlPc and TiOPc, most commonly).[45] Very large metals, like lutetium and neodymium can still be held by the Pc ring, but form large complexes ($LuPc_2$ and $NdPc_2$, respectively).[47] As such, the central metal and the presence or choice of axial substituent has a large influence on the molecular geometry of the MPc, and the resulting crystal and thin film structure.

1.2.2 Crystal Polymorphs of Metal Phthalocyanines

The thin film packing geometry of MPcs is highly variable and influenced by a variety of external factors, due to the reliance on weaker forces like van der Waals interactions that govern the formation of crystal polymorphs, in contrast to covalent or ionic interactions that often govern the crystal formation of inorganic materials. As such, it is important to understand the different polymorphic forms of different MPcs that are possible, as the structure they adopt will greatly influence charge transport. Planar, divalent MPcs typically form stacks that arrange in a herringbone packing pattern (**Figure 1.4**).[44] The molecules in this structure can have different phase angles relative to each other and the surface, characterizing the structure most commonly as an α or β geometry. Additional geometries are sometimes possible, though they are often not stable or achievable without heat, solvent exposure, or chemical modification.[49] Ten different polymorphs have been identified for CuPc in particular, with full crystal structures described for α, β, ε, and γ.[49] Non-planar MPcs, like Cl-AlPc, form face-to-face π-stacks, which can vary in their arrangement relative to one another depending on the size of the axial substituent (**Figure 1.4c**).[50]

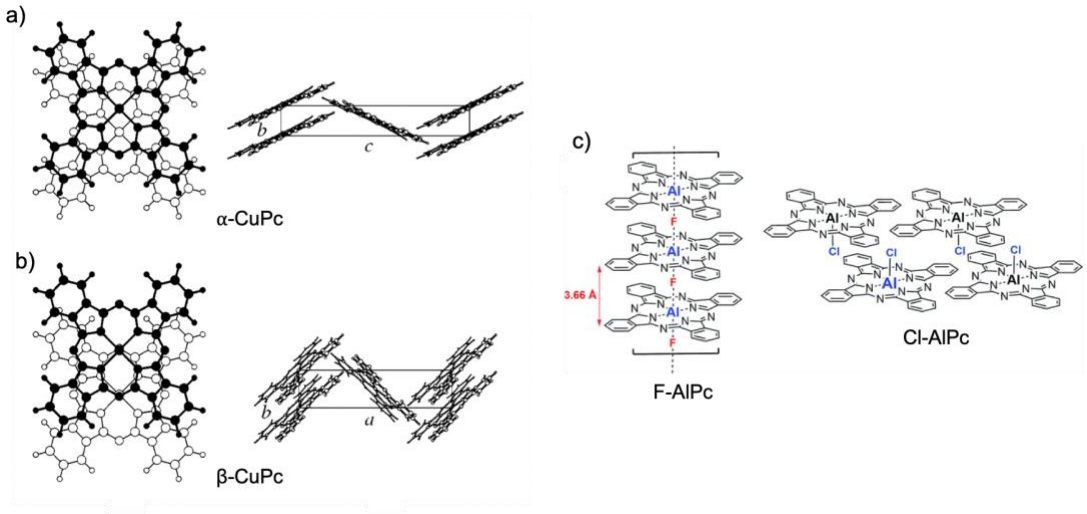

Figure 1.4. *Crystal polymorph structures of planar phthalocyanines a) α- form and b) β- form. Reproduced with permission from Reference [49] Copyright© Wiley 2004. Crystal packing structures of non-planar phthalocyanines c) F-AlPc and Cl-AlPc. Reproduced with permission from Reference [50] Copyright© Royal Society of Chemistry 2015.*

Each polymorph will have a different degree of π-orbital overlap, and angle and distance between adjacent molecules, which ultimately influences their electrical performance. Polymorphs with a higher degree of π-electron overlap and multidimensional electron coupling experience higher conductivity.[51] This is easily demonstrated by α-CuPc and β-CuPc; the former has a tilt angle of 65° and the latter a tilt angle of 45°, implying a greater π-electron overlap in α-CuPc, corresponding to the higher recorded mobility of α-CuPc.[48,52] This reaffirms the importance of the ability to control and identify the molecular rearrangement of MPc films for optimization of OTFT performance.

1.2.3 Optical and Electrical Properties of Metal Phthalocyanines

An important influencing factor over the performance of an OTFT is the charge injection efficiency between the source-drain electrodes and the semiconductor. This is governed largely by how well the work function of the metal electrodes matches the frontier molecular orbitals of the semiconductor material, as the energy-level misalignment between the two forms the energy barrier for charge carrier injection across this interface.[53,54] In the case of *p*-type materials, the highest occupied molecular orbital (HOMO) should align well with the Fermi level (E_F) of the metal to promote hole injection, and in the case of an *n*-type material, the lowest unoccupied molecular orbital (LUMO)

should align to promote electron injection. By properly identifying the HOMO and LUMO of the semiconductor materials, we can choose an appropriate metal electrode that will promote charge injection and reduce contact resistance, R_c. Contact resistance not only negatively affects device performance by reducing the current, but also limits the ability to accurately model and analyze OTFTs.[22,53] When $R_c \neq 0$, the transfer characteristics of an OTFT become nonlinear and the μ becomes V_{GS}-dependent. As previously mentioned, the linearity of OTFT transfer characteristics is a central assumption of the MOSFET model that is commonly used to extract both μ and V_T, so with a R_c-dominated OTFT, this model becomes less suitable.[12,13,53] Common strategies to improve the energy alignment in an OTFT and reduce R_c include using a self-assembled monolayer (SAM) on the electrode layer or using an interlayer to tune the E_F of the electrodes.[55]

HOMO/LUMO identification for semiconductor materials, like MPcs, can be approximated through a combination of ultraviolet-visible (UV-vis) absorption spectroscopy to determine the band gap energy (E_{bg}) and cyclic voltammetry to determine the HOMO by the oxidation onset potential. The HOMO and LUMO can also be calculated directly by photoelectron spectroscopy (PES) techniques. The UV-vis absorption spectrum of MPcs share the same general features, with two strong absorption bands: the B-(Soret) band in the UV region of 280-350 nm, and the Q-band in the visible region between 550-750 nm (**Figure 1.5**).[56,57] The UV-vis spectrum of MPcs in solution will usually be sharp and well-resolved if the material is sufficiently soluble, however the location of the peaks may shift due to solvent-induced aggregation.[57] Solid state UV-vis absorption can often experience peak broadening, but will also show the effects of thin-film packing that are not visible in solution.[58] Generally, the B-band shows changes in the orbital overlap between the phthalocyanine ring and the central metal, indicative of π-*d* transitions, with peaks at lower wavelengths suggesting π^*-*d* transitions.[59] The Q-band is responsible for the bright blue-green color of MPcs and is indicative of π-π^* excitations. All Q-bands of MPcs experience characteristic Davydov splitting due to molecular interactions between adjacent molecules both in and out of solution.[60] The largest peak in the Q-band is assigned to the π-π^* transition of the phthalocyanine macrocycle, while the smaller, lower energy peak has been explained as a second π-π^* transition due to metal out-of-plane bonding.[59] Molecular substitutions at the axial, peripheral, or metal

centre of the MPc can influence the UV-vis spectral properties, shifting existing peaks or generating new ones.

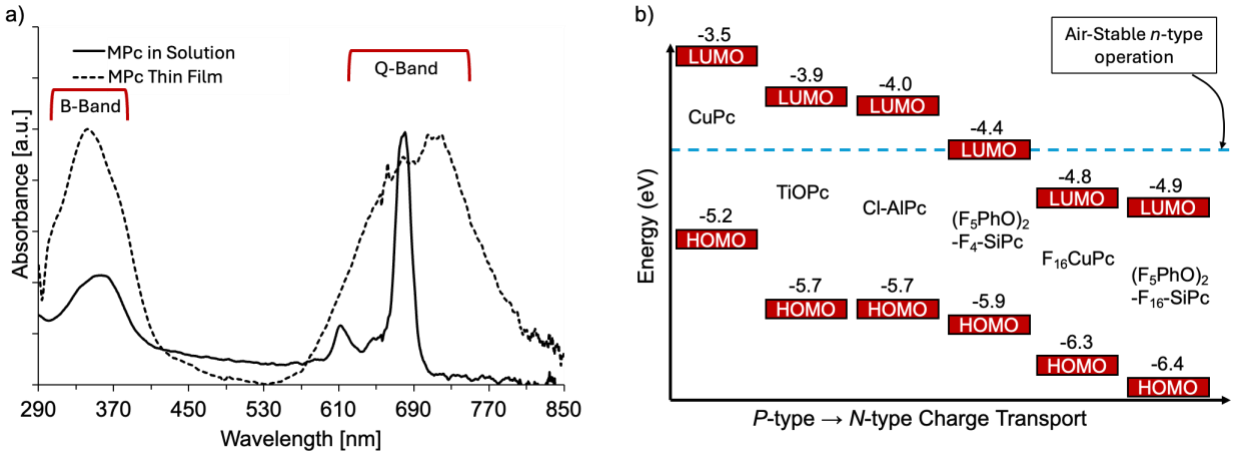

***Figure 1.5**. a) Representative UV-vis absorption spectra of a metal phthalocyanine thin film and in solution, indicating the characteristic B-band and Q-bands. b) HOMO-LUMO energy diagrams of a series of common and relevant metal phthalocyanines, including CuPc,[61] TiOPc,[62] Cl-AlPc,[50] $(F_5PhO)_2$-F_4-SiPc,[63] F_{16}CuPc,[61] and $(F_5PhO)_2$-F_{16}-SiPc.[63]*

The onset of the Q-band can be used to determine the E_{bg} of MPcs, and for most, this is in the range of 1.2 to 3.5 eV, depending on the central metal and any other axial or peripheral substituents. The position, or energy, of the frontier molecular orbitals will determine the majority charge carrier type. Most MPcs are *p*-type, or hole conducting materials. A few MPcs are *n*-type by nature of their metal centre, including R_2-SiPcs[64] and R_2-SnPcs,[42,65,66] though they are not necessarily stably electron conducting in air due to the tendency for oxygen *p*-doping when the LUMO of the material is higher than the oxidation energy of air, at -4.0 eV. The addition of electron-withdrawing peripheral substituents can cause a downward shift in the LUMO and change the majority charge carrier type from holes to electrons (*p*-type to *n*-type) or enable air-stable electron transport in *n*-type materials (**Figure 1.5b**). An example of this is peripheral fluorination, which has been employed in the case of CuPc, ZnPc, CoPc, and FePc to synthesize F_{16}CuPc, F_{16}ZnPc, F_{16}CoPc and F_{16}FePc, which successfully transport electrons and achieve electron mobilities (μ_e) from 10^{-6} to 10^{-2} cm^2/Vs.[67] In recent work, different degrees of peripheral and axial fluorination of R_2-SiPcs were investigated, with the fully fluorinated derivative $(F_5PhO)_2$-F_{16}-SiPc achieving full air stability and a high electron

mobility of 10^{-2} cm^2/Vs.[31,63] From this work, it has been demonstrated that a maximum LUMO of -4.4 eV is required for air stable electron transport in OTFT applications.[63]

1.2.4 Fabrication of Metal Phthalocyanine OTFTs and Influence on Performance

The thermal stability of MPcs enables film fabrication by PVD. Most MPcs readily sublime near ~400°C under rough vacuum, which is relatively mild. PVD processes involve the heating of a source (boat, crucible, etc.) in a chamber held under vacuum pressure (< 10^{-5} Torr), where the material sublimes and forms a plume, ultimately colliding with the substrate held above. Sublimed molecules can adsorb onto the surface either as layers, islands, or a combination of both, depending on the strength of the intermolecular and surface forces.[68] As the molecules are adsorbed, they can move on the surface to form islands, which occur when the intermolecular forces between adsorbed atoms, or adatoms, are stronger than their attraction to the surface.[69] As islands grow, their coordination energy increases, promoting further island growth.[70] The growth of MPc films proceeds through a combination of island and layer-by-layer growth, where the first few monolayers are deposited nearly completely on the surface due to the high attraction to the surface, then the film continues to grow as 3D islands as the coordination forces of the islands become dominant.[68,71] Control over the deposition rate and substrate temperature at this stage can influence nucleation site formation and density, island growth and adatom migration, and the roughness of the final film.

Typically, substrate temperatures between 30-180°C are used to give MPc films with larger grains and smaller grain boundaries, which are preferable for OTFTs. However, this type of morphology may not be ideal for sensor performance, which is explored in **Chapters 2** and **3** of this thesis. Higher temperatures provide more energy for rearrangement during deposition, promoting island migration and the diffusion of smaller islands into larger, more well-aligned islands that lead to the formation of much larger grains with a more uniform orientation.[70] In addition to substrate temperature, the deposition rate can be changed to alter the nucleation density. A higher deposition rate leads to kinetically dominated film growth, increasing the number of nucleation points and leading to smaller and denser crystallites and a more amorphous film. Decreasing the

deposition rate allows for more time for incoming molecules to migrate to a thermodynamically preferable position or orientation, often resulting in a lower nucleation density, larger crystallites, and fewer grain boundaries. Consequently, low rates of 0.05 – 1 Å/s are often used for MPc film fabrication to give films with large crystallites, favorable molecular packing, and higher overall crystallinity, which generally leads to greater OTFT performance. The dynamics and influence of deposition rate and temperature on ZnPc films are illustrated in **Figure 1.6**, where larger crystallites are formed at higher temperatures and lower rates, and very small grains are observed at higher deposition rates and lower temperatures.[72]

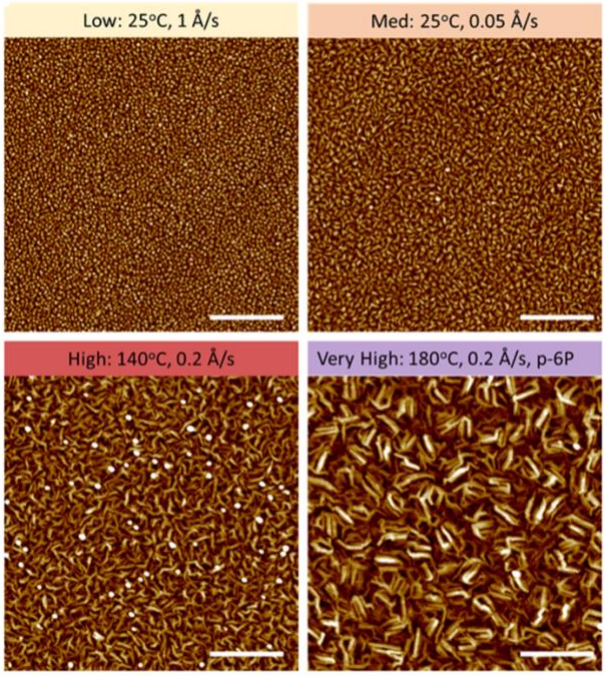

Figure 1.6. *Effect of deposition rate and deposition temperature on the morphology of ZnPc films, characterized from low to very high relative crystallinity. Scale bars represent 500 nm. Reproduced with permission from Reference [72] Copyright© Springer Nature 2023.*

Another method to control or influence the film morphology beyond deposition optimization is through the control of the surface chemistry, often through the use of self-assembled monolayers (SAMs).[73] SAMs are a popular strategy to change the surface energy and polarization, and to reduce surface defects to promote improved nucleation. Organosilanes are a commonly used class of SAMs that can be easily bonded to the surface of Si/SiO_2 substrates by chemisorption on the oxide surface.[74] These

compounds have a reactive head group that binds to the substrate, and an aliphatic backbone that reduces the substrate surface energy and interacts directly with the semiconductor, affecting its morphology and OTFT performance. This reduction in surface energy increases the hydrophobicity of the surface, matching more closely with the MPc and leading to improved film formation.[75] Octyltrichlorosilane (OTS) specifically is used throughout this thesis, as it has been demonstrated to yield high-performing OTFTs.[76]

1.3 Thin Film Characterization of Metal Phthalocyanines

Thin film morphological characteristics of small molecules that influence device performance include molecular geometry, crystal packing and defects, crystallite size and grain boundaries. Each of these film properties occur at different size scales, as illustrated in **Figure 1.7**, that require different analytical techniques. MPcs in particular can adopt different polymorphs and molecular orientations within the same film that can influence their overall performance. For applications in OTFTs, it is important to characterize the nm-scale morphologies over the entire μm-scale channel area, as it is the interaction of the different length scales that ultimately influences device performance. The preservation of molecular scale orientations and textures over larger film areas is what makes these devices functional, while ultimately complicating their characterization. Commonly, X-ray diffraction (XRD) or scattering techniques can be useful to probe and identify many of these molecular-scale packing structures, however these techniques often only identify crystalline features, when MPc films are polycrystalline or amorphous. To compliment these techniques, X-ray absorption or other microscopy techniques can be used in combination to get a more comprehensive picture of the nm- and μm-scale film morphology.

1.3.1 X-Ray Based Characterization of MPc Films

X-rays are particularly well-suited for the characterization of thin films used in OTFTs, as their wavelengths are on the order of the physical features that are relevant to device performance (hard X-rays: 0.01 – 0.3 nm; soft X-rays: 0.3 – 10 nm).[24] One can probe bond lengths, molecular packing, or grain size and orientation by selecting the proper beam energy, incident angle, and detector. A combination of X-ray diffraction,

scattering, and spectroscopic techniques have been used and are well-understood to characterize the underlying polymorphic and morphological behavior of both small molecule and polymer-based OTFTs.

Lab-scale X-ray sources are most commonly used in powder X-ray diffraction (PXRD), and this is a very useful technique to quickly screen multiple thin film samples to obtain information like *d*-spacing and relative diffraction intensity.[77] An X-ray beam is directed at the sample, and the constructive interference between the scattered X-rays from the atoms in the sample make up the diffracted signal that is collected on a point detector, according to Bragg's equation,[78] at different X-ray incident angles (2θ). Small molecule thin films are polycrystalline and weakly diffracting, which limits the information that can be gathered from most tabletop PXRD equipment. The resolution can be improved in the application of thin films by using grazing-incidence XRD (GIXRD), where the X-ray beam is directed at the sample at a low angle of incidence, the critical incident angle, focusing the beam to hit the surface of the film where the X-rays are totally reflected.[77] This geometry can improve the quality of the data collected for thin films, and depending on the detector set up, both in-plane and out-of-plane information could be collected. However, without a high-energy, focused beam, the information from GIXRD is still only enough to suggest a thin-film polymorph and more is needed to assign specific plane orientations and determine film texture, which can play a large role in OTFT performance.

Synchrotron-based X-ray techniques utilize X-ray beams with high flux and intensity, which is useful for weakly scattering organic thin films. Notably, synchrotron radiation is also highly polarized and is able to be tuned to a wide range of energies specific for the application and material.[79] Synchrotron radiation is fast-pulsing (tens of picoseconds), and the end stations are also equipped with rapid, high-quality detectors that allow for the collection of large amounts of data that would be unachievable on a lab-scale machine. Additionally, the superior optics at synchrotron facilities can allow for a beam focus down to the ~20 nm scale, enabling scanning microscopy to measure features in the 50 nm – 1 μm range. X-ray beam polarization also allows for the investigation of the dichroic behaviour of organic molecules to measure bulk film

molecular orientation in absorption spectroscopy. **Figure 1.7** depicts a series of synchrotron X-ray techniques, and the thin film features they are used to investigate.

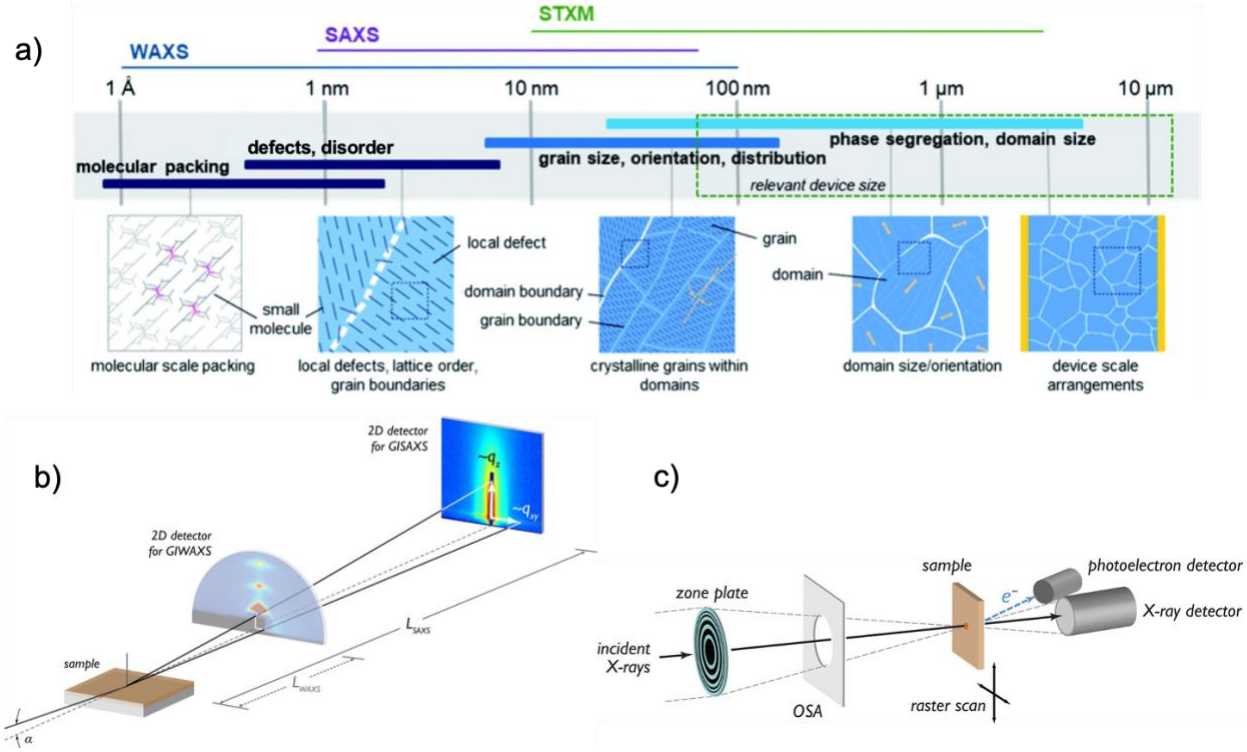

Figure 1.7. *a) Size scales, structural features, and relevant synchrotron X-ray characterization techniques for small molecule thin films. Reproduced with permission from Reference [68]. Copyright© Royal Society of Chemistry 2021. Schematic diagrams of b) GIWAXS and GISAXS, and c) STXM. Reproduced with permission from Reference [24]. Copyright© American Chemical Society 2012.*

Grazing-incidence wide-angle X-ray scattering (GIWAXS) works similarly to PXRD and GIXRD; a high-energy X-ray beam is directed onto a thin film sample at a low angle of incidence, and the constructive interference diffraction signals are collected on a large, 2D detector positioned close to the sample (**Figure 1.7b**). The position of the detector allows for the collection of wide-angle data ($2\theta > 5°$) which provides information about lattice spacing, crystallite orientation and alignment, and thin film texture when compared against the single-crystal structure of the material. Data is collected along both the q_z and q_{xy} axes, corresponding to both the in-plane and out-of-plane directions, which gives a full picture of the arrangement of diffracting material on the surface of the film in reciprocal space. The shape and intensity distribution of the diffracting peaks is an indication of the relative orientation of a specific plane to the surface. A polycrystalline film with no preferential orientation (completely random alignment) will result in rings of uniform

intensity, as would be expected from powder samples. An isotropic film with a preferred orientation but some degree of disorder will have a diffraction pattern with arcs of intensity, and the spread of that arc will depend on the degree of disorder. For a perfectly ordered film, the arcs will tighten into discrete spots.

Generally, it is thought that a high degree of alignment is preferred for charge transport, with the π-stacking planes oriented more edge-on to the substrate to allow for efficient charge hopping.[80,81] This, however, is highly dependent on the alignment and the preferred charge transport pathway of the molecule in the present crystal polymorph. As MPcs adopt multiple polymorphs, corroborating the GIWAXS data to single crystal data is important to understand the implications of the scattering patterns on the final charge transport efficiency in OTFTs. The discrete orientations of the π-stacking plane of MPcs and their relative populations in a thin film can be obtained by performing azimuthal linecuts across the entire range of χ angles, at the location of the diffraction peak corresponding to the π-stacking plane.[24] This has been used to characterize how fabrication parameters or molecular structure affects the molecular orientation of R_2-SiPcs[32,33,36,41] and other small molecules.[82–84] In addition to crystallite orientations, the degree of crystallinity (DoC) can be determined by analyzing the integrated diffraction intensity, and the crystallite size and disorder by analyzing peak width.[24] The review article by Rivnay *et al.* (2012) gives a comprehensive overview on the background and specifics of those calculations.[24]

Near edge X-ray absorption fine structure (NEXAFS) spectroscopy is a technique that uses the absorption of soft X-rays to characterize the bulk composition and bonding characteristics of thin films.[24] The absorption of X-rays excites K-shell electrons to a low-lying antibonding orbital of π^* or σ^*, and the intensity and location of these excitation resonances changes depending on the chemical structure of organic molecule.[23] When the X-ray beam is polarized or the sample is rotated relative to the beam, the dichroic behavior of molecules in a thin film can be investigated to determine their relative orientation by changes in peak intensity of relevant molecular planes (bonds). For example, to characterize the orientation of a MPc in a thin film, we can take the change in peak intensity of the 1s $\rightarrow \pi^*$ transition of the main MPc macrocycle as we rotate the

sample or polarize the beam, as demonstrated in previous work by Dindault *et al*.[85] Details and calculations involved in the use of NEXAFS in the characterization of thin film orientation will be discussed in **Chapter 4**. This technique characterizes not only the crystalline regions of a film, but all molecules in disordered or misaligned crystals that do not give a diffraction signal by GIWAXS, giving a more complete picture of the arrangement through the entire depth of the film.[23,24] When the X-ray beam is spatially resolved, it can be used in scanning transmission X-ray microscopy (STXM – **Figure 1.7c**), where a beam is scanned over the sample and spectral information is collected at each spot, generating an image based on the X-ray absorption at specific energies. This can allow for the determination of grain size and crystallite-specific orientation calculations.[85]

1.3.2 Additional Morphological Characterization of MPc Films

While X-rays offer many advantages in characterizing small molecule thin films, they are not as well-suited for determining grain packing and boundary sizes or surface texture. Some of these properties can be approximated using X-ray techniques, like using GIWAXS to determine crystallite size, but the calculations can be tedious and require assumptions that are not always true for polycrystalline small molecule films. Techniques like atomic force microscopy (AFM) can be very useful to visualize the nanoscale features on thin film surfaces and determine film roughness, which influence OTFT and sensor performance. In an AFM experiment, the thin film sample is scanned by a sharp tip mounted on the end of a cantilever, and the oscillation amplitude of the cantilever is monitored as the probe approaches the sample surface, providing an image of the surface topology. These images can be processed to determine the root mean squared (RMS) roughness of the imaged area, and the grain sizes and boundaries can be qualitatively compared or quantitatively measured using various data processing tools. AFM can give a height resolution <0.1 nm, depending on the instrument, while the lateral resolution is dependent on the tip radius and can achieve nm-scale resolution as well.[86] The technique can also scan over large areas, covering the entire channel length of a typical OTFT. As previously illustrated in **Figure 1.6**, AFM images are excellent for visualizing different crystallite sizes and structures of MPc film surfaces to show the effect of

fabrication parameters,[34,41] surface chemistry,[32,33] or molecular structure[36,68,87] to correlate observed film morphologies with OTFT performance.

Another useful lab scale technique in the characterization of MPc thin films is Raman microscopy, which involves the measurement of the vibrational modes of a material to ultimately determine its composition or crystallographic structure. The intensity of a Raman band depends on the orientation of a materials' axis of symmetry with respect to the direction of the excited laser. The choice of laser depends on the light absorption of the material and the potential for resonant Raman effects when the band gap of the material approaches the laser energy.[88] For most MPc applications, the optimal laser is 532 nm, as MPcs experience an absorption dip at this wavelength, reducing the fluorescence and resonance Raman effects.[89] Polarized Raman microscopy, particularly, can be used to generate orientational maps and determine the packing structure and polymorph formation of planar and nonplanar MPcs using the internal molecular vibration approach.[90–95] As the intensity of Raman signals are dependent on their orientation to the laser, when the laser is polarized the relative orientation to the surface can be determined by mapping the change in peak intensity with polarization.[88,91,93–95] This approach does not rely on diffraction or single crystal data, so it can be used to gather information on new materials, and on both amorphous and crystalline phases of thin films while being less energy intensive and faster than synchrotron methods like STXM. However, the spatial resolution is its weakness when generating maps or images, as the resolution is limited by optical diffraction, which for most visible spectral range lasers is from 200 nm – 1 μm.[88] This makes orientation map generation of PVD films less useful, as PVD results in relatively homogenous films on the macroscale with very little average orientation deviation. However, it can be useful to detect and map widespread film rearrangements due to device operation bias stress,[96] thermal annealing,[95] or analyte exposure. The latter example is the use case explored in **Chapter 4**, and the specifics of the procedure followed are detailed there, following protocols established in recent work by Cranston *et al.* (2024).[95] Enhanced Raman spectroscopy techniques, such as tip-enhanced Raman spectroscopy (TERS), which is a combination of scanning probe microscopy and surface-enhanced Raman spectroscopy

(SERS), can bring the resolution down to <10 nm.[97,98] However, this technique requires highly specialized equipment.

By using a combination of X-ray based techniques and other surface characterization methods, we can get a full picture of amorphous and crystalline phases of thin films from the molecular-scale to the device-scale grain arrangements. The choice of the most suitable technique to characterize OTFT thin films will depend on the information available for the material, and multiple techniques can be used in combination to confirm the morphology of new materials.

1.4 OTFT Sensors

OTFTs have been used for a variety of sensing applications, such as pressure and temperature sensors,[99,100] gas sensors,[101–105] and even highly sensitive biological sensors.[61,106–110] OTFTs allow for molecular and architectural engineering of the semiconductor, dielectric, and electrodes to achieve a sensitivity that is required for its application, making OTFTs an interesting avenue for the development of low-cost, point-of-use sensors. When an OTFT is exposed to an analyte, it experiences changes in its electrical performance. These changes can be caused for a variety of reasons, from doping of the material, to changes in the thin-film morphology, to the introduction of defects and charge traps, among others. By characterizing and exploiting these interactions, high-performing OTFT sensors can be developed for a variety of analytes and applications. Sensitization techniques, such as the utilization and/or immobilization of chemical or biological probes is common to help achieve high sensitivity for biological applications.[3,110–114] A recent review article by King & Lessard (2024) highlights the different sensing mechanisms and strategies used in the development and fabrication of OTFT sensors, for additional reading on this topic.[17]

1.4.1 OTFT Cannabinoid Sensors

In recent years, recreational and medicinal cannabis (*Cannabis sativa*) use has been growing in popularity, with countries increasingly removing restrictions on its consumption and sale.[115] The psychotropic effects commonly associated with cannabis are caused by cannabinoids produced in the plant, most notably Δ^9-tetrahydrocannabinolic acid (THCA) that, upon heating, decarboxylates to Δ^9-

tetrahydrocannabinol (THC), which is known to cause psychogenic effects in consumers.[116] THC is chemically very similar to other cannabinoids in cannabis products, including some that are potentially therapeutic, such as cannabidiol (CBD).[116] Due to this chemical similarity, illustrated in **Figure 1.8**, it is difficult to differentiate THC and CBD in consumer products or human biological samples, which presents a challenge for a variety of cannabis-related fields, including cannabis producers, government regulatory bodies, law enforcement, and medical professionals. The current state-of-the-art detection methods used in industry, such as high-performance liquid chromatography (HPLC), have a high level of sensitivity but are expensive, time-consuming, require specialists to interpret the results, and cannot be performed on-site.[117] Thus, there is a present need for low-cost point-of-source sensors that maintain both accuracy and a high level of sensitivity. OTFT-based sensors are a promising alternative that offer fast and accurate detection of cannabinoids while being accessible, disposable, and inexpensive.[106,111,118]

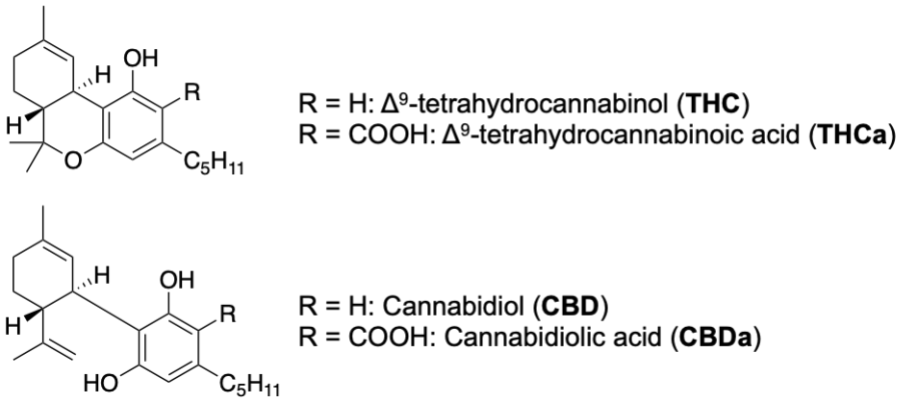

***Figure 1.8**. Chemical structure of THC/THCa and CBD/CBDa.*

Previously, our group has demonstrated copper phthalocyanine (CuPc) OTFT sensors for ratiometric detection and differentiation of cannabinoids.[111] Observed by spectroelectrochemistry and 2D nuclear magnetic resonance (NMR) spectroscopy, cannabinoids interact strongly with MPcs in solution, and in thin-films, causing changes in Pc–Pc π-stacking and increasing π-electron delocalization.[119] These interactions can induce recrystallization of MPc thin-films, altering thin-film morphologies and nanostructures, resulting in OTFT performance changes which enhance the detection of THC and lead to better sensitivity.[87] ZnPc has been identified as another material

sensitive to cannabinoids, and as a subject of previous work in our lab, we have found its film morphology to be highly tunable to improve the detection of cannabinoids. The presence of THC and CBD induces structural changes within ZnPc films, disrupting charge pathways and leading to an exaggerated sensing response.[72] A particularly interesting material however, is Cl-AlPc, due to its central nonplanarity. The unique packing structures of Cl-AlPc make it particularly susceptible to cannabinoid-induced physical effects, demonstrating greater interactions both in solution and as a thin-film compared to CuPc.[87,119] This thesis further characterizes the thin film interactions of Cl-AlPc, particularly in **Chapters 2** and **3**, while also exploring the possibility of integrating new MPc derivatives into this cannabinoid sensing platform in **Chapter 4**.

1.5 Scope of the Thesis

This thesis focuses on the fabrication of MPc-based OTFTs and thin films, which were then exposed to THC and CBD solution and vapor samples at industrially relevant concentrations. These films and devices were then characterized electrically and morphologically with the purpose of drawing connections between the electrical and thin film responses of different MPc structures.

In **Chapter 2**, I expanded on previous work in our group that identified Cl-AlPc as an interesting active material in cannabinoid OTFT sensors. I probed the influence that various film properties have on the THC and CBD response of this molecule, including film thickness and device architecture. I fabricated devices with three different film thicknesses and six different device architectures to compare their electrical responses. Using an ANOVA statistical analysis, I extracted which factors influenced the electrical response to cannabinoids The films of different thicknesses were also characterized by AFM and GIWAXS to visualize their surface rearrangement in response to THC and CBD solution and vapor samples. This work demonstrated the importance that film thickness had on the sensing response and highlighted that the quality of charge transport pathways is important for a larger sensing response.

Chapter 3 continues by investigating Cl-AlPc as the base active material in OTFT cannabinoid sensors, but I sought to investigate the effect of the axial group on this sensing response. For this study, I synthesized a group of five additional axially

phenoxylated R-AlPc molecules with different substituents, all of which were confirmed by NMR and mass spectrometry. I then integrated them into OTFTs by PVD and characterized their baseline electrical performance, and thin film morphologies. Following, they were exposed to THC and CBD solution and vapor samples and re-characterized to determine their response. Thin film characterization was performed by a combination of AFM, Raman, XRD and GIWAXS. This study found that making simple axial substitutions can increase the response to cannabinoids by introducing new crystal arrangements and polymorphs that shift upon exposure to cannabinoids.

The strategy of MPc chemical modification was continued in **Chapter 4**, when I investigated a fully fluorinated, air stable, *n*-type R_2-SiPc as the active material in an OTFT cannabinoid sensor. This molecule, $(F_5PhO)_2$-F_{16}-SiPc, was developed to expand the library of air stable *n*-type materials, but our lab had never previously incorporated an SiPc in our cannabinoid sensors due to their environmental instability. This presented an opportunity to incorporate this metal centre and investigate the effect of extensive peripheral and axial fluorination on the cannabinoid response. Electrical characterization was completed before and after cannabinoid exposure, showing no significant response to THC or CBD. To investigate the reason, the film was characterized by a combination of NEXAFS, Raman and GIWAXS, where no film reorganization was observed, which has been found to be the driving force behind the sensing response of MPc OTFTs. This study reaffirmed the importance of film recrystallization on the electrical response to cannabinoids in MPc OTFTs and informed us that the hydrogens in the MPc structure, along with the reactivity of the metal, likely have a large influence on the interactions at the film surface that lead to this recrystallization.

Chapter 5 highlights the additional work I have contributed to during my Ph.D. studies, particularly in the areas of OTFT fabrication and characterization, GIWAXS characterization, and sensor platform development. The abstracts for the publications are included with context to the work I contributed on each project. Finally, in **Chapter 6**, I highlight the overall conclusions of my thesis and present some future research I think could be interesting and worth pursuing in MPc-based sensing.

1.6 References

[1] G. H. Gelinck, H. E. A. Huitema, E. van Veenendaal, E. Cantatore, L. Schrijnemakers, J. B. P. H. van der Putten, T. C. T. Geuns, M. Beenhakkers, J. B. Giesbers, B.-H. Huisman, E. J. Meijer, E. M. Benito, F. J. Touwslager, A. W. Marsman, B. J. E. van Rens, D. M. de Leeuw, *Nature Mater* **2004**, *3*, 106.

[2] G. Gelinck, P. Heremans, K. Nomoto, T. D. Anthopoulos, *Adv. Mater.* **2010**, *22*, 3778.

[3] J. Liu, M. Agarwal, K. Varahramyan, *Sens. Actuators B: Chem* **2008**, *135*, 195.

[4] M. D. Dankoco, G. Y. Tesfay, E. Benevent, M. Bendahan, *Mater. Sci. Eng. B* **2016**, *205*, 1.

[5] D. Gupta, Y. Hong, *Org. Electron.* **2010**, *11*, 127.

[6] B. Kumar, B. K. Kaushik, Y. S. Negi, *Polymer Reviews* **2014**, *54*, 33.

[7] H. Klauk, *Chem. Soc. Rev.* **2010**, *39*, 2643.

[8] B. Kumar, B. K. Kaushik, Y. S. Negi, *Journal of Materials Science: Materials in Electronics* **2014**, *25*, 1.

[9] H. Bässler, A. Köhler, in *Unimolecular and Supramolecular Electronics I: Chemistry and Physics Meet at Metal-Molecule Interfaces* (Ed.: R. M. Metzger), Springer, Berlin, Heidelberg, **2012**, pp. 1–65.

[10] V. Coropceanu, J. Cornil, D. A. da Silva Filho, Y. Olivier, R. Silbey, J.-L. Brédas, *Chem. Rev.* **2007**, *107*, 926.

[11] O. A. Melville, B. H. Lessard, T. P. Bender, *ACS Appl Mater Interfaces* **2015**, *7*, 13105.

[12] C.-H. Kim, Y. Bonnassieux, G. Horowitz, *IEEE T-ED* **2014**, *61*, 278.

[13] S. Blawid, N. J. Dallaire, B. H. Lessard, *J-FLEX* **2022**, *1*, 114.

[14] G. Horowitz, M. E. Hajlaoui, R. Hajlaoui, *J. Appl. Phys.* **2000**, *87*, 4456.

[15] N. Tessler, Y. Preezant, N. Rappaport, Y. Roichman, *Adv. Mater.* **2009**, *21*, 2741.

[16] Y. Xie, C. Ding, Q. Jin, L. Zheng, Y. Xu, H. Xiao, M. Cheng, Y. Zhang, G. Yang, M. Li, L. Li, M. Liu, *SmartMat* **2024**, *5*, e1261.

[17] B. King, B. H. Lessard, *J. Mater. Chem. C* **2024**, *12*, 5654.

[18] P. Lin, F. Yan, P. Lin, F. Yan, *Adv. Mater.* **2012**, *24*, 34.

[19] J.-H. Kwon, M.-H. Kim, J.-H. Bae, *J. Mater. Chem. C* **2023**, *12*, 29.

[20] Z. Hao, Z. Wu, S. Liu, X. Tang, J. Chen, X. Liu, *J. Mater. Chem. C* **2024**, *12*, 9427.

[21] D. Liu, Q. Miao, *Mater. Chem. Front.* **2017**, *2*, 11.

[22] H. Klauk, G. Schmid, W. Radlik, W. Weber, L. Zhou, C. D. Sheraw, J. A. Nichols, T. N. Jackson, *Solid-State Electron.* **2003**, *47*, 297.

[23] A. Salleo, R. J. Kline, D. M. DeLongchamp, M. L. Chabinyc, *Adv. Mater.* **2010**, *22*, 3812.

[24] J. Rivnay, S. C. B. Mannsfeld, C. E. Miller, A. Salleo, M. F. Toney, *Chem. Rev.* **2012**, *112*, 5488.

[25] N. Kobayashi, *Curr. Opin. Solid State Mater. Sci.* **1999**, *4*, 345.

[26] A. B. P. Lever, in *Advances in Inorganic Chemistry and Radiochemistry* (Eds.: H. J. Emeléus, A. G. Sharpe), Academic Press, **1965**, pp. 27–114.

[27] C. G. Claessens, U. Hahn, T. Torres, *Chem. Rec.* **2008**, *8*, 75.

[28] D. Elkington, N. Cooling, W. Belcher, P. C. Dastoor, X. Zhou, *Electronics* **2014**, *3*, 234.

[29] M. Urbani, M. E. Ragoussi, M. K. Nazeeruddin, T. Torres, *Coord. Chem. Rev.* **2019**, *381*, 1.

[30] G. de la Torre, G. Bottari, T. Torres, *Adv. Energy Mater.* **2017**, *7*, 1601700.

[31] M. C. Vebber, B. King, C. French, M. Tousignant, B. Ronnasi, C. Dindault, G. Wantz, L. Hirsch, J. Brusso, B. H. Lessard, *Can J Chem Eng.* **2023**, *101*, 3019.

[32] R. R. Cranston, M. C. Vebber, J. Faleiro Berbigier, J. Brusso, T. L. Kelly, B. H. Lessard, *Adv. Electron. Mater.* **2022**, *8*, 2200696.

[33] B. King, C. L. Radford, M. C. Vebber, B. Ronnasi, B. H. Lessard, *ACS Appl. Mater. Interfaces* **2023**, *15*, 14937.

[34] R. R. Cranston, B. King, C. Dindault, T. M. Grant, N. A. Rice, C. Tonnelé, L. Muccioli, F. Castet, S. Swaraj, B. H. Lessard, *J. Mater. Chem. C* **2022**, *10*, 485.

[35] B. H. Lessard, T. M. Grant, R. White, E. Thibau, Z.-H. Lu, T. P. Bender, *J. Mater. Chem. A* **2015**, *3*, 24512.

[36] B. King, O. A. Melville, N. A. Rice, S. Kashani, C. Tonnelé, H. Raboui, S. Swaraj, T. M. Grant, T. McAfee, T. P. Bender, H. Ade, F. Castet, L. Muccioli, B. H. Lessard, *ACS Appl. Electron. Mater.* **2021**, *3*, 325.

[37] H. Raboui, M. AL-Amar, A. I. Abdelrahman, T. P. Bender, *RSC Adv.* **2015**, *5*, 45731.

[38] M.-T. Dang, T. M. Grant, H. Yan, D. S. Seferos, B. H. Lessard, T. P. Bender, *J. Mater. Chem. A* **2017**, *5*, 12168.

[39] A. J. Pearson, T. Plint, S. T. E. Jones, B. H. Lessard, D. Credgington, T. P. Bender, N. C. Greenham, *J. Mater. Chem. C* **2017**, *5*, 12688.

[40] M. C. Vebber, N. A. Rice, J. L. Brusso, B. H. Lessard, *ACS Appl. Energy Mater.* **2022**, *5*, 3426.

[41] R. R. Cranston, M. C. Vebber, J. F. Berbigier, N. A. Rice, C. Tonnelé, Z. J. Comeau, N. T. Boileau, J. L. Brusso, A. J. Shuhendler, F. Castet, L. Muccioli, T. L. Kelly, B. H. Lessard, *ACS Appl Mater Interfaces* **2021**, *13*, 1008.

[42] R. R. Cranston, M. C. Vebber, N. A. Rice, C. Tonnelé, F. Castet, L. Muccioli, J. L. Brusso, B. H. Lessard, *ACS Appl. Electron. Mater.* **2021**, *3*, 1873.

[43] N. J. Yutronkie, B. King, O. A. Melville, B. H. Lessard, J. L. Brusso, *J. Mater. Chem. C* **2021**, *9*, 10119.

[44] A. Hoshino, Y. Takenaka, H. Miyaji, *Acta Cryst B* **2003**, *59*, 393.

[45] Y. Yoon, J. Y. Koo, J. Oh, S. Kim, H. C. Choi, S. M. Yoon, *Inorg. Chem. Front.* **2020**, *7*, 2178.

[46] H. Raboui, A. J. Lough, T. Plint, T. P. Bender, *Cryst. Growth Des.* **2018**, *18*, 3193.

[47] M. Dailey, C. Besson, *CrystEngComm* **2021**, *23*, 7151.

[48] X. Ai, J. Lin, Y. Chang, L. Zhou, X. Zhang, G. Qin, *Appl. Surf. Sci.* **2018**, *428*, 788.

[49] P. Erk, H. Hengelsberg, M. F. Haddow, R. van Gelder, *CrystEngComm* **2004**, *6*, 475.

[50] B. H. Lessard, M. AL-Amar, T. M. Grant, R. White, Z.-H. Lu, T. P. Bender, *J. Mater. Chem. A* **2015**, *3*, 5047.

[51] F. Iwatsu, *J. Phys. Chem.* **1988**, *92*, 1678.

[52] K. Xiao, R. Li, J. Tao, E. A. Payzant, I. N. Ivanov, A. A. Puretzky, W. Hu, D. B. Geohegan, *Adv. Funct. Mater.* **2009**, *19*, 3776.

[53] M. Waldrip, O. D. Jurchescu, D. J. Gundlach, E. G. Bittle, *Adv. Funct. Mater.* **2020**, *30*, 1904576.

[54] P. Li, Z.-H. Lu, *Small Sci.* **2021**, *1*, 2000015.

[55] O. A. Melville, T. M. Grant, K. Lochhead, B. King, R. Ambrose, N. A. Rice, N. T. Boileau, A. J. Peltekoff, M. Tousignant, I. G. Hill, B. H. Lessard, *ACS Appl. Electron. Mater.* **2020**, *2*, 1313.

[56] C.C. Leznoff, A.B.P. Lever, *Phthalocyanines: Properties and Applications*, Wiley-VCH, **1998**.

[57] T. Fukuda, N. Kobayashi, in *Handbook of Porphyrin Science*, World Scientific, **2010**.

[58] Q. Chen, D. Gu, J. Shu, X. Tang, F. Gan, *Mater. Sci. Eng. B* **1994**, *25*, 171.

[59] A. A. M. Farag, *Opt. Laser Technol.* **2007**, *39*, 728.

[60] P. Day, R. J. P. Williams, *J. Chem. Phys.* **1962**, *37*, 567.

[61] N. T. Boileau, O. A. Melville, B. Mirka, R. Cranston, B. H. Lessard, *RSC Adv.* **2019**, *9*, 2133.

[62] J.-F. Li, S.-H. Su, K.-S. Hwang, M. Yokoyama, *J. Phys. D: Appl. Phys.* **2007**, *40*, 2435.

[63] B. King, M. C. Vebber, R. Ewenike, M. Dupuy, C. French, J. L. Brusso, B. H. Lessard, *Chem. Mater.* **2023**, *35*, 8517.

[64] B. H. Lessard, *ACS Appl Mater Interfaces* **2021**, *13*, 31321.

[65] D. Song, F. Zhu, B. Yu, L. Huang, Y. Geng, D. Yan, *Appl. Phys. Lett.* **2008**, *92*, 143303.

[66] D. Song, H. Wang, F. Zhu, J. Yang, H. Tian, Y. Geng, D. Yan, *Adv. Mater.* **2008**, *20*, 2142.

[67] Z. Bao, A. J. Lovinger, J. Brown, *J. Am. Chem. Soc.* **1998**, *120*, 207.

[68] R. R. Cranston, B. H. Lessard, *RSC Adv.* **2021**, *11*, 21716.

[69] G. Antczak, W. Kamiński, A. Sabik, C. Zaum, K. Morgenstern, *J. Am. Chem. Soc.* **2015**, *137*, 14920.

[70] Z. Zhang, M. G. Lagally, *Science* **1997**, *276*, 377.

[71] T. Vetter, M. Iggland, D. R. Ochsenbein, F. S. Hänseler, M. Mazzotti, *Cryst. Growth Des.* **2013**, *13*, 4890.

[72] Z. J. Comeau, R. R. Cranston, H. R. Lamontagne, C. S. Harris, A. J. Shuhendler, B. H. Lessard, *Commun Chem* **2022**, *5*, 1.

[73] C. Nicosia, J. Huskens, *Mater. Horiz.* **2013**, *1*, 32.

[74] Y. Ito, A. A. Virkar, S. Mannsfeld, J. H. Oh, M. Toney, J. Locklin, Z. Bao, *J. Am. Chem. Soc.* **2009**, *131*, 9396.

[75] S. Zhou, Q. Tang, H. Tian, X. Zhao, Y. Tong, S. Barlow, S. R. Marder, Y. Liu, *ACS Appl. Mater. Interfaces* **2018**, *10*, 15943.

[76] O. A. Melville, N. A. Rice, I. Therrien, B. H. Lessard, *Dyes Pigm.* **2018**, *149*, 449.

[77] A. Pandey, S. Dalal, S. Dutta, A. Dixit, *J Mater Sci: Mater Electron* **2021**, *32*, 1341.

[78] B.D. Cullity, S.R. Stock, *Elements of X-Ray Diffraction*, Pearson Education Limited, **2014**.

[79] C. Fan, Z. Zhao, *Synchrotron Radiation in Materials Science: Light Sources, Techniques, and Applications*, John Wiley & Sons, **2018**.

[80] L. Li, W. Hu, H. Fuchs, L. Chi, *Advanced Energy Materials* **2011**, *1*, 188.

[81] W. A. Memon, R. Zhou, Y. Zhang, Y. Wang, L. Liu, C. Yang, J. Zhang, A. Liaqat, L. Xie, Z. Wei, *Advanced Functional Materials* **2022**, *32*, 2110080.

[82] R. Li, H. U. Khan, M. M. Payne, D.-M. Smilgies, J. E. Anthony, A. Amassian, *Adv. Funct. Mater.* **2013**, *23*, 291.

[83] K. W. Chou, H. U. Khan, M. R. Niazi, B. Yan, R. Li, M. M. Payne, J. E. Anthony, D.-M. Smilgies, A. Amassian, *J. Mater. Chem. C* **2014**, *2*, 5681.

[84] M. Hodas, P. Siffalovic, P. Nádaždy, N. Mrkyvková, M. Bodík, Y. Halahovets, G. Duva, B. Reisz, O. Konovalov, W. Ohm, M. Jergel, E. Majková, A. Gerlach, A. Hinderhofer, F. Schreiber, *ACS Appl. Nano Mater.* **2018**, *1*, 2819.

[85] C. Dindault, B. King, P. Williams, J. H. Absi, M. D. M. Faure, S. Swaraj, B. H. Lessard, *Chem. Mater.* **2022**, *34*, 4496.

[86] Y. Gan, *Surf. Sci. Rep.* **2009**, *64*, 99.

[87] Z. J. Comeau, N. A. Rice, C. S. Harris, A. J. Shuhendler, B. H. Lessard, *Adv. Funct. Mater.* **2022**, *32*, 2107138.

[88] J. Álvarez-García, V. Izquierdo-Roca, P. Pistor, T. Schmid, A. Pérez-Rodríguez, in *Advanced Characterization Techniques for Thin Film Solar Cells*, John Wiley & Sons, Ltd, **2016**, pp. 469–499.

[89] C. Murray, N. Dozova, J. G. McCaffrey, S. FitzGerald, N. Shafizadeh, C. Crépin, *Phys. Chem. Chem. Phys.* **2010**, *12*, 10406.

[90] M. Szybowicz, J. Makowiecki, *J Mater Sci* **2012**, *47*, 1522.

[91] M. Szybowicz, W. Bała, K. Fabisiak, K. Paprocki, M. Drozdowski, *J Mater Sci* **2011**, *46*, 6589.

[92] M. Szybowicz, W. Bała, K. Fabisiak, K. Paprocki, M. Drozdowski, *Cryst. Res. Technol.* **2010**, *45*, 1265.

[93] M. Szybowicz, W. Bała, S. Dümecke, K. Fabisiak, K. Paprocki, M. Drozdowski, *Thin Solid Films* **2011**, *520*, 623.

[94] M. Szybowicz, T. Runka, M. Drozdowski, W. Bała, A. Grodzicki, P. Piszczek, A. Bratkowski, *J. Mol. Struct.* **2004**, *704*, 107.

[95] R. R. Cranston, T. D. Lanosky, R. Ewenike, S. Mckillop, B. King, B. H. Lessard, *Small Sci.* **2024**, *n/a*, 2300350.

[96] H. L. Cheng, W. Y. Chou, C. W. Kuo, Y. W. Wang, Y. S. Mai, F. C. Tang, S. W. Chu, *Adv. Funct. Mater.* **2008**, *18*, 285.

[97] P. Verma, *Chem. Rev.* **2017**, *117*, 6447.

[98] Z. Zhang, S. Sheng, R. Wang, M. Sun, *Anal. Chem.* **2016**, *88*, 9328.

[99] Y. Zang, F. Zhang, D. Huang, X. Gao, C. Di, D. Zhu, *Nat Commun* **2015**, *6*, 6269.

[100] N. T. Boileau, R. Cranston, B. Mirka, O. A. Melville, B. H. Lessard, *RSC Adv.* **2019**, *9*, 21478.

[101] Y. Jiang, W. Huang, X. Zhuang, Y. Tang, J. Yu, *Mater. Sci. Eng. B* **2017**, *226*, 107.

[102] F. Liao, C. Chen, V. Subramanian, *Sens. Actuators B: Chem* **2005**, *107*, 849.

[103] B. Nketia-Yawson, Y. Y. Noh, *Macromol. Res.* **2017**, *25*, 489.

[104] L. Torsi, A. Dodabalapur, L. Sabbatini, P. G. Zambonin, *Sens. Actuators B: Chem* **2000**, *67*, 312.

[105] M. Wu, S. Hou, X. Yu, J. Yu, *J. Mater. Chem. C* **2020**, *8*, 13482.

[106] C. Sun, R. Li, Y. Song, X. Jiang, C. Zhang, S. Cheng, W. Hu, *Anal. Chem.* **2021**, *93*, 6188.

[107] C. Chircov, A. M. Grumezescu, E. Andronescu, *Molecules* **2020**, *25*, 6013.

[108] J. Choi, T. W. Seong, M. Jeun, K. H. Lee, *Adv. Healthc. Mater.* **2017**, *6*, DOI 10.1002/adhm.201700796.

[109] J. Choi, M. Jeun, S. S. Yuk, S. Park, J. Choi, D. Lee, H. Shin, H. Kim, I. J. Cho, S. K. Kim, S. Lee, C. S. Song, K. H. Lee, *ACS Nano* **2019**, *13*, 812.

[110] Y.-H. Lin, Y. Han, A. Sharma, W. S. AlGhamdi, C.-H. Liu, T.-H. Chang, X.-W. Xiao, W.-Z. Lin, P.-Y. Lu, A. Seitkhan, A. D. Mottram, P. Pattanasattayavong, H. Faber, M. Heeney, T. D. Anthopoulos, *Adv. Mater.* **2022**, *34*, 2104608.

[111] Z. J. Comeau, N. T. Boileau, T. Lee, O. A. Melville, N. A. Rice, Y. Troung, C. S. Harris, B. H. Lessard, A. J. Shuhendler, *ACS Sens.* **2019**, *4*, 2706.

[112] E. Macchia, K. Manoli, B. Holzer, C. Di Franco, M. Ghittorelli, F. Torricelli, D. Alberga, G. F. Mangiatordi, G. Palazzo, G. Scamarcio, L. Torsi, *Nat Commun* **2018**, *9*, DOI 10.1038/s41467-018-05235-z.

[113] E. MacChia, A. Tiwari, K. Manoli, B. Holzer, N. Ditaranto, R. A. Picca, N. Cioffi, C. Di Franco, G. Scamarcio, G. Palazzo, L. Torsi, *Chem. Mater.* **2019**, *31*, 6476.

[114] E. Macchia, K. Manoli, B. Holzer, C. Di Franco, R. A. Picca, N. Cioffi, G. Scamarcio, G. Palazzo, L. Torsi, *Anal. Bioanal. Chem.* **2019**, *411*, 4899.

[115] A. DI, *Eur. J. Intern. Med.* **2018**, *49*, 7.

[116] R. Mechoulam, M. Peters, E. Murillo-Rodriguez, L. O. Hanuš, *Chem. Biodiversity* **2007**, *4*, 1678.

[117] B. De Backer, B. Debrus, P. Lebrun, L. Theunis, N. Dubois, L. Decock, A. Verstraete, P. Hubert, C. Charlier, *J. Chromatogr. B* **2009**, *877*, 4115.

[118] C. Sun, Y. X. Wang, M. Sun, Y. Zou, C. Zhang, S. Cheng, W. Hu, *Biosens. Bioelectron.* **2020**, *164*, 112251.

[119] Z. J. Comeau, G. A. Facey, C. S. Harris, A. J. Shuhendler, B. H. Lessard, *ACS Appl. Mater. Interfaces* **2020**, *12*, 50692.

Chapter 2: Chloro Aluminum Phthalocyanine-Based Organic Thin-Film Transistors as Cannabinoid Sensors: Engineering the Thin Film Response

---

This work is adapted from: ***Halynne R. Lamontagne****, Zachary J. Comeau, Rosemary R. Cranston, Nicholas T. Boileau, Cory S. Harris, Adam J. Shuhendler & Benoît H. Lessard, Sensors & Diagnostics, 2022, 1, 1165-1175.*
DOI: 10.1039/D2SD00071G

2.1 Context

During my undergraduate research and the early stages of my graduate studies, I was trained by a previous Ph.D. student, Dr. Zachary Comeau, on our groups' protocols for device fabrication and characterization. His work focused on the detection and speciation of cannabinoids by MPc-based OTFTs, and his most recent study at the time had demonstrated some interesting and unique solution-based interactions between Cl-AlPc and THC/CBD, as discussed in **Chapter 1**. This described work was meant to expand the characterization of those interactions from solution to Cl-AlPc thin films. We also sought to study the influence of film thickness and channel architecture on the strength of these interactions and their influence on the resulting OTFT response. Through a combination of electrical and thin-film characterization I found that an increase in exposed surface area led to an improvement in the OTFT response to cannabinoids. Both an increase in channel area and surface roughness demonstrated this improved response, both of which are generally associated with decreased device performance. This demonstrated that there is a balance to strike between fabricating a high-performing transistor, and a responsive sensor, and the conditions that are optimal for the former are not always optimal for the latter. Additionally, a decrease in film thickness led to an improved response, likely due to the smaller distance for charges to travel to the semiconductor-dielectric interface. Concurrently, this work helped validate the new pre-fabricated BGBC device architecture used in our custom autotester for sensor work.

2.2 Contributions of Authors

I performed the device fabrication and OTFT characterization. ZJC assisted with device characterization and OTFT data interpretation, and cannabinoid exposure studies. RRC performed the AFM and GIWAXS measurements and assisted me in the GIWAXS data workup and interpretation. NTB designed the new channel architecture used in this study, particularly the prefabricated autotester substrates. I authored the manuscript, and all co-authors provided editorial contributions.

2.3 Abstract

Cannabis producers, retailers, and law enforcement increasingly need low-cost point-of-source cannabinoid sensors. Organic thin-film transistor (OTFT) based sensors are a promising technology that can provide rapid speciation and detection of Δ^9-tetrahydrocannabinol (THC) while maintaining low manufacturing costs and ease of use. Herein, chloro aluminum phthalocyanine (Cl-AlPc) OTFTs were optimized through engineering film thickness (30, 50 or 100 nm) and the device source-drain geometry (W/L = 100, 200, 400, 800 and 1000), as these parameters have been shown to strongly influence OTFT performance. Optimized Cl-AlPc OTFT based sensors were exposed to both THC solution and THC vapor, demonstrating that improved device performance was not directly correlated with increased sensitivity. Grazing-incidence wide-angle X-ray scattering (GIWAXS) and atomic force microscopy (AFM) were used to interrogate thin-film morphology. While little change in molecular orientation resulted from film thickness or exposure to THC, the data suggests that the improved sensing response of Cl-AlPc-derived devices is directly related to increased thin-film surface area resulting from increased roughness and reduced film thickness.

2.4 Introduction

In recent years, recreational and medicinal cannabis (*Cannabis sativa*) use has been growing in popularity, with countries increasingly removing restrictions on its consumption and sale.[1] The psychotropic effects commonly associated with cannabis are caused by cannabinoids produced in the plant, most notably Δ^9-tetrahydrocannabinolic acid (THCA) that, upon heating, decarboxylates to Δ^9-tetrahydrocannabinol (THC), which is known to cause psychogenic effects in

consumers.[2] THC is chemically very similar to other cannabinoids in cannabis products, including some that are potentially therapeutic, such as cannabidiol (CBD).[2] Due to this chemical similarity, it is difficult to differentiate THC and CBD in consumer products or human biological samples, which presents a challenge for a variety of cannabis-related fields, including cannabis producers, government regulatory bodies, law enforcement, and medical professionals. The current state-of-the-art detection methods used in industry, such as high-performance liquid chromatography (HPLC), have a high level of sensitivity but are expensive, time-consuming, require specialists to interpret the results, and cannot be performed on-the-spot.[3] Thus, there is a present need for low-cost point-of-source sensors that maintain both accuracy and a high level of sensitivity. Organic thin-film transistor (OTFT)-based sensors are a promising alternative that offer fast and accurate detection of cannabinoids while being accessible, disposable, and inexpensive.[4–6] OTFTs have the potential to achieve a lower manufacturing cost than conventional electronics, as OTFTs utilize more affordable organic materials and are manufactured at ambient temperatures. The simple device structure of an OTFT also makes them conducive to high-volume manufacturing processes, like roll-to-roll printing.[7–14] OTFTs are three-electrode solid state electrical devices where current travels at the interface between an organic semiconductor and a dielectric. Changes in electrical behaviour can result from several mechanisms, including oxidation/reduction, and doping or physical changes in the active semiconducting material.[15–20] Understanding which mechanisms contribute to sensing and how these mechanisms interact will enable the optimization and enhancement of OTFT based sensors.

Metal and metalloid phthalocyanines (MPcs) are a class of conjugated macrocyclic molecules that have found success as semiconducting layers in OTFTs[21,22] and organic photovoltaics (OPVs).[23,24] MPcs are thermally and chemically stable, inexpensive to manufacture on the ton scale with facile metal substitution providing opportunities to tune molecular interactions for integration into OTFT sensors.[6,21,25–30] While many MPcs are insoluble or sparingly soluble in organic solvents, they can be modified with solubilizing groups making them potentially compatible with low-cost solution processing techniques. Previously, we demonstrated copper phthalocyanine (CuPc) OTFT sensors for ratiometric detection and differentiation of cannabinoids.[6] Observed by

spectroelectrochemistry and 2D NMR, cannabinoids interact strongly with MPcs in solution, and in thin-films, causing changes in Pc–Pc π-stacking and increasing π-electron delocalization.[31] These interactions can induce recrystallization of MPc thin-films, altering thin-film morphologies and nanostructures, resulting in OTFT performance changes which enhance the detection of THC and lead to better sensitivity.[26] The central aluminum chloride of chloro aluminum phthalocyanine (Cl-AlPc, **Figure 2.1**) bends the MPc ring, resulting in unique packing structures that are susceptible to cannabinoid induced physical effects, demonstrating greater interactions both in solution and as a thin-film compared to CuPc.[26,31] In bottom-gate bottom-contact (BGBC) OTFTs, the thickness of the deposited semiconductor film has been observed to effect OTFT charge transport properties.[32–34] For evaporated small molecules, surface coverage, growth mode, and thin-film morphology can change with thickness, leading to altered charge transport properties.[25,35–38] Thus, to increase the sensitivity of cannabinoid sensors, we exploit the sensitivity of Cl-AlPc to cannabinoids by altering the semiconducting layer and device architecture of Cl-AlPc-based OTFTs.

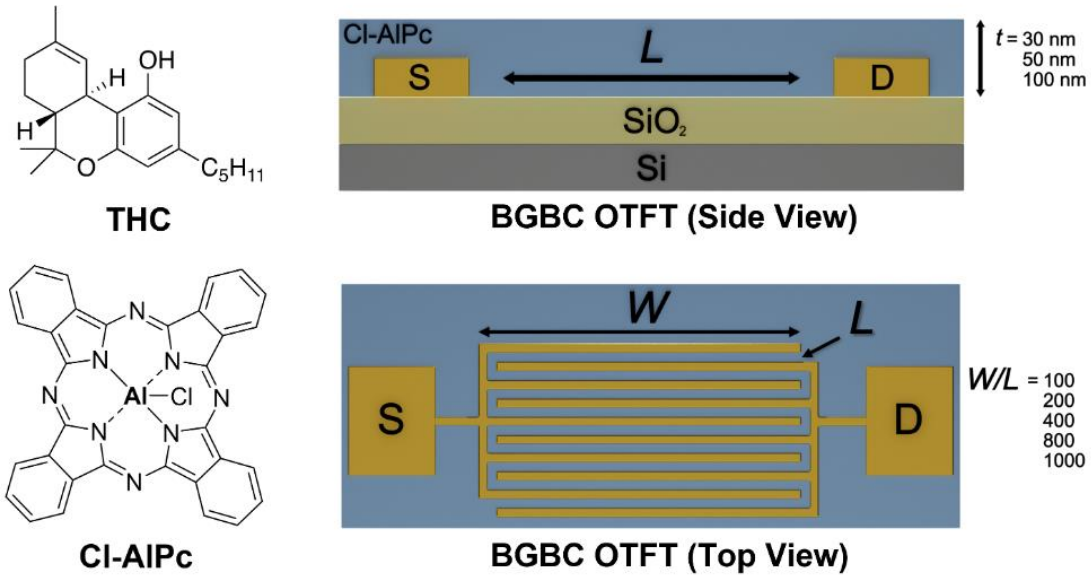

Figure 2.1. *Chemical structure of chloro aluminum phthalocyanine (Cl-AlPc) and Δ^9-tetrahydrocannabinol (THC), as well as a schematic representation of the bottom-gate bottom-contact (BGBC) organic thin-film transistor (OTFT) architecture used in this study.*

Towards the goal of understanding how to optimize Cl-AlPc-based devices for THC sensing, we studied the molecular interactions of Cl-AlPc in OTFTs and the structural

alterations that take place upon exposure to cannabinoids in both liquid and vapor phases. By synchrotron grazing-incident wide-angle X-ray scattering (GIWAXS) and atomic force microscopy (AFM) we probe the nanostructures of Cl-AlPc thin-films, comparing the effects of OTFT architecture and thin-film thickness to overall OTFT sensor performance. In addition, we aim to determine if these parameters affect baseline device performance in the same way as sensor performance to differentiate the dynamics of THC sensing from normal OTFT operation. This work demonstrates that device architecture has little effect on sensor performance; instead, we find that film thickness substantially impacts both pre- and post-exposure device performance and sensitivity, particularly to liquid THC. This illustrates the importance of deposition conditions and thin-film morphology.

2.5 Results and Discussion

2.5.1 Baseline Cl-AlPc OTFT Optimization

To examine the effects of device architecture on OTFT performance we prepared a series of BGBC Cl-AlPc-based OTFTs under identical evaporation conditions, with thin-film thicknesses of 30 nm, 50 nm or 100 nm and *W*/*L* ratios from 100 to 1000 on OTS treated Si/SiO_2 substrates (**Figure 2.1**). Characteristic transfer curves can be found in **Figure 2.2**, along with plots of the on-current (I_{on}) and μ_h with the tested *W*/*L* ratios and film thicknesses. The output curves and a summary table can be found in Fig. S1 and Table S1, respectively. A two-way ANOVA analysis was performed on the data shown in **Figure 2.2D** and **E** to determine the significance of each pair-wise data set to a confidence of 95%, and the results can be found in **Table 2.2** (**Supporting Information**). As expected from **Equation 2.1**, I_{on} increases with increasing *W*/*L*, from approximately 100 µA to 5000 µA from a *W*/*L* of 100 to 1000. Additionally, I_{on} increases with increasing film thickness, yielding an increase in μ_h from 0.02 $cm^2\ V^{-1}\ s^{-1}$ to 0.5 $cm^2\ V^{-1}\ s^{-1}$, consistent with previously reported performances for Cl-AlPc devices.[26,27]

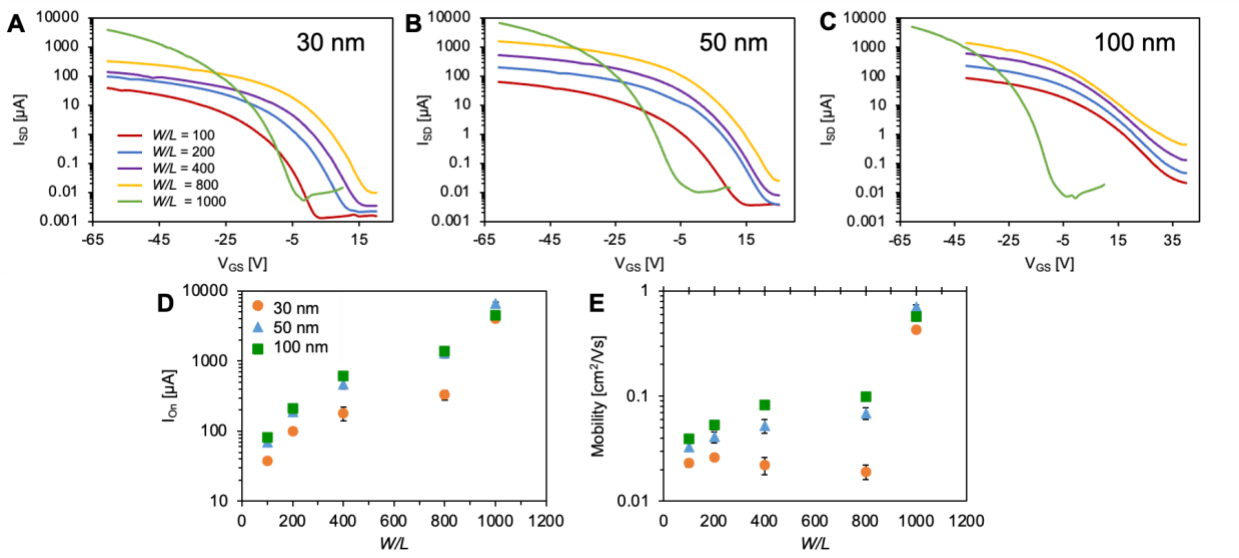

Figure 2.2. *Transfer curves for CI-AlPc devices with 30 nm (A), 50 nm (B), and 100 nm (C) thickness. I_{on} (D) and μ_h (E) are plotted with W/L and CI-AlPc thickness. V_{SD} was -50 V. In panels D and E, points represent the means of a minimum of 4 devices and error bars represent standard deviation. Significance of data has been analyzed by two-way ANOVA and can be found in Table 2.2.*

An ideal transfer curve would have a V_T near 0, a low I_{off} followed by a sharp increase in current after the V_T (steep subthreshold slope), and the current would plateau at a high I_{on} resulting in a high $I_{on/off}$, with low hysteresis throughout the transfer curve. While a higher I_{on} led to a higher μ_h for the thicker films, the transfer curves for these films are less ideal. A greater V_T, lower $I_{on/off}$, and a smaller subthreshold slope is observed for the 100 nm devices compared to the 30 nm devices. The I_{on} also increases as the *W*/*L* ratio increases from 100 to 800, while the transfer curves become less ideal. A *W*/*L* of 1000 shows the most ideal transfer curves with the highest I_{on} and μ_h. The devices with a *W*/*L* ratio of 1000 had the same *L* (10 μm) but a greater *W* (10 mm) than the devices with a *W*/*L* ratio of 200 (*W* = 2 mm), thus, the dependence of these metrics on *W*/*L* is likely a result of contact resistance, which becomes more dominant as *L* decreases.[39,40] This increased contact resistance would lead to the less optimal transfer characteristics that we observed for higher *W*/*L* ratios. Additionally, there is a reduced effect from channel resistance in devices with a lower *L*,[39,40] leading to higher operating currents. This resistance dominates in devices that have a greater *L*, which explains the lower performance of the devices with a lower *W*/*L* ratio. The design of the devices with the *W*/*L* of 1000 balances the channel and contact resistances to give high operating current with ideal transfer characteristics. This balance is illustrated by the V_T of

the devices in **Figure 2.2**, where the V_T increases from a W/L of 100 to 800 but drops for the W/L of 1000.

The contact resistance for each Cl-AlPc thickness was calculated as a function of channel length using the modified-transfer length method (M-TLM) (**Equation 2.2**), the results of which can be found in **Table 2.3** (**Supporting Information**). The contact resistance decreased with increasing film thickness. This supports the resulting higher I_{on} and μ_h observed for the 100 nm devices, as its contact resistance was the lowest, allowing for easier charge injection and higher mobilities.

Thin-films of Cl-AlPc, with thicknesses of 30 nm, 50 nm, or 100 nm, were characterized by GIWAXS with the resulting spectra shown in **Figure 2.3**. These spectra reveal that the films are moderately semicrystalline and correspond well to the single crystal as demonstrated by the diffraction patterns shown in **Figure 2.3G**. The high intensity (001) peak at approximately q = 0.5 Å^{-1}, along the q_z axis observed in all spectra indicates a major preferential orientation of molecules aligned parallel to the substrate. The distinct feature at χ = −30° observed in **Figure 2.3H** indicates Cl-AlPc molecules aligned ∼30° to the substrate in a face-on configuration for all thin-film thicknesses. Although no change in molecular orientation is observed with film thickness, a loss of molecular order is exhibited in the thicker 100 nm films. Characterizing the surface morphology of the Cl-AlPc films by AFM, we observe the ordering of the grains improves with decreasing film thickness, supporting the observations from the GIWAXS spectra. The 30 nm film shows the most ordered grains and sharpest signals by GIWAXS, indicating the highest level of molecular order.

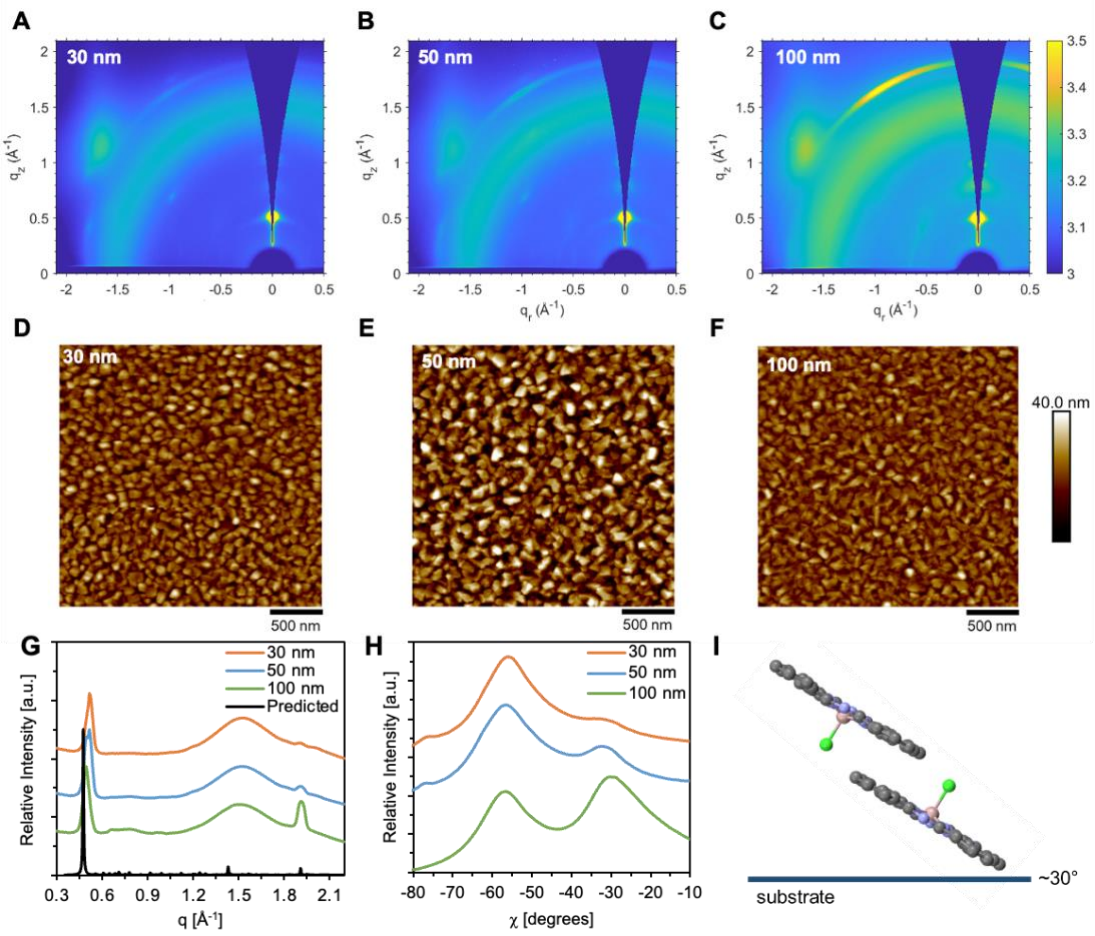

***Figure 2.3**. 2D scattering patterns (θ = 0.3°) of (A) 30 nm, (B) 50 nm, and (C) 100 nm thick Cl-AlPc. Atomic force microscopy (AFM) images of (D) 30 nm, (E) 50 nm, and (F) 100 nm thick Cl-AlPc with scale bars of 500 nm. Diffraction pattern of Cl-AlPc (G) predicted from single crystal (CCDC #1134071)[41] and 100 nm, 50 nm and 30 nm thick films determined by grazing-incidence wide-angle X-ray scattering (GIWAXS). Linecut profiles (H) of 100 nm, 50 nm, and 30 nm thick Cl-AlPc films with respect to χ using a q range between 1.9–2.1 Å^{-1}. Molecular orientation (I) of Cl-AlPc relative to the substrate.*

The 30 nm films also demonstrated the best transfer characteristics in their corresponding devices, with high $I_{on/off}$ ratios, low V_T, and greater subthreshold slopes (**Figure 2.2**). In contrast, the 100 nm film showed more disordered grains by AFM and broad GIWAXS signals, indicating a disordered morphology (**Figure 2.3**). Though these films had high operating currents and low contact resistance, which yielded a high μ_h, they had the worst transfer characteristics with a high V_T, hysteresis, and low subthreshold slope (**Figure 2.2**). The 50 nm films appear significantly rougher than the other thicknesses, suggesting surface-ordered film growth up to ~30 nm (RMS = 5.69 nm) which transitions to island growth up to ~50 nm (RMS = 9.49 nm), yielding the

observed roughness and grain order (**Figure 2.3**). The islands fill in as the thickness approaches 100 nm (RMS = 5.06 nm), yielding the smoothest, but most disordered, films. Consequentially, the more ordered films will have improved charge transport pathways, however, the number of pathways available are likely lower. This will hinder charge injection and limit the operating current and μ_h as a result. Alternatively, the 100 nm films experience an increased number of charge transport pathways, making charge injection easier, giving rise to the higher μ_h and operating current in their corresponding devices. The disordered nature of the films and these pathways causes worse transfer characteristics. The 50 nm films strike a balance somewhere in between, experiencing both an increased number of charge transport pathways compared to the 30 nm film, and improved charge transport pathways compared to the 100 nm film. This leads to a high μ_h and operating current, while maintaining favorable transfer characteristics. Though thin-film morphology is conserved for all thicknesses, the degree of molecular order, and thus the OTFT characteristics, varies, with a >5-fold increase in mobility at the expense of other semiconducting properties. Thus, it is important to control the thickness of the Cl-AlPc film to control the grain morphology, charge transport properties, and baseline performance of Cl-AlPc OTFTs.

2.5.2 Cl-AlPc OTFT Sensor Optimization

In our previous studies,[26,31] we identified that Cl-AlPc strongly interacts with THC, leading to large changes in OTFT performance. Thus, by exposing BGBC OTFTs with different Cl-AlPc film thicknesses (30 nm, 50 nm, and 100 nm) and two geometries (W/L = 200 and 1000) to both a liquid solution of THC and THC vapor, we could examine thin-film processing conditions and device architecture of Cl-AlPc OTFTs with the goal of establishing the greatest sensor response. Differences in V_T, μ_h and $I_{on/off}$ between OTFTs pre- and post-exposure are displayed in **Figure 2.4**. Characteristic OTFT output curves and transfer curves post-THC exposure can be found in **Figure 2.8** and **2.9** (**Supporting Information**), respectively. A two-way ANOVA was performed on the results to analyze their statistical significance to a 95% confidence level, and the results of the pair-wise comparisons can be found in **Table 2.4** (**Supporting Information**).

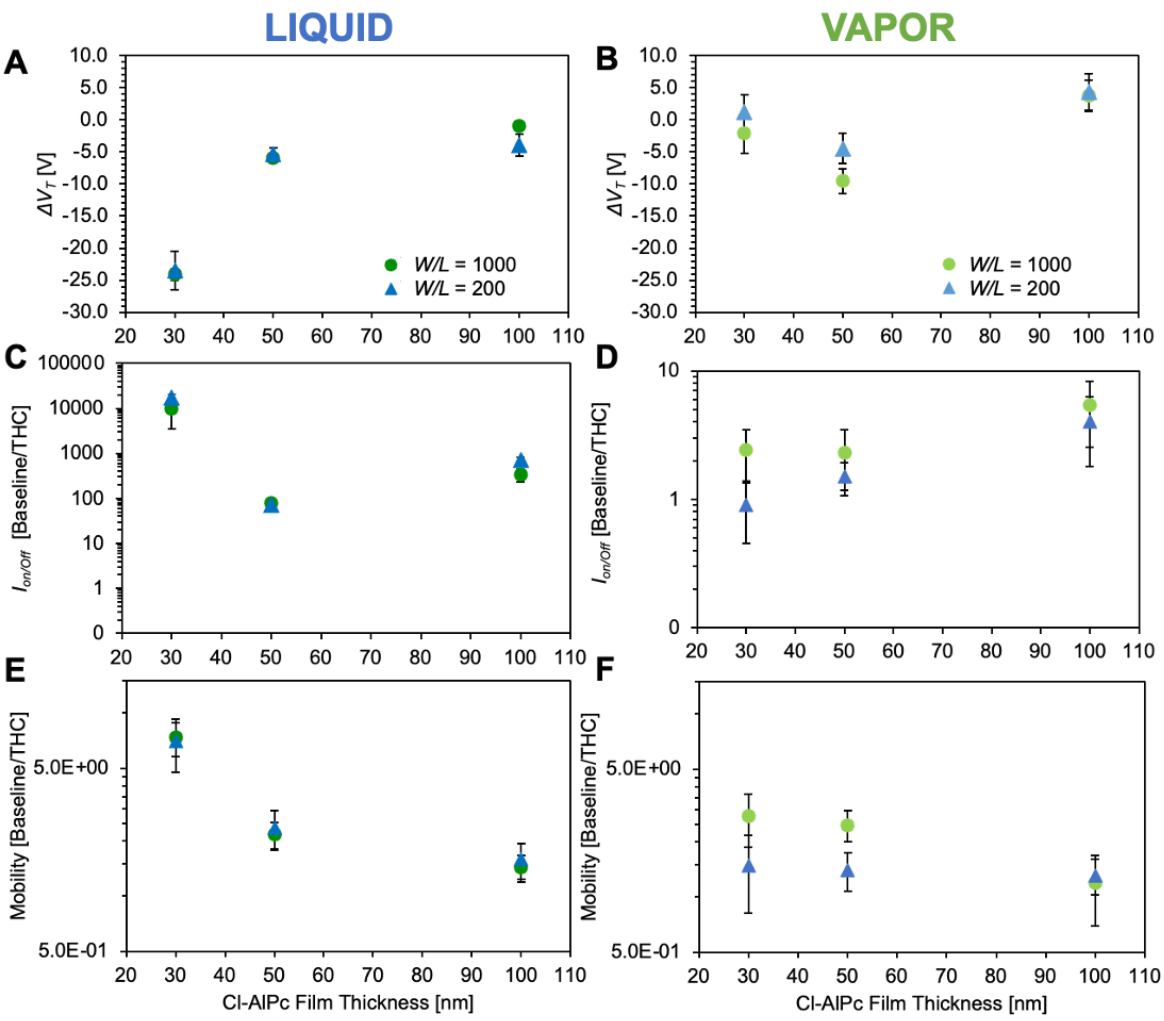

Figure 2.4. *Cl-AlPc OTFT based sensor characteristics when exposed to THC solution (A, C, and E) and THC vapor (B, D and F). The device performance changes are reported as the difference from the baseline device and the exposed device for V_T, (A and B), and a ratio from the baseline and the exposed device for $I_{on/off}$, (C and D), and μ_h, (E and F). The axes of (C) and (D) have been plotted on different scales to better frame the data. Points represent the means of a minimum of 4 devices and error bars represent standard deviation. Significance of data has been analyzed by two-way ANOVA and can be found in Table 2.3.*

As illustrated in **Figure 2.4**, exposure to THC solution led to a reduction in V_T, μ_h and $I_{on/off}$ for all devices, however a significantly larger change was observed for the 30 nm devices, indicating that a thinner semiconductor layer is more sensitive to THC in solution. The devices were less sensitive to THC vapor; although a slight reduction in $I_{on/off}$ current was still observed, with no trend as a function of film thickness. A reduction in μ_h was also observed in response to THC vapor, with a greater response from the 30 nm film compared to the 100 nm film. This result was expected, as previous OTFT gas

sensors have shown greater sensitivities with thinner semiconductor films.[32,42,43] Channel architecture (*W*/*L*) did not appear to influence OTFT performance when exposed to THC solution. Contrastingly, the *W*/*L* appears to have a slight effect on the sensitivity of the OTFTs to vapor THC. The *W*/*L* of 1000 exhibited marginally larger changes in V_T, $I_{on/off}$, and μ_h, with this effect more pronounced in the thinner films than the 100 nm film. This was determined to be statistically significant. This effect has been demonstrated previously, where channels with larger widths lead to more sensitive gas sensors due to their larger surface area for sensing interactions to occur.[44] Exposing the OTFTs to pure hexanes as a blank solvent control leads to no change in device performance, as we have previously illustrated.[6] This suggests that the Cl-AlPc OTFTs are sensitive not only to the analyte but also the form in which the analyte is exposed to the sensor. In both forms of THC exposure, vapor and solution, the devices with the more ideal baseline transfer curves led to the greater response; the 30 nm devices or a *W*/*L* of 1000.

The same experiments were performed with solution and vapor CBD, the results of which can be found in **Figure 2.10** (**Supporting Information**). The sensitivity to CBD was similarly strongly dependent on film thickness, particularly to solution samples, while the channel architecture had little to no effect on sensitivity.

Cl-AlPc films were further characterized by GIWAXS post-exposure to THC solution and vapor with their spectra shown in **Figure 2.5** and **2.11** (**Supporting Information**). For the 30 nm films, the primary alignment of the molecules remains at 30° to the substrate surface, and no new molecular orientations appear upon exposure to THC. However, the corresponding AFM images in **Figure 2.5**, show a slight increase in grain sizes and disordering after exposure to THC, with some slight roughening of the films from RMS = 5.69 nm to RMS = 6.57 nm for samples exposed to THC solution and RMS = 7.11 nm for samples exposed to THC vapor, with similar trends observed for the 100 nm films (**Figure 2.11, Supporting Information**).

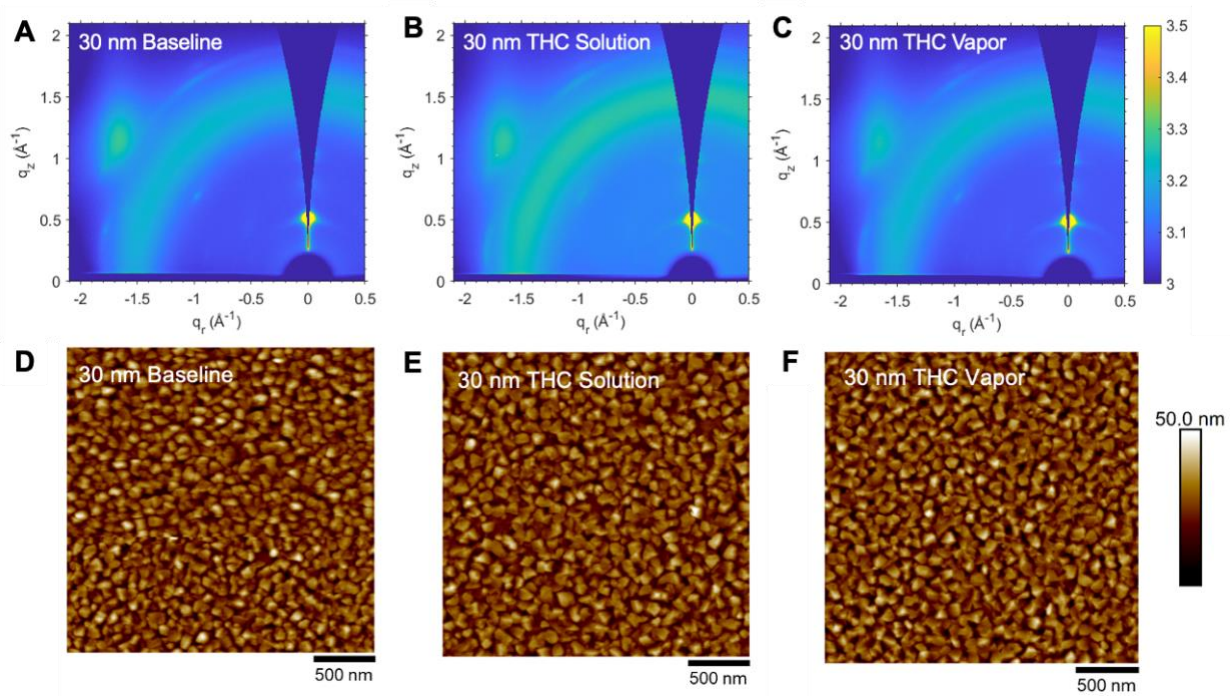

***Figure 2.5**. 2D scattering patterns (θ = 0.3°) of (A) unexposed baseline, (B) THC solution exposed, and (C) THC vapor exposed 30 nm thick Cl-AlPc. AFM images of (D) unexposed baseline, (E) THC solution exposed, and (F) THC vapor exposed 30 nm thick Cl-AlPc with scale bars of 500 nm.*

Unlike the 30 nm and 100 nm films, the 50 nm films by GIWAXS demonstrated some molecular reorganization upon exposure to a liquid THC solution and THC vapor as shown in **Figure 2.6**. Upon exposure to liquid THC solution, the film appeared to become more ordered, reflected by the sharper signals in the GIWAXS spectra and diffraction patterns. This can also be observed in the AFM images. The roughness of the film decreased from a baseline of RMS = 9.49 nm to 8.02 nm after exposure, resulting in a more uniform, ordered film upon exposure to THC in solution. The vapor-exposed film also experienced a slight decrease in surface roughness (RMS = 8.86 nm) and increase in grain order. Additionally, the 50 nm vapor-exposed films demonstrated small changes in the molecular orientation of Cl-AlPc, with a slight shift of the (004) peak from a baseline of q = 1.92 Å^{-1} to q = 1.85 Å^{-1} (**Figure 2.12, Supporting Information**). This suggests that the rougher grains of the 50 nm films are more susceptible to THC vapor-induced molecular reorganization, resulting in a new polymorph which is not observed in the thinner 30 nm or thicker 100 nm films.

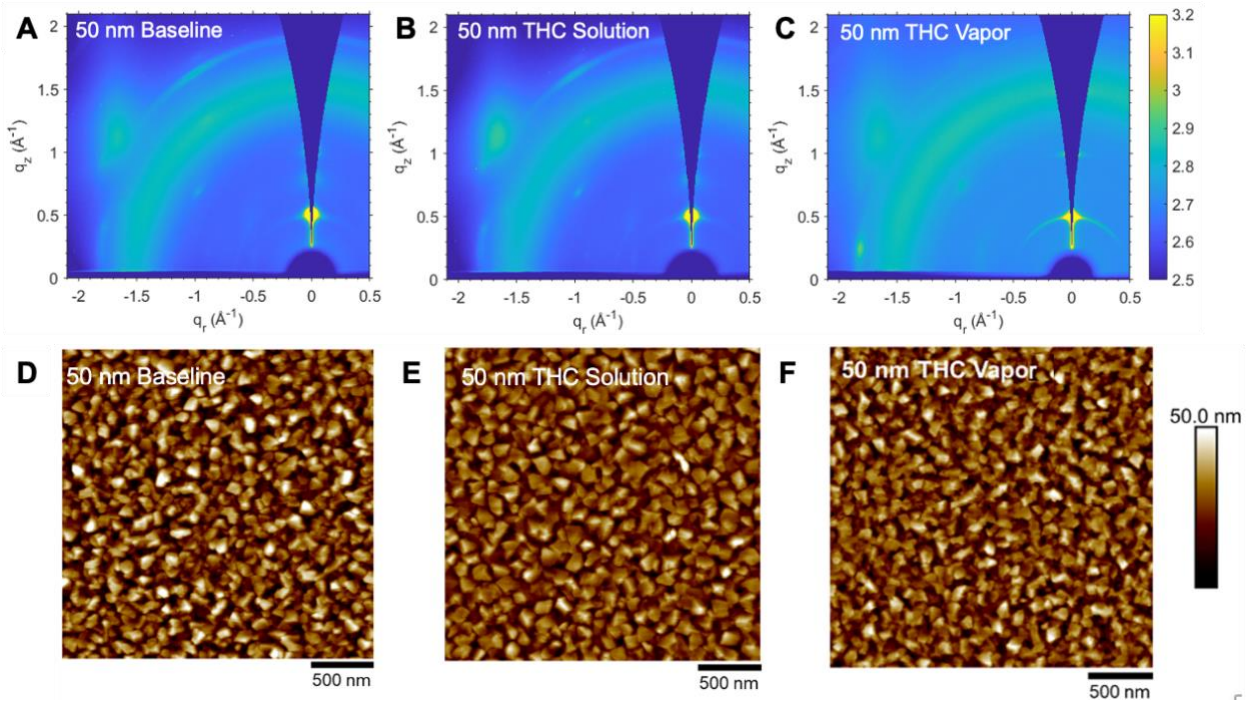

Figure 2.6. *2D scattering patterns (θ = 0.3°) of (A) unexposed baseline, (B) THC solution exposed, and (C) THC vapor exposed 50 nm thick Cl-AlPc. AFM images of (D) unexposed baseline, (E) THC solution exposed, and (F) THC vapor exposed 50 nm thick Cl-AlPc with scale bars of 500 nm.*

Notably, small shifts in molecular orientation of the 50 nm films did not produce significant changes in the performance of OTFT sensors. Additionally, the absence of interactions between the 30 nm and 100 nm films and THC by GIWAXS further suggests that the detection mechanism of THC is not purely physical. AFM results demonstrated a slight change in film roughness, more substantial for THC solution, which is accompanied by an increase in detection sensitivity (**Figure 2.4**). The results from the OTFT sensors emphasize that film thickness plays an important role in sensitivity to THC in solution, while *W*/*L* imparts a negligible effect in comparison. Jiang *et al.* demonstrated that sensitivity to NO_2 increased with decreasing CuPc film thickness, suggesting that thinner films afford increased analyte interaction with the semiconductive/dielectric interface.[32] This has been observed for different semiconductor materials as well.[43] As a much larger, pi-conjugated organic molecule, THC is less likely to permeate throughout the film and therefore the process is likely a charge transfer interaction as THC interacts between grain boundaries and the top layer of the Cl-AlPc film. Thinner films facilitate quicker diffusion of charge and as the surface roughness increases, there are more opportunities for the Pc–analyte interaction on the top layer of the film.

For liquid solution THC sensing, the most sensitive devices were those with the most ideal baseline transfer characteristics and most ideal transport of charge through the device. The fastest baseline charge transport did not necessarily result in the most sensitive THC sensors. This effect was less pronounced, but still present for vapor THC sensing. This finding suggests that we should prioritize the reduction of channel and contact resistances during channel architecture design and device fabrication, and the formation of ordered grains in the thin film to produce quality charge transport pathways for high-performing and sensitive THC sensors. Upon exposure to THC, the changes to more ideal transport pathways are more pronounced, especially in thinner films where less transport pathways are available. These results suggest that THC OTFT sensors can be engineered to be more effective for both solution and vapor THC testing, and that the environment or type of THC exposure will lead to different changes in device response.

2.6 Conclusion

We optimized Cl-AlPc OTFTs by changing the source-drain electrode configuration (W/L) and the film thickness. We found that increasing the W/L leads to improved mobilities and I_{on}, but worse transfer curve characteristics. A W/L of 1000 balances the contact and channel resistances to give the best performance with favorable transfer characteristics. It was found to have a limited effect on the sensitivity to THC. An analysis of the different film thicknesses through GIWAXS and AFM showed that the 30 nm films likely had improved charge transport pathways due to higher grain ordering, which led to improved transfer characteristics and sensitivity to THC in solution. The 100 nm films likely had an increased number of charge transport pathways leading to higher mobilities and I_{on} with disordered grains and worse transfer characteristics, resulting in less sensitive THC sensors. No change in molecular orientation was detected with exposure to THC solution and vapor for the 30 nm and 100 nm films. A slight change was observed for the 50 nm film, but this did not lead to a significant change in performance as an OTFT sensor compared to the other films, indicating that the method of detection of THC and Cl-AlPc is likely not solely dependent on physical changes in the thin film. AFM suggests a slight roughening of the Cl-AlPc film with exposure to THC solution leading to a greater surface area, which could contribute to the overall change in device performance. This

study suggests that film thickness plays an important role in the quality of the charge transport pathways in Cl-AlPc OTFTs, which can influence the sensitivity to THC.

2.7 Experimental Section

2.7.1 Materials

Cl-AlPc was obtained from TCI Chemicals and purified by train sublimation before use. (Octyl)trichlorosilane (OTS, 97%) was purchased from TCI Chemicals and used as received. All solvents were HPLC grade and purchased from Fischer Scientific. Cannabinoid standards were obtained from Toronto Research Chemicals.

2.7.2 Thin Film Formation

Prefabricated devices were purchased from Fraunhofer IPMS to make BGBC transistors. Each substrate consisted of a 230 nm thermally grown SiO_2 dielectric on a Si gate, with prepatterned gold source-drain electrodes to give five different device architectures: W/L = 100 (W = 2 mm, L = 20 µm), W/L = 200 (W = 2 mm, L = 10 µm), W/L = 400 (W = 2 mm, L = 5 µm), W/L = 800 (W = 2 mm, L = 2.5 µm), and W/L = 1000 (W = 10 mm, L = 10 µm). For AFM and GIWAXS characterization, substrates were purchased from Ossila with 300 nm thermally grown SiO_2 dielectric on Si. The substrates were thoroughly washed with acetone to remove the photoresist, then rinsed with isopropanol and dried under a N_2 gas stream. The substrates then underwent an air plasma treatment for 15 minutes, after which time they were briefly rinsed with water, isopropanol, and dried again with N_2. The substrates were submerged in a 1% v/v OTS solution in toluene at 70 °C for 1 hour. The treated substrates were then rinsed with toluene and isopropanol before being dried with a N_2 gas stream and a further drying step in a 70 °C vacuum oven for 1 hour. The substrates were then heated to 140 °C in an Angstrom EvoVac thermal evaporator at a pressure below 2×10^{-6} Torr and held for 1 hour. Next, Cl-AlPc was deposited onto the surface by sublimation at a rate of 0.2 Å s^{-1}. An *in situ* servo shutter mask was used to progressively block the plume during fabrication so that all samples were exposed to the same plume at early stages but that some samples were blocked off at early stages and others were blocked when more material could be deposited to form the desired thicknesses of 300 Å, 500 Å, or 1000 Å.

After deposition was completed, the substrates were cooled to room temperature before characterization.

2.7.3 GIWAXS Characterization

GIWAXS experiments were completed at the Canadian Light Source (CLS) in Saskatoon, Canada using the Brockhouse Diffraction Sector (BXDS) beamline with a photon energy of 15.1 keV. A Rayonix MX300 CCD detector (73.242 μm × 73.242 μm pixel size) placed 417 mm from the sample was used to collect 2D scattering patterns at an angle of incidence of θ = 0.3°. Silver behenate and poly(3-hexylthiophene-2,5-diyl) standards were used to calibrate the data, which was analyzed with the GIXSGUI software package in MATLAB, where both polarization and solid-angle corrections were applied.[45]

2.7.4 AFM

AFM measurements (2.5 μm × 2.5 μm) were carried out with a Bruker Dimension Icon AFM equipped with ScanAsyst-Air tips using tapping mode and a scan rate of 0.69 Hz. Image processing and editing was performed with NanoScope Analysis v.1.8 software.

2.7.5 OTFT Characterization

Transistors with *W*/*L* ratios of 100 to 800 were characterized using a custom electrical probe station, oesProbe A10000-P290 (Element instrumentation Inc. & Kreus Design Inc.), and transistors with a *W*/*L* ratio of 1000 were tested using a custom-built auto tester apparatus. Both were run using a Keithley 2614B SourceMeter and Labview software, where the V_{SD} and V_{GS} were set to discrete values and the I_{SD} was measured. To saturate the devices, six transfer curves were obtained and the final three were averaged to yield the characteristic transfer curve for each transistor, as shown in Fig. S1 and S3.‡ The V_T and $I_{on/off}$ was determined from these measurements, and the μ_h was determined using the general expression relating it to the gate voltage in the saturation region, shown again in **Equation 2.1**.

$$I_{SD} = \frac{\mu C_i W}{2L}(V_{GS} - V_T)^2 \quad (2.1)$$

The baseline values for V_T, $I_{on/off}$ and μ_h were obtained for all devices to assess which semiconductor thickness and channel architecture resulted in the best device performance, and these characteristics were averaged across a minimum of 4 devices for each condition.

$$\frac{R_T W}{L} = \frac{1}{\mu C_i (V_{GS} - V_T)} + R_C W \left(\frac{1}{L}\right), where\ R_T = \frac{dV_{DS}}{dI_{DS}}|_{V_{DS} \to 0V} \quad (2.2)$$

Contact resistance was calculated by the M-TLM shown in **Equation 2.2**. The total resistance (R_T) was obtained from the output curve at a low source-drain voltage. A plot of $R_T W/L$ *vs.* $1/L$ was generated for the channel lengths of 2.5, 5, 10, and 20 µm. The data was fit with a linear trendline, the slope of which gave the width-normalized contact resistance, $R_C W$.

Following, the devices were exposed to either to a liquid THC solution or THC vapor. For solution exposure, 0.5 µL of a 20 µM solution of THC in hexanes was drop-cast onto the surface of each transistor channel and allowed to dry for 2 minutes. For vapor exposure, 36 mg of THC was vaporized into an 8 L bag (4.5 mg L^{-1}) using the Vapormed Volcano Medic. The bag was slowly emptied into a small chamber housing the devices where they were exposed to the vapor for a total of 90 seconds. The devices were then characterized again, and new V_T, $I_{on/off}$ and μ_h values were obtained and compared to the baseline values to assess which devices and channel architectures resulted in the highest sensitivity to THC. The procedure was repeated for CBD solution and CBD vapor.

2.7.6 ANOVA Statistical Analysis

The two-way ANOVA analysis was performed using GraphPad's Prism software. All I_{on} and μ_h values for baseline devices, and all changes in V_T, $I_{on/off}$ and μ_h for THC-exposed devices were input in the software as grouped data. A two-way ANOVA analysis was performed fitting main effects. The Tukey test was used to compare all data pairs individually. The effect of W/L and thickness was reported for the overall data set and all pairs using an α of 0.05 (95% confidence interval), and the results were tabulated.

2.8 Acknowledgments

This work was supported by NSERC Discovery grant RGPIN 2015-05796 (A. J. S.), 2015-05453 (C. S. H.), and 2020-04079 (B. H. L.), the Canada Research Chairs Program 950-230754 (A. J. S.) and 950-230724 (B. H. L.). Infrastructure used to complete this work was acquired using CFI-JELF #30488 (B. H. L.) and NSERC RTI 472921-2015 (B. H. L.). We recognize the Centre for Research in Photonics at the University of Ottawa (CRPuO) for allowing access to the AFM. The authors express gratitude to the CLS for granting beamtime, and to Adam Leontowich for his technical support and proficiency during data collection. CLS is supported by CFI, NSERC, the University of Saskatchewan, the Government of Saskatchewan, Western Economic Diversification Canada, the National Research Council Canada, and the Canadian Institutes of Health Research.

2.9 Supporting Information

Table 2.1. *Device characteristics of Cl-AlPc OTFTs with different device structures.*

W/L [a)]	Thickness [a)] [nm]	I_{on} [b)] [10^{-4} A]	$I_{on/off}$ [b)]	μ_h [b)] [10^{-2}cm^2/Vs]	H [b)] [V]	V_T [b)] [V]
100	30	0.38 ± 0.04	10^4	2.3 ± 0.2	4.03 ± 0.002	-0.9 ± 0.8
	50	0.70 ± 0.07	10^4	3.3 ± 0.3	7.14 ± 0.004	10.7 ± 1.1
	100	0.82 ± 0.03	10^3	3.9 ± 0.1	10.42 ± 0.67	30.5 ± 1.1
200	30	1.0 ± 0.1	10^4	2.6 ± 0.1	6.72 ± 0.002	7.2 ± 0.7
	50	1.9 ± 0.2	10^4	4.1 ± 0.5	9.29 ± 0.82	13.0 ± 0.7
	100	2.1 ± 0.1	10^3	5.3 ± 0.5	11.09 ± 0.67	33.2 ± 0.7
400	30	1.8 ± 0.4	10^4	2.2 ± 0.4	8.74 ± 0.78	13.2 ± 0.7
	50	4.7 ± 0.7	10^4	5.2 ± 0.8	10.00 ± 0.10	15.7 ± 0.8
	100	6.2 ± 0.2	10^3	8.3 ± 0.4	11.09 ± 0.67	29.2 ± 0.7
800	30	3.3 ± 0.5	10^4	1.9 ± 0.3	9.41 ± 0.004	12.6 ± 1.3
	50	13 ± 2	10^4	6.9 ± 0.9	11.07 ± 0.71	20.0 ± 0.8
	100	14 ± 0.3	10^3	9.9 ± 0.2	13.11 ± 0.67	31.9 ± 0.7
1000	30	40 ± 0.8	10^5	43 ± 2	4.47 ± 0.93	-5.7 ± 1.5
	50	67 ± 2	10^5	71 ± 3	2.59 ± 0.50	-8.0 ± 0.8
	100	45 ± 4	10^5	57 ± 5	2.35 ± 0.55	-12.0 ± 0.8

[a)] OTFTs with following structure Si (gate), 230 nm SiO_2 (dielectric), ITO adhesion layer with gold source drain electrodes with different width/length ratios and different thicknesses of Cl-AlPc (semiconductor).

[b)] On current (I_{on}), on and off current ratio ($I_{on/off}$), hole mobility (μ_h), hysteresis (H), and threshold voltage (V_T). All values were averaged from a minimum of four devices.

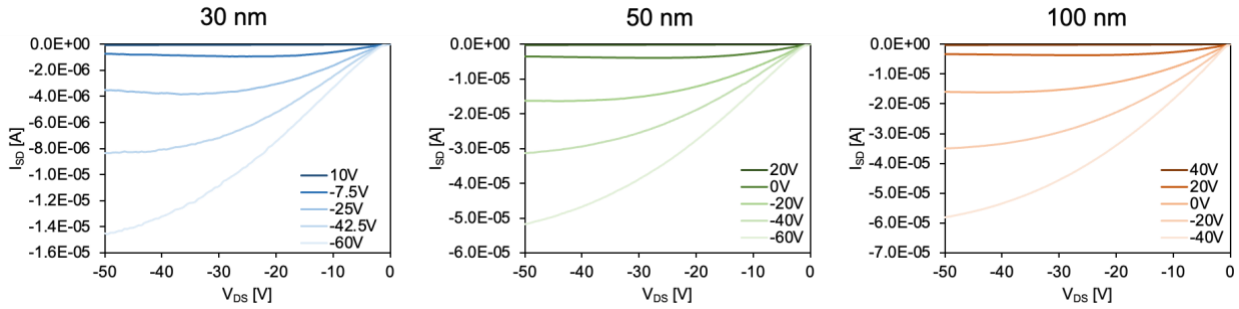

Figure 2.7*. Characteristic output curves (A, B, C) were taken for the OTFTs with W/L = 200 for comparison. Cl-AlPc film thickness was varied from 30 nm (A), 50 nm (B) and 100 nm (C).*

Table 2.2. *Two-way ANOVA analysis of the effect of W/L and thickness, with individual interactions assessed using the Tukey test, for baseline device I_{on} and μ_h using a 95% confidence interval (α = 0.05). Significant interactions are shown in green, and non-significant interactions are shown in red. The analysis was performed using GraphPad's Prism software using the extracted average and SD of I_{on} and μ_h for each W/L and thickness.*

Baseline I_{on}

***W/L* Constant**	30 nm → 50 nm	30 nm → 100 nm	50 nm → 100 nm
W/L = 100	*	n.s.	*
W/L = 200	*	n.s.	*
W/L = 400	*	n.s.	*
W/L = 800	*	n.s.	*
W/L = 1000	*	n.s.	*
Thickness Constant	30 nm	50 nm	100 nm
100 → 200	n.s.	n.s.	n.s.
100 → 400	n.s.	n.s.	n.s.
100 → 800	*	*	*
100 → 1000	*	*	*
200 → 400	n.s.	n.s.	n.s.
200 → 800	n.s.	n.s.	n.s.
200 → 1000	*	*	*
400 → 800	n.s.	n.s.	n.s.
400 → 1000	*	*	*
800 → 1000	*	*	*

Baseline μ_h

***W/L* Constant**	30 nm → 50 nm	30 nm → 100 nm	50 nm → 100 nm
W/L = 100	*	*	n.s.
W/L = 200	*	*	n.s.
W/L = 400	*	*	n.s.
W/L = 800	*	*	n.s.
W/L = 1000	*	*	n.s.
Thickness Constant	30 nm	50 nm	100 nm
100 → 200	n.s.	n.s.	n.s.
100 → 400	n.s.	n.s.	n.s.
100 → 800	n.s.	n.s.	n.s.
100 → 1000	*	*	*
200 → 400	n.s.	n.s.	n.s.
200 → 800	n.s.	n.s.	n.s.
200 → 1000	*	*	*
400 → 800	n.s.	n.s.	n.s.
400 → 1000	*	*	*
800 → 1000	*	*	*

* = $p < 0.05$, significant
n.s. = not significant

Table 2.3. *Contact resistance (R_C) and width-normalized contact resistance (R_CW) for OTFTs with CI-AlPc film thickness of 30 nm, 50 nm, and 100 nm.*

	30 nm	**50 nm**	**100 nm**
R_C [Ω]	43 244 000	3 750 000	1 420 400
R_CW [Ω cm]	865 000	75 000	28 400

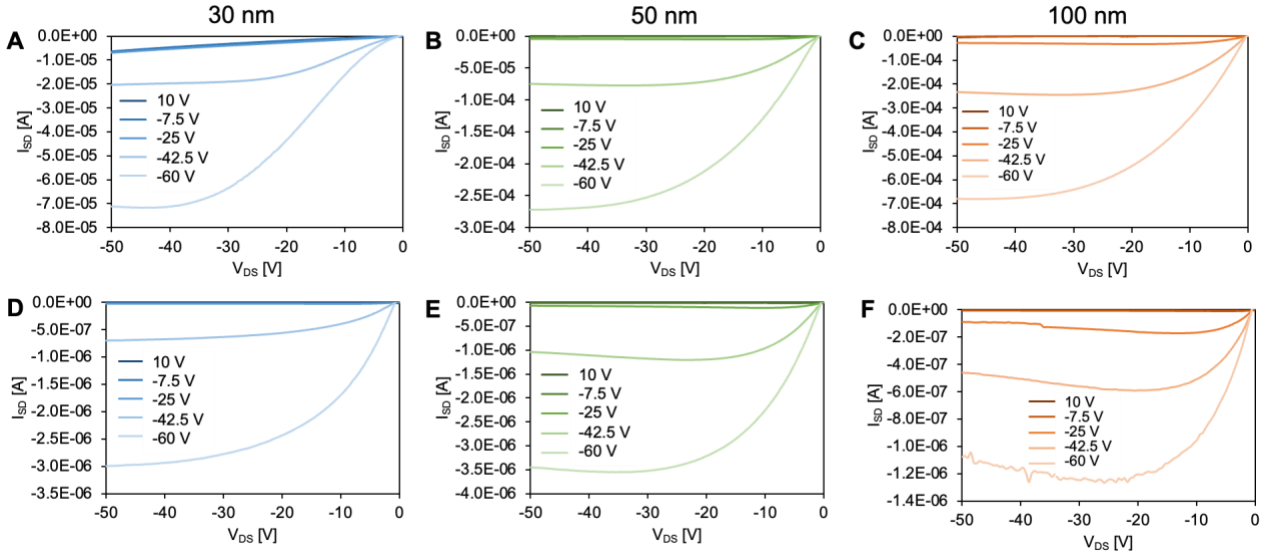

Figure 2.8. *Output curves for CI-AlPc BGBC OTFT THC sensors exposed to a THC solution (A, B, C) and to THC vapor (D, E, F). CI-AlPc film thickness was varied from 30 nm (A, D), 50 nm (B, E) and 100 nm (C, F). As a comparison all output curves are for devices with W/L = 200.*

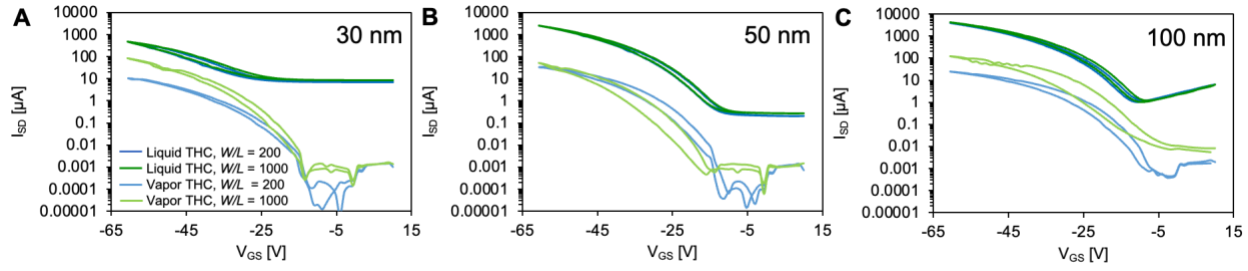

Figure 2.9. *Transfer curves for CI-AlPc BGBC OTFT THC sensors for different W/L between 200 and 1000. CI-AlPc film thickness was varied from 30 nm (A), 50 nm (B) and 100 nm (C). V_{SD} for all transfer curves was -50 V.*

Table 2.4. *Two-way ANOVA analysis of the effect of W/L and thickness, with individual interactions assessed using the Tukey test, for liquid THC and vapor THC-exposed devices for V_T, $I_{on/off}$, and μ_h using a 95% confidence interval (α = 0.05). Significant interactions are shown in green, and non-significant interactions are shown in red. The analysis was performed using GraphPad's Prism software using the extracted average and SD of V_T, $I_{on/off}$, and μ_h for each W/L and thickness.*

V_T – Liquid THC			
***W/L* Constant**	30 nm → 50 nm	30 nm → 100 nm	50 nm → 100 nm
W/L = 200	*	*	n.s.
W/L = 1000	*	*	n.s.
Thickness Constant	30 nm	50 nm	100 nm
200 → 1000	n.s.	n.s.	n.s.
V_T – Vapor THC			
W/L Constant	30 nm → 50 nm	30 nm → 100 nm	50 nm → 100 nm
W/L = 200	*	*	*
W/L = 1000	*	*	*
Thickness Constant	30 nm	50 nm	100 nm
200 → 1000	*	*	*
$I_{on/off}$ – Liquid THC			
***W/L* Constant**	30 nm → 50 nm	30 nm → 100 nm	50 nm → 100 nm
W/L = 200	*	*	n.s.
W/L = 1000	*	*	n.s.
Thickness Constant	30 nm	50 nm	100 nm
200 → 1000	*	*	*
$I_{on/off}$ – Vapor THC			
***W/L* Constant**	30 nm → 50 nm	30 nm → 100 nm	50 nm → 100 nm
W/L = 200	n.s.	*	*
W/L = 1000	n.s.	*	*
Thickness Constant	30 nm	50 nm	100 nm
200 → 1000	*	*	*
Mobility – Liquid THC			
***W/L* Constant**	30 nm → 50 nm	30 nm → 100 nm	50 nm → 100 nm
W/L = 200	*	*	n.s.
W/L = 1000	*	*	n.s.
Thickness Constant	30 nm	50 nm	100 nm
200 → 1000	n.s.	n.s.	n.s.
Mobility – Vapor THC			
***W/L* Constant**	30 nm → 50 nm	30 nm → 100 nm	50 nm → 100 nm
W/L = 200	n.s.	*	*
W/L = 1000	n.s.	*	*
Thickness Constant	30 nm	50 nm	100 nm
200 → 1000	*	*	*

* = $p < 0.05$, significant
n.s. = not significant

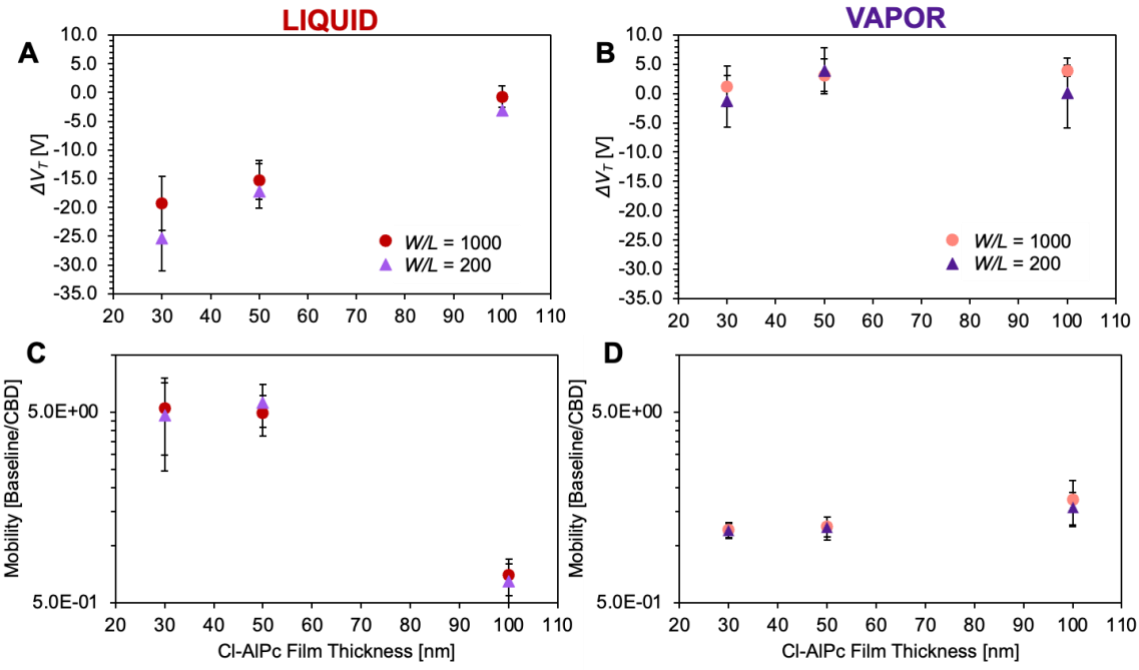

Figure 2.10. *Cl-AlPc OTFT based sensor characteristics when exposed to CBD solution (A, C), and CBD vapor (B, D). The device performance changes are reported as differences from the baseline device and the exposed device for V_T (A, B), and a ratio from the baseline and the exposed device for mobility (C, D). Points represent the means of a minimum of 4 devices and error bars represent standard deviation.*

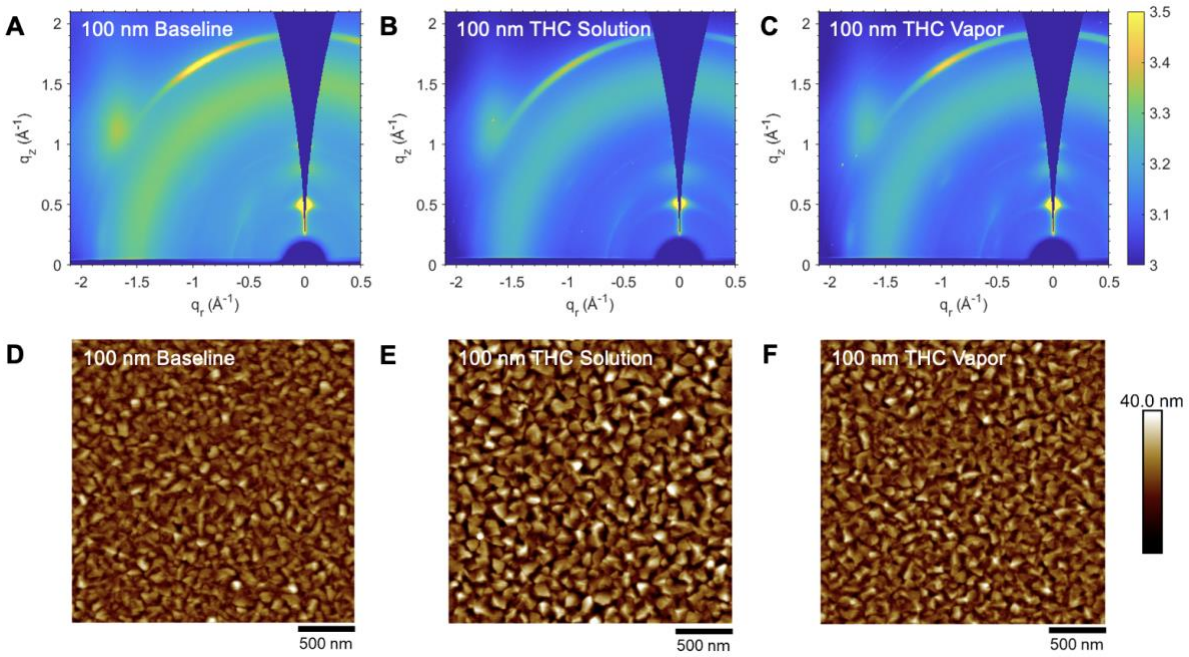

Figure 2.11. *2D scattering patterns (θ = 0.3°) of (A) unexposed baseline, (B) THC solution exposed, and (C) THC vapor exposed 100 nm thick Cl-AlPc. AFM images of (D) unexposed baseline (RMS = 5.06 nm), (E) THC solution exposed (RMS = 7.58 nm), and (F) THC vapor exposed (RMS = 5.26 nm) 100 nm thick Cl-AlPc with scale bars of 500 nm.*

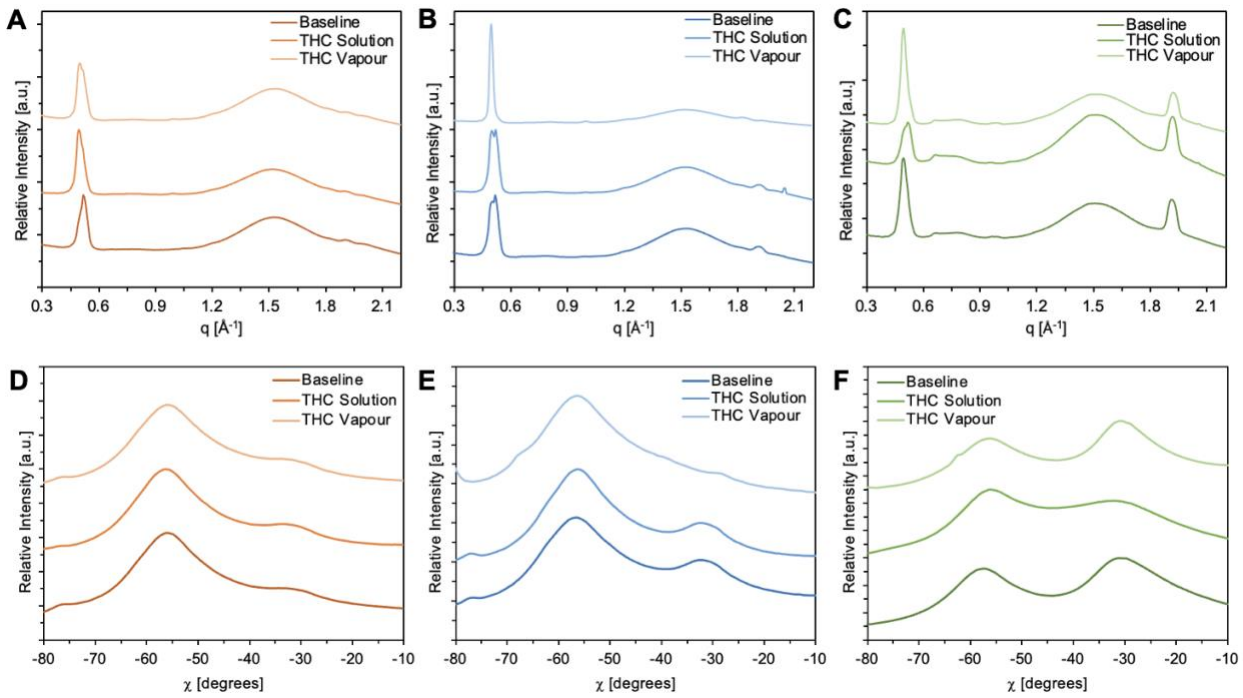

Figure 2.12. *Diffraction patterns (A, B, C) and linecut profiles with respect to χ between a q of 1.9-2.1 Å^{-1} (D, E, F) of 30 nm (A, D), 50 nm (B, E) and 100 nm (C, F) thick Cl-AlPc exposed to THC solution and vapor.*

2.10 References

[1] A. DI, *Eur. J. Intern. Med.* **2018**, *49*, 7.

[2] R. Mechoulam, M. Peters, E. Murillo-Rodriguez, L. O. Hanuš, *Chem. Biodiversity* **2007**, *4*, 1678.

[3] B. De Backer, B. Debrus, P. Lebrun, L. Theunis, N. Dubois, L. Decock, A. Verstraete, P. Hubert, C. Charlier, *J. Chromatogr. B* **2009**, *877*, 4115.

[4] C. Sun, Y. X. Wang, M. Sun, Y. Zou, C. Zhang, S. Cheng, W. Hu, *Biosens. Bioelectron.* **2020**, *164*, 112251.

[5] C. Sun, R. Li, Y. Song, X. Jiang, C. Zhang, S. Cheng, W. Hu, *Anal. Chem.* **2021**, *93*, 6188.

[6] Z. J. Comeau, N. T. Boileau, T. Lee, O. A. Melville, N. A. Rice, Y. Troung, C. S. Harris, B. H. Lessard, A. J. Shuhendler, *ACS Sens.* **2019**, *4*, 2706.

[7] J. Jo, J. S. Yu, T. M. Lee, D. S. Kim, *Jpn. J. Appl. Phys.* **2009**, *48*, 04C181.

[8] G. Grau, R. Kitsomboonloha, S. L. Swisher, H. Kang, V. Subramanian, *Adv. Funct. Mater.* **2014**, *24*, 5067.

[9] J. Kim, T. Hassinen, W. H. Lee, S. Ko, *Org. Electron.* **2017**, *42*, 361.

[10] Z. Lin, X. Guo, L. Zhou, C. Zhang, J. Chang, J. Wu, J. Zhang, *Org. Electron.* **2018**, *54*, 80.

[11] Y. Y. Noh, N. Zhao, M. Caironi, H. Sirringhaus, *Nat. Nanotechnol.* **2007**, *2*, 784.

[12] H. Y. Tseng, V. Subramanian, *Org. Electron.* **2011**, *12*, 249.

[13] A. De La Fuente Vornbrock, D. Sung, H. Kang, R. Kitsomboonloha, V. Subramanian, *Org. Electron.* **2010**, *11*, 2037.

[14] H. Kang, R. Kitsomboonloha, J. Jang, V. Subramanian, *Adv. Mater.* **2012**, *24*, 3065.

[15] J. T. Mabeck, G. G. Malliaras, *Anal. Bioanal. Chem.* **2006**, *384*, 343.

[16] P. Lin, F. Yan, P. Lin, F. Yan, *Adv. Mater.* **2012**, *24*, 34.

[17] M. Wu, S. Hou, X. Yu, J. Yu, *J. Mater. Chem. C* **2020**, *8*, 13482.

[18] M. E. Roberts, A. N. Sokolov, Z. Bao, *J. Mater. Chem.* **2009**, *19*, 3351.

[19] J. Locklin, Z. Bao, *Anal. Bioanal. Chem.* **2006**, *384*, 336.

[20] J. N. Arthur, A. K. Pandey, J. M. Nunzi, S. D. Yambem, *ACS Appl Mater Interfaces* **2022**, *14*, 5709.

[21] O. A. Melville, B. H. Lessard, T. P. Bender, *ACS Appl Mater Interfaces* **2015**, *7*, 13105.

[22] D. Elkington, N. Cooling, W. Belcher, P. C. Dastoor, X. Zhou, *Electronics* **2014**, *3*, 234.

[23] M. Urbani, M. E. Ragoussi, M. K. Nazeeruddin, T. Torres, *Coord. Chem. Rev.* **2019**, *381*, 1.

[24] G. de la Torre, G. Bottari, T. Torres, *Adv. Energy Mater.* **2017**, *7*, 1601700.

[25] R. R. Cranston, B. H. Lessard, *RSC Adv.* **2021**, *11*, 21716.

[26] Z. J. Comeau, N. A. Rice, C. S. Harris, A. J. Shuhendler, B. H. Lessard, *Adv. Funct. Mater.* **2022**, *32*, 2107138.

[27] N. T. Boileau, R. Cranston, B. Mirka, O. A. Melville, B. H. Lessard, *RSC Adv.* **2019**, *9*, 21478.

[28] B. H. Lessard, *ACS Appl Mater Interfaces* **2021**, *13*, 31321.

[29] D. Klyamer, A. Sukhikh, S. Gromilov, P. Krasnov, T. Basova, *Sensors* **2018**, *18*, 2141.

[30] N. T. Boileau, O. A. Melville, B. Mirka, R. Cranston, B. H. Lessard, *RSC Adv.* **2019**, *9*, 2133.

[31] Z. J. Comeau, G. A. Facey, C. S. Harris, A. J. Shuhendler, B. H. Lessard, *ACS Appl. Mater. Interfaces* **2020**, *12*, 50692.

[32] Y. Jiang, W. Huang, X. Zhuang, Y. Tang, J. Yu, *Mater. Sci. Eng. B* **2017**, *226*, 107.

[33] A. Demir, S. Bałci, S. E. San, Z. Dołruyol, *Surface Review and Letters* **2015**, *22*, DOI 10.1142/S0218625X15500389.

[34] R. Ruiz, A. Papadimitratos, A. C. Mayer, G. G. Malliaras, *Adv. Mater.* **2005**, *17*, 1795.

[35] B. King, O. A. Melville, N. A. Rice, S. Kashani, C. Tonnelé, H. Raboui, S. Swaraj, T. M. Grant, T. McAfee, T. P. Bender, H. Ade, F. Castet, L. Muccioli, B. H. Lessard, *ACS Appl. Electron. Mater.* **2021**, *3*, 325.

[36] P. Kumar, A. Sharma, S. Yadav, S. Ghosh, *Org. Electron.* **2013**, *14*, 1663.

[37] M. Girtan, S. Dabos-Seignon, A. Stanculescu, *Vacuum* **2009**, *83*, 1159.

[38] H. Jung, J. Whan, H. Hwi, J.-J. Hyo Jung Kim, J. Whan Kim, H. Hwi Lee, B. Lee, J.-J. Kim, in *Proc. SPIE*, SPIE, **2012**, p. 84771C.

[39] P. V. Necliudov, M. S. Shur, D. J. Gundlach, T. N. Jackson, *Solid-State Electron.* **2003**, *47*, 259.

[40] H. Klauk, G. Schmid, W. Radlik, W. Weber, L. Zhou, C. D. Sheraw, J. A. Nichols, T. N. Jackson, *Solid-State Electron.* **2003**, *47*, 297.

[41] K. J. Wynne, *Inorg. Chem.* **1984**, *23*, 4658.

[42] B. Nketia-Yawson, Y. Y. Noh, *Macromol. Res.* **2017**, *25*, 489.

[43] T. Xie, G. Xie, H. Du, Y. Zhou, F. Xie, Y. Jiang, H. Tai, *IEEE Sens. J.* **2016**, *16*, 1865.

[44] B. Nketia-Yawson, A. R. Jung, Y. Noh, G. S. Ryu, G. D. Tabi, K. K. Lee, B. Kim, Y. Y. Noh, *ACS Appl Mater Interfaces* **2017**, *9*, 7322.

[45] Z. Jiang, *J. of Appl. Crystallogr.* **2015**, *48*, 917.

Chapter 3: Axial Phenoxylation of Aluminum Phthalocyanines for Improved Cannabinoid Sensitivity in OTFT Sensors

This chapter was adapted from: ***Halynne R. Lamontagne****, Rosemary R. Cranston, Zachary J. Comeau, Cory S. Harris, Adam J. Shuhendler & Benoît H. Lessard, Advanced Science, 2024,* ***11*** *(27), 2305515*
DOI: 10.1002/advs.202305515

3.1 Context

In conjunction with the previous study on Cl-AlPc in **Chapter 2**, I wanted to explore the potential of tuning or enhancing the interactions between Cl-AlPc and THC/CBD to improve the sensing response of our OTFTs. To do this, I utilized simple phenoxylation reactions to replace the axial chlorine with a set of five different substituted phenol groups. The hypothesis was that these groups would introduce new thin film packing motifs and change the thin film morphology to a potentially more favourable arrangement, while maintaining the conjugated MPc core that was found to interact with THC/CBD. Through electrical characterization, I found that while these substitutions led to a slightly decreased initial device performance compared to Cl-AlPc, some improved the overall response to THC and CBD. This coincides with the findings in **Chapter 2**, where high device performance did not lead to improved sensor performance. The reason for the improved sensor response was uncovered from AFM, GIWAXS, XRD and Raman characterization of the various films pre- and post-exposure. The phenoxy-AlPc films often showed evidence of multiple polymorphs present in the thin film, forming a mixed film with often rougher grains, that led to larger changes in overall film roughness and film crystal structure upon exposure to THC and CBD. Additionally, I was able to see shifts in the Raman spectra in the characteristic isoindole region for the phenoxy-AlPcs that were not observed in Cl-AlPc. The enhanced film interactions between THC and CBD and the phenoxy-AlPcs likely drove the improved sensing response of the OTFTs. This work highlights the usefulness of simple substitution reactions to tune the thin film behavior of MPcs to maintain adequate device performance while enhancing the sensing response.

3.2 Contribution of Authors

I synthesized, purified, and characterized all R-AlPc compounds used in this study. I fabricated all devices and substrates used for OTFT and thin-film characterization. I performed all OTFT characterization, cannabinoid exposure studies, OTFT data interpretation, and Raman measurements. RRC performed AFM measurements and assisted in GIWAXS measurements and data analysis. ZJC assisted with cannabinoid exposure studies. I authored the manuscript, and all co-authors assisted with editorial contributions. This work was supervised by AJS and BHL.

3.3 Abstract

Cannabis producers, consumers, and regulators need fast, accurate, point-of-use sensors to detect Δ^9-tetrahydrocannabinol (THC) and cannabidiol (CBD) from both solution and vapor source samples, and phthalocyanine-based organic thin-film transistors (OTFTs) provide a cost-effective solution. Chloro aluminum phthalocyanine (Cl-AlPc) has emerged as a promising material due to its unique coordinating interactions with cannabinoids, allowing for superior sensitivity. This work explores the molecular engineering of AlPc to tune and enhance these interactions, where a series of novel phenxoylated R-AlPcs were synthesized and integrated in OTFTs, which were then exposed to THC and CBD solution and vapor samples. While the R-AlPc substituted molecules had a comparable baseline device performance to Cl-AlPc, their new crystal structures and weakened intermolecular interactions increased sensitivity to THC. Grazing-incidence wide-angle X-ray scattering (GIWAXS) and atomic force microscopy (AFM) were used to investigate this film restructuring, where a significant shift in the crystal structure, grain size, and film roughness was detected for the R-AlPc molecules that did not occur with Cl-AlPc. This significant crystal reorganization and film restructuring is the driving force behind the improved sensitivity to cannabinoids relative to Cl-AlPc and demonstrates that analyte-semiconductor interactions can be enhanced through chemical modification to create more sensitive OTFT sensors.

3.4 Introduction

As countries around the world move to legalize cannabis, there is a growing burden on producers and regulators to accurately measure and monitor the quality of cannabis

products for their cannabinoid content. The two major cannabinoids, Δ^9-tetrahydrocannabinol (THC) and cannabidiol (CBD), have different but specific psychogenic and therapeutic effects on the human body when they are consumed.[1–5] They are also chemically similar, making them difficult to differentiate and measure in samples.[2,6] Currently in industry, this differentiation is often performed by high-performance liquid chromatography (HPLC), an expensive and time-consuming technique that requires trained personnel.[7,8] There is a present need for quick, accurate, point-of-source tests to identify and speciate THC and CBD in a variety of source samples. A demonstrated potential low-cost solution to this problem is the use of phthalocyanine-based organic thin-film transistors (OTFTs).[9–13]

Phthalocyanines (Pcs) are conjugated macrocyclic organic compounds which can chelate a variety of metals and metalloids (MPcs). Their chemical stability, alongside unique spectral and electronic properties, has led to Pc applications as dyes and pigments,[14,15] and as charge transport layers in OTFTs[16–22] and organic photovoltaics (OPVs).[16,23–25] They are inexpensive to synthesize and can easily be chemically modified through peripheral substituents,[26–29] axial substituents[18,30–38] or substituting the central metal.[39] This structural versatility enables the tuning of their physical properties to achieve greater solubility, new crystal polymorphs, desirable film morphology, or improved electronic properties.[14,40–42] For example, the choice of axial groups in silicon phthalocyanines (R_2-SiPc)[43] has enabled the fine tuning of solubility/miscibility,[44] processability,[17] morphology,[18,35,36] and OTFT performance such as threshold voltage[37,38,45] or air stability.[29,46] Pc-based OTFTs have also been used for a variety of liquid and gas sensing applications,[19,47–50] including as cannabinoid sensors to ratiometrically detect and differentiate THC and CBD in plant and vapor samples.[9–13] Our group's previous work has identified that this sensing response arises from a combination of electrochemical and physical interactions between cannabinoids and thin-films of Pcs.[10–13] These interactions lead to a structural change in the Pc film through induced surface crystallization, causing a change in the electrical performance of the OTFT.[11–13] The magnitude and nature of these structural changes varies depending on the MPc, which highlights the importance of both the choice of Pc, and its thin-film structure for the overall performance of an OTFT sensor.

Chloro aluminum phthalocyanine (Cl-AlPc) has demonstrated superior performance as a cannabinoid sensor in previous work.[10,12] Cl-AlPc interacts strongly with cannabinoids both in solution and as a thin-film, leading to a greater change in electrical response.[10,12] The large aluminum atom and the single chloro axial substituent of Cl-AlPc causes the molecule to form an inverted umbrella shape, which exposes its inner ring of nitrogens to interactions with analytes.[10] Cl-AlPc also results in a relatively loose crystal packing structure compared to other divalent MPcs.[51] This open crystal packing can be exploited by switching the Cl- atom for a larger pendant group, changing the crystal structure and further exposing the inner nitrogen ring, potentially leading to more sensitive devices. Phenoxylation is a facile reaction which can be performed on axial halogens of MPcs and which has proven effective at engineering crystals and improving solubility in boron subphthalocyanines (BsubPcs),[24,26,52] a class of MPcs which also have an inverted umbrella molecular shape with a single axial group. Several phenoxylated BsubPcs have emerged in literature where even subtle changes to the phenoxy group, such as a well-placed methyl group or halogen group can lead to significant changes in solubility and crystal orientation, respectively.[53,54] While relatively less explored, the phenoxylation of Cl-AlPc can be carried out under similar conditions[55] and could therefore benefit from such crystal engineering.

Here, we synthesized a series of novel trifluoro- and monomethylphenoxylated aluminum phthalocyanine derivatives (R-AlPc) and integrated them into OTFTs as the semiconducting layer for the first time (**Figure 3.1**). We characterized these R-AlPc compounds in terms of their response to THC and CBD in OTFT based sensors. Grazing-incidence wide-angle X-ray scattering (GIWAXS) and atomic force microscopy (AFM) were used to probe the changes in thin film structure which led to improved sensor performance. Thus, we demonstrate phenoxylation as a straightforward technique to alter the thin film structure and sensitize axially substituted Pc-based OTFTs to analytes without compromising performance.

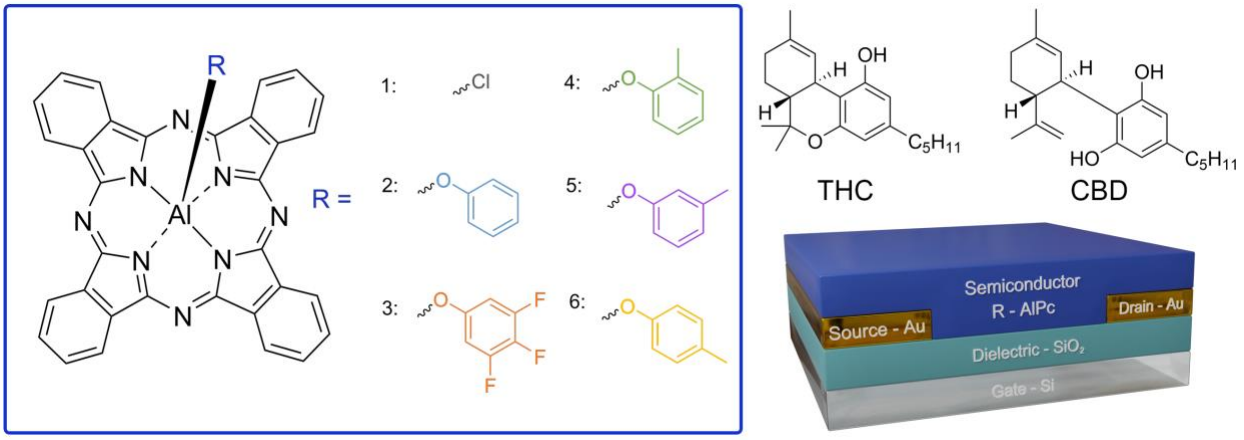

Figure 3.1. *Schematic diagram of the axial phenoxy-AlPcs used as semiconductors in a bottom-gate bottom-contact (BGBC) OTFT cannabinoid sensor, including the structure of THC and CBD. 1: Chloro aluminum phthalocyanine (Cl-AlPc); 2: phenoxy aluminum phthalocyanine (PhO-AlPc); 3: 3,4,5-trifluorophenoxy aluminum phthalocyanine (345F-AlPc); 4: 2-methylphenoxy aluminum phthalocyanine (oCr-AlPc); 5: 3-methylphenoxy aluminum phthalocyanine (mCr-AlPc); 6: 4-methylphenoxy aluminum phthalocyanine (pCr-AlPc).*

3.5 Results and Discussion

3.5.1 Axial Phenoxylation of Aluminum Phthalocyanines

A series of axial phenoxylation coupling reactions were performed on Cl-AlPc by reaction with different phenols at 10-molar excess in chlorobenzene at 125 °C, as outlined by Raboui et al. (**Figure 3.6, Supporting Information**).[55] The reaction conditions and resulting yields for all substitutions performed can be found in **Table 3.1** (**Supporting Information**). The chosen synthesized compounds include phenoxy-AlPc (PhO-AlPc), 3,4,5-trifluorophenoxy-AlPc (345F-AlPc), 2-methylphenoxy-AlPc (oCr-AlPc), 3-methylphenoxy-AlPc (mCr-AlPc), and 4-methylphenoxy-AlPc (pCr-AlPc). These substitutions were chosen to study both the effect of fluorination and methyl position on AlPc film morphology and resulting sensor performance, as both have been found to greatly influence Pc solubility and electrical performance.[29,38,55–57] Other substitutions were attempted to expand the arsenal of phenoxy-AlPcs, but were not successful, including pentafluorophenoxy-AlPc , 4-nitrophenoxy-AlPc and benzoate-AlPc.

The resulting phenoxy-AlPcs structures were confirmed by mass spectrometry and Nuclear Magnetic Resonance spectroscopy (H^1-NMR) in DMSO-d_6 (**Figures 3.7-3.11, Supporting Information**). The protons closest to the oxygen on the phenoxy groups experienced a significant upfield shift (drop in ppm) in H^1-NMR signal upon coupling of

the oxygen to the aluminum metal centre of the Pc (**Figures 3.7-3.11, Supporting Information**). Similar shifts have previously been reported for protons near oxygen in axially substituted silicon and tin Pcs.[18,58] Prior to device integration all materials were purified by train sublimation. The sublimation temperatures of all phenoxy-AlPcs were approximately 350 °C, which is significantly lower than the typical sublimation temperature for Cl-AlPc at 410 °C, suggesting weaker intermolecular interactions that enable lower sublimation temperatures. The R-AlPc molecules were characterized by both solution and solid-state UV-Vis (**Figure 3.12, Supporting Information**). Characteristic peaks at 677-683 nm corresponded to the Q-band of the Pcs, with the largest redshift observed for 345F-AlPc and largest blue shift for oCr-AlPc and pCr-AlPc. In all cases, we observed a broadening and red shifting of the absorption out to 770 nm for the solid-state samples, which are typical of solid-state interactions. Minimal changes in optical band gap due to phenoxylation is consistent with previously synthesized phenoxylated R-BsubPcs[26,53,54], R_2-SiPcs[38]and R-AlPcs.[55] The R-AlPc molecules exhibited limited solubility in most solvents, which is common for Pcs, limiting single crystal growth from solution. Sublimation also did not lead to single crystal formation. Regardless, we found that phenoxylation was an effective way to tune the molecular properties of R-AlPc.

3.5.2 R-AlPc Based Organic Thin-Film Transistors

R-AlPc compounds were incorporated into bottom-gate bottom-contact (BGBC) OTFTs as the semiconducting layer and compared to baseline Cl-AlPc after testing in air. Device output and transfer curves were obtained and used to extract the transconductance (g_m), saturation hole mobility (μ_h), on-off current ratio ($I_{On/Off}$), threshold voltage (V_T) and hysteresis (H). All transfer and output curves can be found in the Supporting Information (**Figure 3.13-3.14**). As demonstrated in **Figure 3.2**, Cl-AlPc maintained the highest performance among all R-AlPc compounds when integrated into OTFTs, with the greatest μ_h, g_m, and I_{On}. However, pCr-AlPc, mCr-AlPc and 345F_3-AlPc showed a comparable μ_h within the same order of magnitude as Cl-AlPc, and comparable if not superior V_T and $I_{On/Off}$. Additionally, the cresol-substituted compounds (pCr-AlPc, mCr-AlPc, oCr-AlPc) also experienced the lowest H of all R-AlPc.

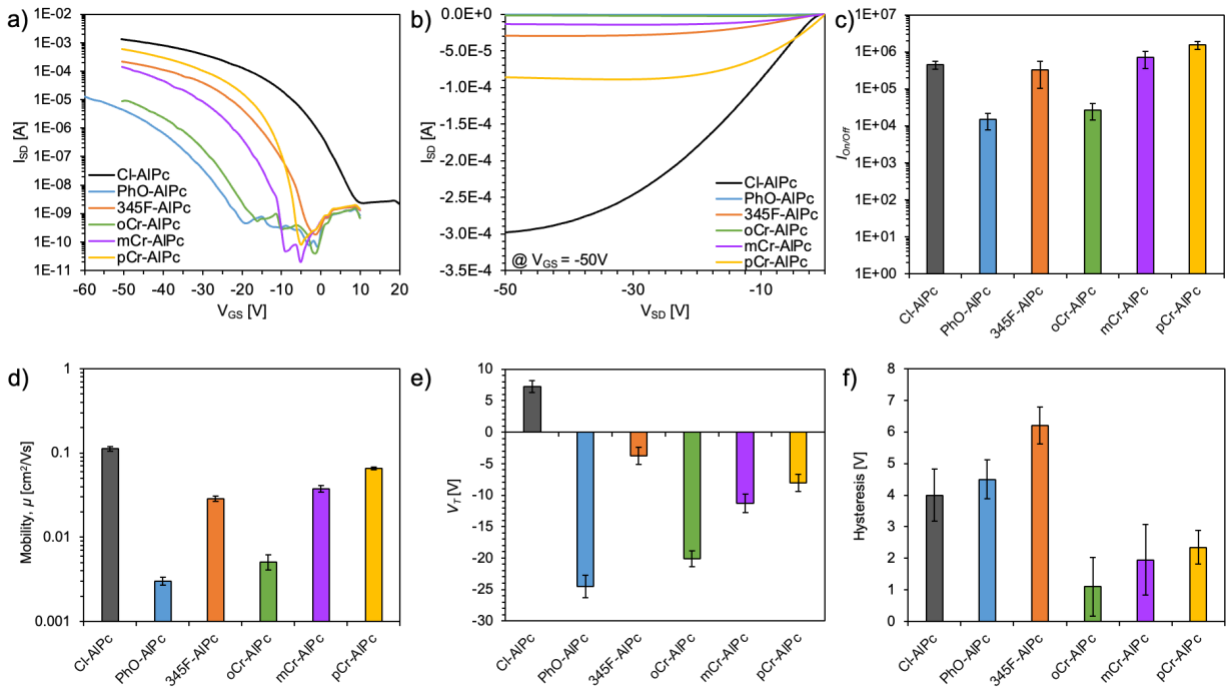

Figure 3.2. *Baseline performance of R-AlPc OTFTs, including the (a) transfer curves with a V_{SD} of -50 V and (b) output curves of a representative device at a V_{GS} of -50 V. The (c) $I_{On/Off}$, (d) μ_h, (e) V_T, and (f) H were determined from the average of a minimum of 10 devices.*

MPcs are known to crystallize in thin films such that small molecular changes, like the location of a methyl group on the axial phenoxy ring, can lead to widely different film morphologies and resulting OTFT performance.[59] In this study, the lowest-performing materials in devices were PhO-AlPc and oCr-AlPc, which both yielded a μ_h an order of magnitude lower than Cl-AlPc and a large V_T. A possible explanation for the poor performance of these substituted compounds lies in the molecular packing of these materials in thin-films, which has an effect on the surface morphology, and subsequent charge transfer through the film.[11,13] Towards this end, the surface morphology of each R-AlPc film was investigated by AFM (**Figure 3.3**). The thin-films of 345F$_3$-AlPc, mCr-AlPc and pCr-AlPc all had similar morphologies, with highly crystalline domains and a similar mean surface roughness of 3-4 nm. Additionally, the shape and size of the grains are similar to those of the Cl-AlPc film, forming larger, more plate-like grains consistent with those previously reported for Cl-AlPc.[60] However, the PhO-AlPc film shows substantially smaller crystal domains, while the oCr-AlPc film shows much larger, irregularly shaped crystal structures compared to Cl-AlPc. Both PhO-AlPc and oCr-AlPc film morphologies could account for the reduced charge transport efficiency observed

from OTFTs derived from these semiconductors (**Figure 3.2**). The smaller crystal domains in the PhO-AlPc film have a smaller area of tightly packed and aligned molecules with more grain boundaries throughout the film, which would have a higher impact on the resistance to charge transport.[61,62] The highly disordered grains observed in the oCr-AlPc film are randomly oriented and have larger grain boundaries, which would also negatively impact charge transport. As demonstrated by the Cl-AlPc, 345F-AlPc, pCr-AlPc and mCr-AlPc films, highly crystalline domains of a moderate size strike a good balance, with high quality transport pathways available with fewer large grain boundaries.

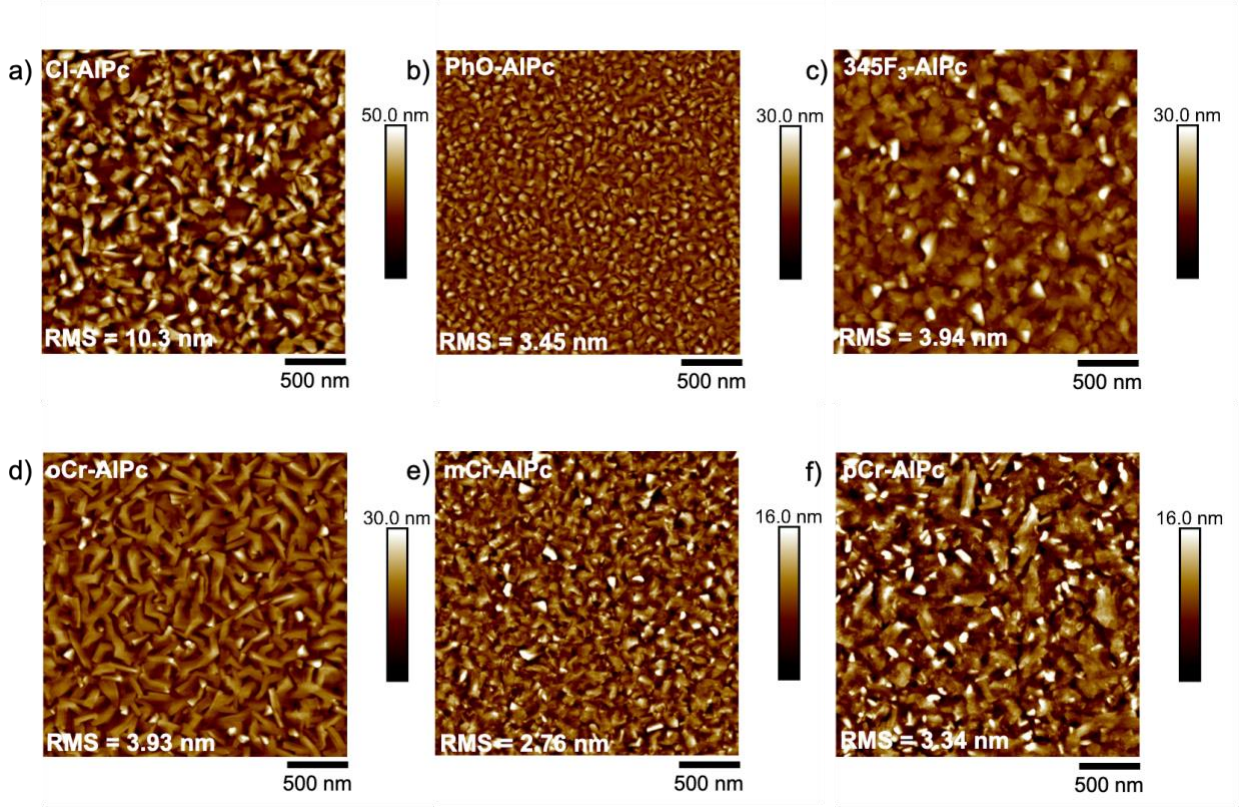

Figure 3.3. *AFM images of Cl-AlPc (a), PhO-AlPc (b), 345F$_3$-AlPc (c), oCr-AlPc (d), mCr-AlPc (e), and pCr-AlPc (f). All images are 2.5 μm x 2.5 μm, with a scale bar of 500 nm.*

To further compare the crystallinity and orientation of the films, GIWAXS was performed on each of the films (**Figure 3.15, Supporting Information**), however since single crystal data could not be obtained for each of the R-AlPc compounds, the resulting scattering could not be attributed to the specific packing of the molecules. From **Figure 3.15**, the highest performing devices appeared to have the broadest scattering signals and distribution of molecular orientations (**Figure 3.28, Supporting Information**). These

films still demonstrate a high overall crystallinity by XRD (**Figure 3.19, Supporting Information**) and AFM (**Figure 3.3**) but are likely less uniformly aligned. However, their favorable grain structures and high crystallinity within those individual grains is likely driving the higher performance of these films. The scattering pattern observed for oCr-AlPc was sharp with many high intensity reflections, indicating highly ordered crystalline domains with a strong preferential orientation to the substrate at a χ of 75° (**Figure 3.28**), although the exact orientation of the Pc cannot be concluded due to the lack of single-crystal XRD data. While the crystallinity of this film was high with a single preferential orientation, which is generally associated with improved device performance, this orientation could be less conducive to efficient charge transport in conjunction with the larger grain boundaries and irregular grain structures observed by AFM. Overall, the performance of phenoxy-AlPc derivatives in OTFTs, paired with their film characterization, demonstrates that they can successfully act as semiconductors, and that phenoxylation can be used both to impart functionality to the Pc and provide a handle for crystal engineering and device optimization through molecular design.

3.5.3 Exposure of R-AlPc Molecules to Cannabinoids

To assess the performance of the R-AlPc materials as a cannabinoid sensing layer, they were integrated into OTFT-based sensors. The R-AlPc OTFTs were characterized before and after exposure to 300 ppm THC vapor, 300 ppm CBD vapor (**Figure 3.4, 3.16**), 20 μM THC solution and 20 μM CBD solution (**Figure 3.17, Supporting Information**) to determine how the device performance changed in response to cannabinoid exposure. A similar sensor response, in terms of trends, between the R-AlPcs and THC and CBD solution and vapor was observed, thus for simplicity this section will focus on the discussion of THC and CBD vapor. Overall, compared to Cl-AlPc, devices made with 345F-AlPc, mCr-AlPc and pCr-AlPc experienced a greater change in μ_h, g_m and $I_{On/Off}$, while devices made with all phenoxy-AlPcs experienced larger shifts in V_T compared to Cl-AlPc (**Figure 3.4**). The performance of these materials surpasses those previously reported using Cl-AlPc[12], but does not quite reach the sensitivity achieved using ZnPc as the sensing layer.[13] Other previously reported MPc cannabinoid

sensors have reached similar sensitivities, but have required the addition of a sensitizing probe to the surface to achieve these results.[9–11]

Additionally, some phenoxy-AlPcs experienced selective responses to one cannabinoid over the other. However, the reason for this response is ultimately unknown. A selective response to THC and CBD has previously been reported for Cl-AlPc and other MPcs in OTFTs,[9–12] and their interactions in solution have been investigated, suggesting strong coordination between the nitrogen ring and central metal of the Pc with the conjugated ring of the cannabinoids, causing changes in their electrical properties.[10] It is unclear if these interactions in solution are reproduced in a thin-film. The selectivity observed with the phenoxy-AlPcs could be due to a combination of similar electrochemical interactions and the interactions of THC and CBD with the different crystal structures and morphologies of the phenoxy-AlPcs. The absence of single crystal data for each of the phenoxy-AlPcs makes it difficult to draw conclusions, but these results indicate that the choice of phenoxy group on the AlPc could be used to provide a more sensitive cannabinoid sensing layer in OTFT based sensors.

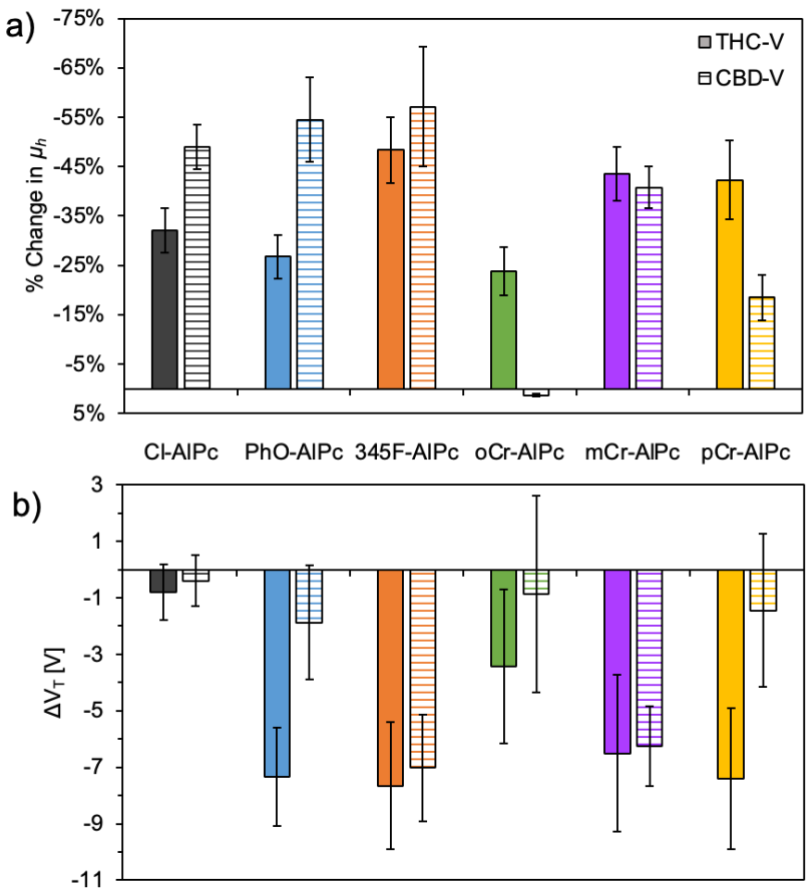

Figure 3.4. *OTFT Performance before and after exposure to 300 ppm THC vapor and 300 ppm CBD vapor for 90 seconds. The change in (a) μ_h and (b) V_T, were determined from the average of a minimum of 10 devices, where the x-axis legend is the same for both (a) and (b).*

As previously observed, THC and CBD can coordinate strongly with R-AlPc molecules, changing the Pcs electronic properties, and therefore the substituted phenoxy group could improve these interactions.[10] Additionally, THC and CBD can induce structural changes in thin films, also leading to reductions in μ_h, $I_{On/Off}$, V_T, and changes in subthreshold slope and defect density.[11–13] **Figure 3.5** presents the AFM, GIWAXS and OTFT transfer curves for 345F-AlPc and Cl-AlPc before and after exposure to THC or CBD vapor to investigate the effect of phenoxy functionalization of AlPc. The AFM images show significant reorganization or recrystallization takes place with exposure to THC or CBD, leading to larger crystals with greater grain boundaries and an increase in surface roughness from 3.9 to 14.8 nm and 18.9 nm, respectively, for the 345F-AlPc films. In comparison, the same exposure led to a reduction in grain size for Cl-AlPc films and a drop in surface roughness from 10.3 to 5.6 nm and 9.06 nm for THC and CBD,

respectively (**Figure 3.5**). Changes in grain size and film morphology order affect the number and quality of charge transport pathways available, altering the defect density and causing a reduction in performance as a result of structural interactions of THC or CBD with thin films of Pcs.[11] An increase in grain size, as seen with 345F-AlPc, can lead to a decrease in defect density due to the larger crystal structures (**Figure 3.16, Supporting Information**), but a simultaneous decrease in the quality of charge transport pathways due to the larger grain boundaries and more irregular grains, leading to the observed overall reduction in μ_h and V_T.[38,61,63] A similar trend was observed with the other phenoxy-AlPc films (**Figure 3.20, 3.21, Supporting Information**). The orientation of the molecules within these grains may also help explain the reduced performance.

The 2D scattering patterns and the azimuthally-integrated GIWAXS patterns of Cl-AlPc thin-films displayed in **Figure 3.5** exhibit no large structural changes after THC or CBD exposure. However, exposure to THC and CBD vapor resulted in a change in molecular order of the Cl-AlPc film with a slight increase in film crystallinity evident by the rounded reflection at q = 0.56 Å^{-1}, compared to the more arched shaped of the same reflection pre-exposure to cannabinoids. These results are consistent with previous reports for Cl-AlPc films upon exposure to THC and CBD (liquid solution or vapor).[12] Conversely, 345F-AlPc films experience significant microstructural changes while maintaining approximately the same degree of molecular order and crystallinity. The initial thin films display high intensity reflections at q = 0.61 Å^{-1} and q = 0.65 Å^{-1} along the q_z axis. When exposed to THC or CBD, a change in the ratio of these two peaks suggests a reorganization in the thin-film. A change in the average molecular orientation was also detected from primarily ~52° to a more mixed orientation with ~25°, determined by linecuts with respect to χ (**Figure 3.5**). This means there could be a mix of molecules oriented more face-on than edge-on to the substrate upon exposure to cannabinoids, which is associated with reduced mobility and lower I_{On}.[13,38] This can help explain the observed reduced mobility with the larger crystallite size seen by AFM, which is generally associated with improved mobility. Similar relative changes in peak intensities from the (100) plane at q = ~0.50 Å^{-1} and (10-2) plane at q = 0.68 Å^{-1} of β-ZnPc films have been reported after exposure to THC vapor in conjunction with a shift in the average molecular orientation from ~45° to ~74° for β-ZnPc molecules relative to the substrate.[13] The more

face-on oriented films had a lower $I_{On/Off}$, and lower μ_h.[13] While no single crystal data is available for the phenoxy-AlPc derivatives, a similar shift in 345F-AlPc molecular orientation is likely taking place with exposure to THC and CBD due to the similar changes detected by GIWAXS. In fact, all other phenoxy-AlPc films experienced similar shifts in their film morphology (**Figure 3.18, 3.20-3.22, Supporting Information**), with pronounced grain restructuring and crystal reorganization similar to that of 345F-AlPc. The integrated GIWAXS patterns demonstrate that the phenoxy substitutions promote more reorganization of R-AlPc films upon THC vapor exposure that is not observed with Cl-AlPc. By GIWAXS (**Figure 3.15**) and XRD (**Figure 3.19**), the *d*-spacing of the phenoxylated-AlPc films is smaller than Cl-AlPc, suggesting smaller intermolecular distances. However, as evidenced by lower sublimation temperature, the phenoxy groups are likely disrupting the strength of the inter-molecular interactions, corroborating the higher tendency for the phenoxy-AlPc films to reorganize upon exposure to cannabinoids.

The R-AlPc films were also exposed to a 20 μM liquid THC solution, and 20 μM CBD solution, where similar results were observed (**Figure 3.23-3.28, Supporting Information**). Significant changes in the thin-film morphology were observed for the phenoxy-AlPc films, resulting in the larger changes observed in their device performance. Again, 345F-AlPc experienced significant surface morphology changes in response to THC and CBD vapor resulting in an increase in grain size and surface roughness. This surface reorganization was less significant upon exposure to THC and CBD solutions, suggesting the solvent interferes with the surface interactions. These results demonstrate selective effects of THC relative to CBD which can facilitate ratiometric cannabinoid analysis[9], and the improvement of OTFT sensitivity to both cannabinoids with the implementation of phenoxylated AlPc.

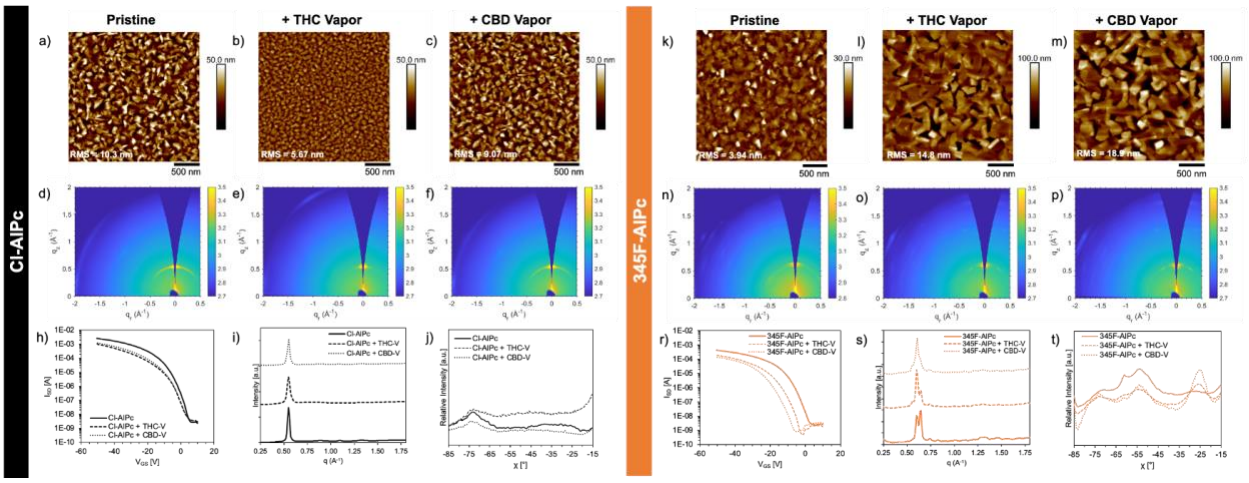

Figure 3.5. *Film morphology and device performance of Cl-AlPc (a-j) and 345F-AlPc (k-t) films in response to 300 ppm THC vapor or CBD vapor. Figures (a-c) and (k-m) are 2.5 μm x 2.5 μm AFM images. Figures (d-f) and (n-p) are 2D GIWAXS spectra while (i) and (s) are the corresponding diffraction patterns, and (j) and (t) are the linecut profiles with respect to χ for a q range of 0.5-0.65. Figure h) and r) are the OTFT transfer curves.*

Finally, Raman spectroscopy was used to further probe the interactions between the R-AlPc molecules and cannabinoids in a thin film (Figure S24). Upon exposure, there appears to be shifting of the peaks in both location and intensity around the isoindole region of the spectra, at ~1530-1540 cm^{-1}.[64,65] Spectra of THC and CBD alone were collected to confirm that these shifts were not caused merely by the presence of the cannabinoids (Figure S25). These results indicate a change in the environment around the R-AlPc molecules in a thin film, possibly suggesting the interactions observed previously in solution with MPcs[10] are maintained in a thin film. Further investigation is required to characterize the nature of the interaction taking place.

Phenoxylation of R-AlPc alters the crystal packing of R-AlPc molecules, reducing the strength of the intermolecular interactions compared to Cl-AlPc. As THC has been shown to coordinate with the nitrogen ring of AlPcs in previous work,[10] the tight crystal structure is likely interrupted by the introduction of THC, causing more drastic shifts in its film structure. Consequently, the addition of the phenoxy groups changed the response of AlPc to analytes and generated a more sensitive cannabinoid sensor through the introduction of new crystal structures. This demonstrates the utility of molecular engineering as a strategy to fine tune the thin-film properties of Pcs for sensor optimization through the enhancement of Pc-analyte interactions.

3.6 Conclusion

This work demonstrates the successful synthesis and integration of phenoxylated AlPc molecules in OTFT cannabinoid sensors for the first time. Through the introduction of new crystal structures and intermolecular interactions, the phenoxy-AlPc molecules have shown an improved response to THC compared to Cl-AlPc, while maintaining a comparable baseline device performance. The most sensitive of the substitutions, 345F-AlPc, experienced drastic changes in grain size and film roughness, thin-film reorganization and crystal orientation upon exposure to THC vapor that were not detected with Cl-AlPc. These structural changes within the thin film drive the improved sensitivity to THC and highlight molecular engineering as a straightforward technique to tune and enhance analyte-semiconductor interactions in OTFT sensors.

3.7 Experimental Section

3.7.1 Materials

Cl-AlPc (85% purity) was received from Abacipharm and used in chemical reactions as received. It was purified by train sublimation before use in OTFTs. Phenol, o-cresol, p-cresol, and 3,4,5-trifluorophenol were supplied by TCI Chemicals, and m-cresol was supplied by Sigma-Aldrich. All were used as received. (Octyl)trichlorosilane (OTS, 97%) was purchased from TCI Chemicals and used as received. Chlorobenzene (99%) was purchased from Sigma-Aldrich. DMSO-d_6 was supplied by Cambridge Isotope Laboratories Ltd. All other solvents used in device fabrication were HPLC grade and purchased from Fisher Scientific. Toronto Research Chemicals supplied the cannabinoid standards.

3.7.2 Chemical Characterization

NMR spectroscopy of all newly synthesized compounds was performed on a Bruker AVANCE III 400 NMR spectrometer. Mass spectrometry analysis was performed at the University of Toronto AIMS Mass Spectrometry Laboratory.

3.7.3 Chemical Synthesis

A 100 mL round-bottom flask was charged with 1 g of Cl-AlPc (1.74 mmol) and a 10-molar excess of the substituted phenol in 30 mL of chlorobenzene. The flask was stirred under nitrogen and refluxed at 125 °C for 18 hours. Upon cooling, the solvent was evaporated and the solid was washed with 3M KOH, filtered, and dried. The product was purified by train sublimation at 350 – 380 °C, depending on the compound, to obtain a pure final product for use in device fabrication. The structure of all synthesized compounds was confirmed by NMR spectroscopy **(Figures S3.2-S3.6**) and mass spectrometry (**Figures S3.26-S3.30**). The details and results for each individual reaction can be found in the Supporting Information **(Table S3.1**).

3.7.4 Thin-Film Deposition

Fraunhofer IPMS supplied prefabricated devices to make BGBC transistors, each consisting of a 230 nm thermally grown SiO_2 dielectric layer on an Si gate, and prepatterned source-drain electrodes with a *W/L* of 1000 (*W* = 10 mm, *L* = 10 μm). Substrates purchased from Ossila were used for AFM and XRD characterization, consisting of a 300 nm thermally grown SiO_2 dielectric layer on Si. The substrates were completely rinsed with acetone to remove the photoresist, then washed with isopropanol and dried under a N_2 gas stream. The substrates were treated with air plasma for 15 minutes then briefly rinsed with water, isopropanol, and dried with N_2. Once dry, they were immersed in a 1% v/v OTS solution in toluene for 1 hour at 70 °C. The substrates were then rinsed with toluene and isopropanol, dried with N_2, and placed in a vacuum oven at 70 °C for 1 hour to remove trace solvent. The substrates were placed in an Angstrom EvoVac thermal evaporator at a pressure below 2 x 10^{-6} Torr and heated to 140 °C, and the temperature was stabilized and held for 1 hour. Deposition of R-AlPc was performed by sublimation at 0.2 Å s^{-1} until a thickness of 500 Å was reached. The substrates were cooled to room temperature before physical and electrical characterization.

3.7.5 AFM Characterization

AFM measurements (2.5 μm x 2.5 μm) were performed with a Bruker Dimension Icon AFM with ScanAsyst-Air tips and a scan rate of 0.69 Hz. Processing of images were performed using NanoScope Analysis v.1.8 software.

3.7.6 XRD Characterization

XRD measurements were performed using a Rigaku Ultima IV powder diffractometer with a Cu-Kα (λ = 1.5418 Å) source with a scan range of $3° < 2\theta < 18°$ at a rate of $0.5° \text{ min}^{-1}$.

3.7.7 GIWAXS Characterization

GIWAXS experiments were performed at the Canadian Light Source (CLS) in Saskatoon, Canada on the Brockhouse Diffraction Sector Undulator (BXDS IVU) beamline with a photon energy of 10 keV. The scattering data was collected on a Rayonix MX300 CCD detector (73.242 μm x 73.242 μm pixel size), placed 401.5 mm from the sample, at an angle of $\theta = 0.3°$. All data was calibrated with silver behenate and poly(3-hexylthiophene-2,5-diyl) standards and analyzed with the GIXSGUI software package in MATLAB, where both polarization and solid-angle corrections were applied.

3.7.8 Raman Characterization

Raman spectra were collected on a Renishaw inVia Raman microscope using a 532 nm laser with 2400 l/mm grating. The spectra for the R-AlPc films were collected as a sum of 5 accumulations at 10% power, with 1-second exposure per measurement over a wavelength range of 550-1700 cm^{-1}. The THC and CBD-only spectra was performed on a thin film of pure cannabinoid oil on a glass slide, and were collected as a sum of 5 accumulations at 10% power with 5-second exposure per measurement over a wavelength range of 550-1700 cm^{-1}. A baseline subtraction was performed to remove the baseline noise from the measurement.

3.7.9 OTFT Characterization

Transistors were tested using a custom-build auto tester machine and run using a Keithley 2614B SourceMeter and Labview software. The V_{SD} and V_{GS} were set and the I_{SD} was measured to obtain both output and transfer curves. Six transfer curves were taken for each transistor and the final three were averaged. From the transfer curve, the V_T, H and μ_h could be extracted, the latter using **Equation 3.1**.

$$I_{SD} = \frac{\mu C_i W}{2L}(V_{GS} - V_T)^2 \quad (3.1)$$

Once the baseline performance of all R-AlPc compounds was assessed, new transistors were exposed to either a liquid THC solution (20 μM) in hexanes, a liquid CBD solution (20 μM) in hexanes, THC vapor (300 ppm concentration) or CBD vapor (300 ppm concentration). For the liquid solutions, 0.5 μL was dropcast on the transistor surface and allowed to dry for 2 minutes. For vapor exposure, the samples were vaporized into an 8 L bag using the Vapormed Volcano Medic, and the bag was slowly emptied over the devices in a chamber for 90 seconds. New output and transfer curves were then obtained for all exposed devices, allowing for a comparison with the baseline values to assess the sensitivity of each R-AlPc compound as a sensing layer for OTFT cannabinoid sensors.

3.8 Acknowledgments

This work was supported by NSERC Discovery grant RGPIN 2015-05796 (A.J.S.), 2015-05453 (C.S.H.), and 2020-04079 (B.H.L.), the Canada Research Chairs Program 950-230754 (A.J.S.) and 950-230724 (B.H.L.). Student support was acquired through NSERC PGS-D (H.L). The authors would like to thank the CLS for providing beamtime, which was supported by CFI, NSERC, the National Research Council (NRC), the Canadian Institutes of Health Research (CIHR), the Government of Saskatchewan, and the University of Saskatchewan. The Centre for Research in Photonics at the University of Ottawa (CRPuO) is acknowledged for providing access to the AFM.

3.9 Supporting Information

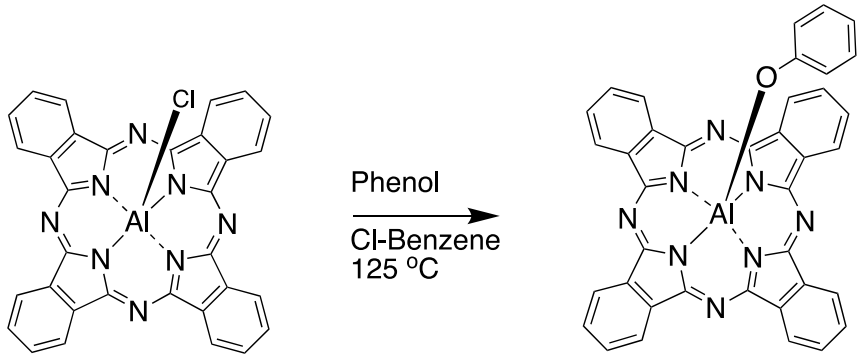

Figure 3.6. *Phenoxylation reaction of Cl-AlPc.*

Table 3.1. *Synthesis results for R-AlPc substituents.*

R-Group	Reaction Yield After Sublimation (%)	Expected Mass (g/mol)	Confirmed Mass (g/mol)	Confirmed Structure by 1H-NMR
Phenol (2)	16	632.17	632.17	Yes
3,4,5-Trifluorophenol (3)	38	686.14	686.14	Yes
o-Cresol (4)	36	646.18	646.18	Yes
m-Cresol (5)	28	646.18	646.18	Yes
p-Cresol (6)	13	646.18	646.18	Yes

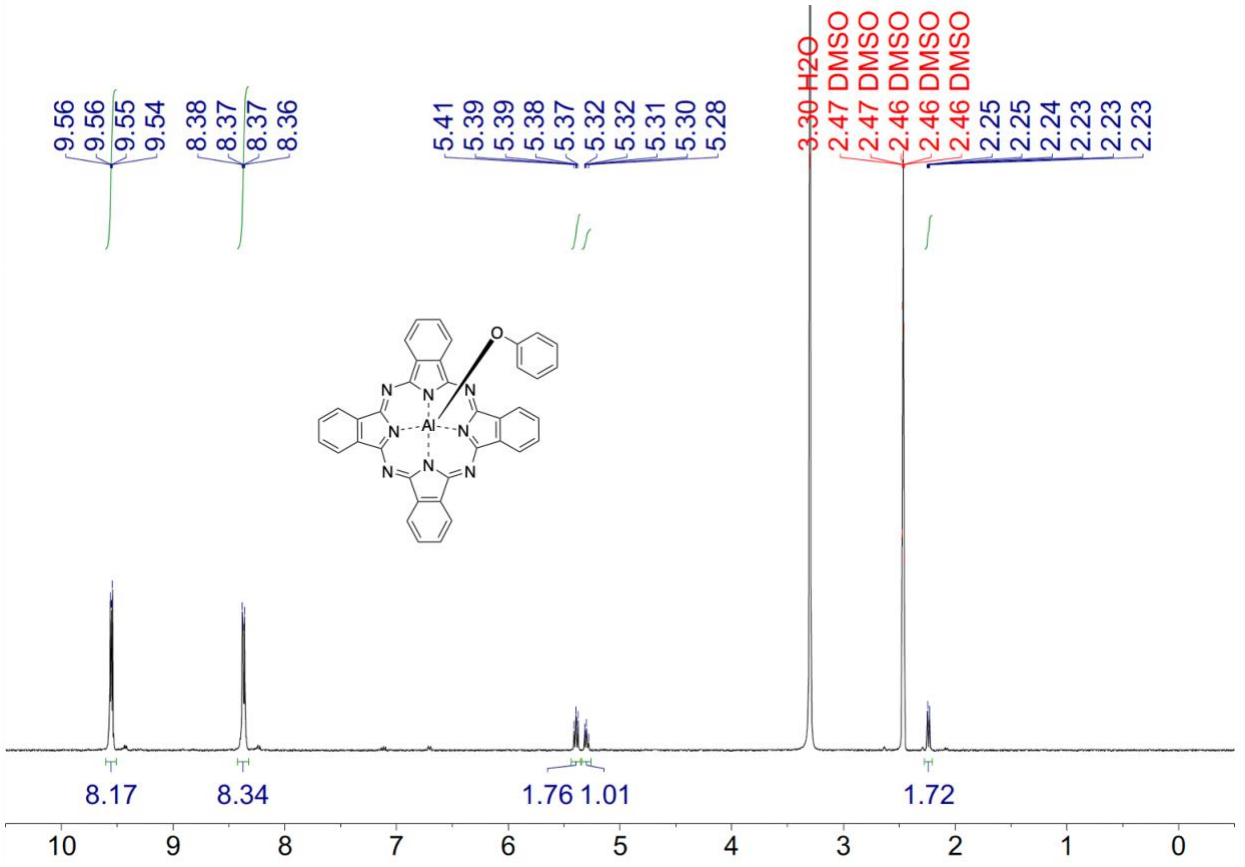

Figure 3.7. *1H-NMR of PhO-AlPc (2). (400 MHz; DMSO-d_6): δ 9.55 (m, 8H), 8.37 (m, 8H), 5.39 (m, 2H), 5.30 (m, 1H), 2.24 (m, 2H)*

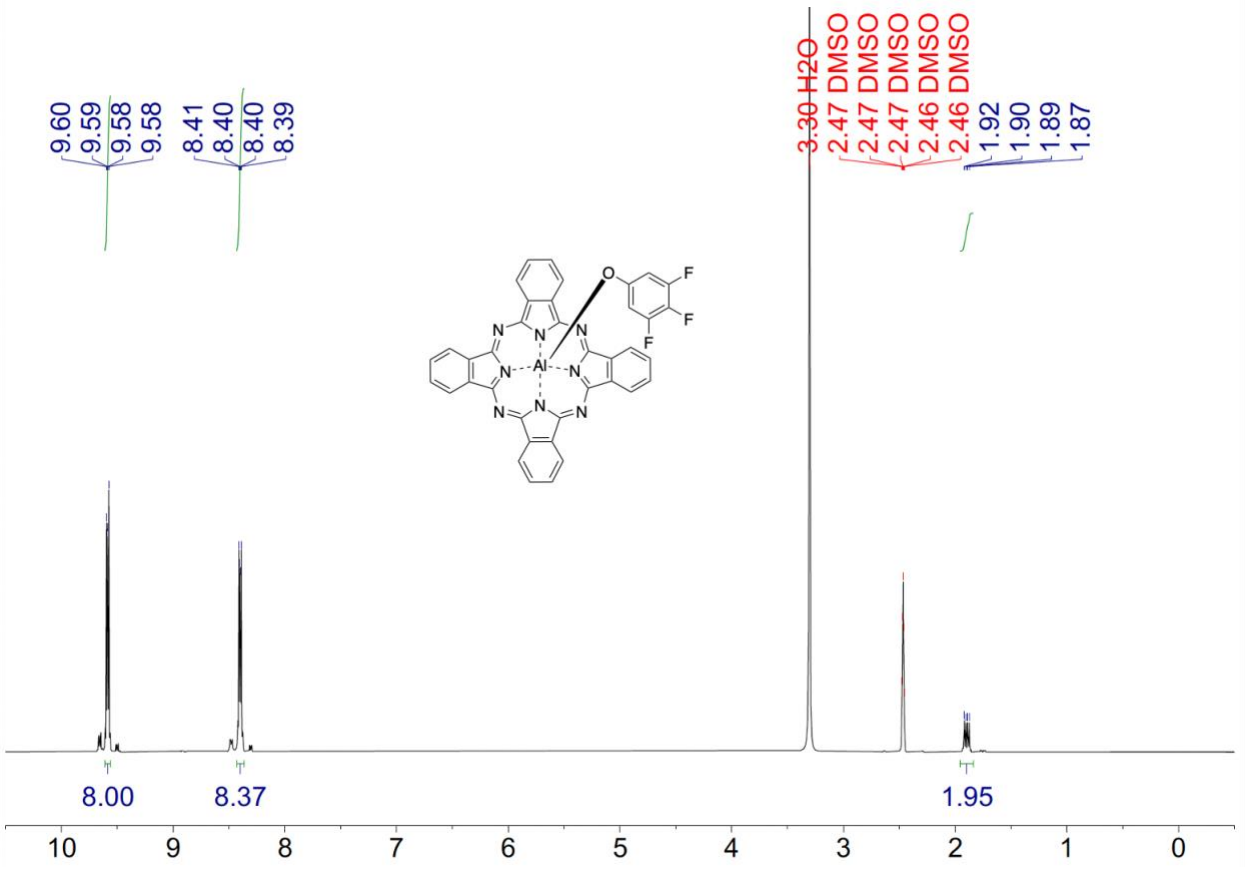

***Figure 3.8**. 1H-NMR of 345F$_3$-AlPc (3). (400 MHz; DMSO-d$_6$): δ 9.62 (m, 8H), 8.43 (m, 8H), 1.93 (m, 2H)*

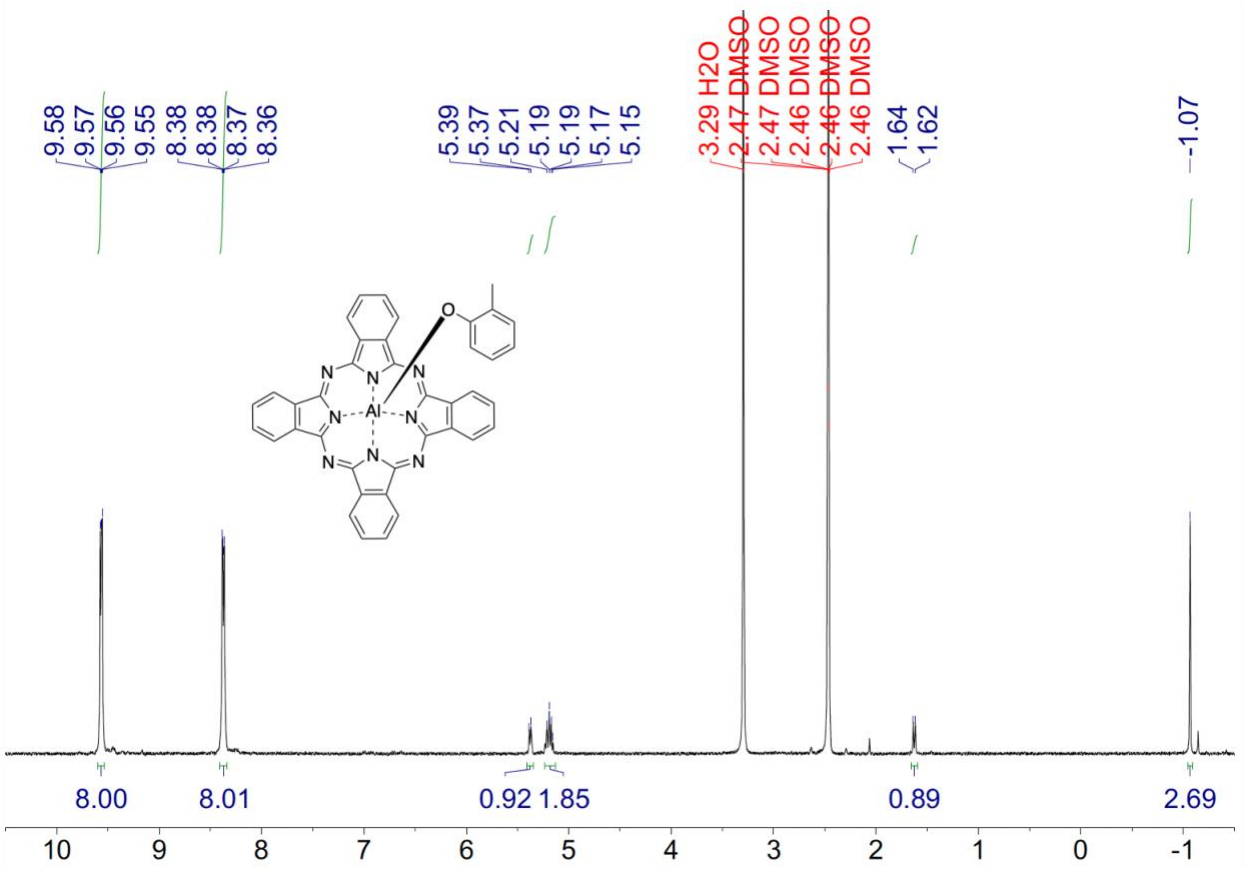

Figure 3.9. *1H-NMR of oCr-AlPc (4). (400 MHz; DMSO-d$_6$): δ 9.57 (m, 8H), 8.37 (m, 8H), 5.38 (m, 1H), 5.19 (m, 2H), 1.63 (d, J = 7.9 Hz, 1H), -1.07 (s, 3H).*

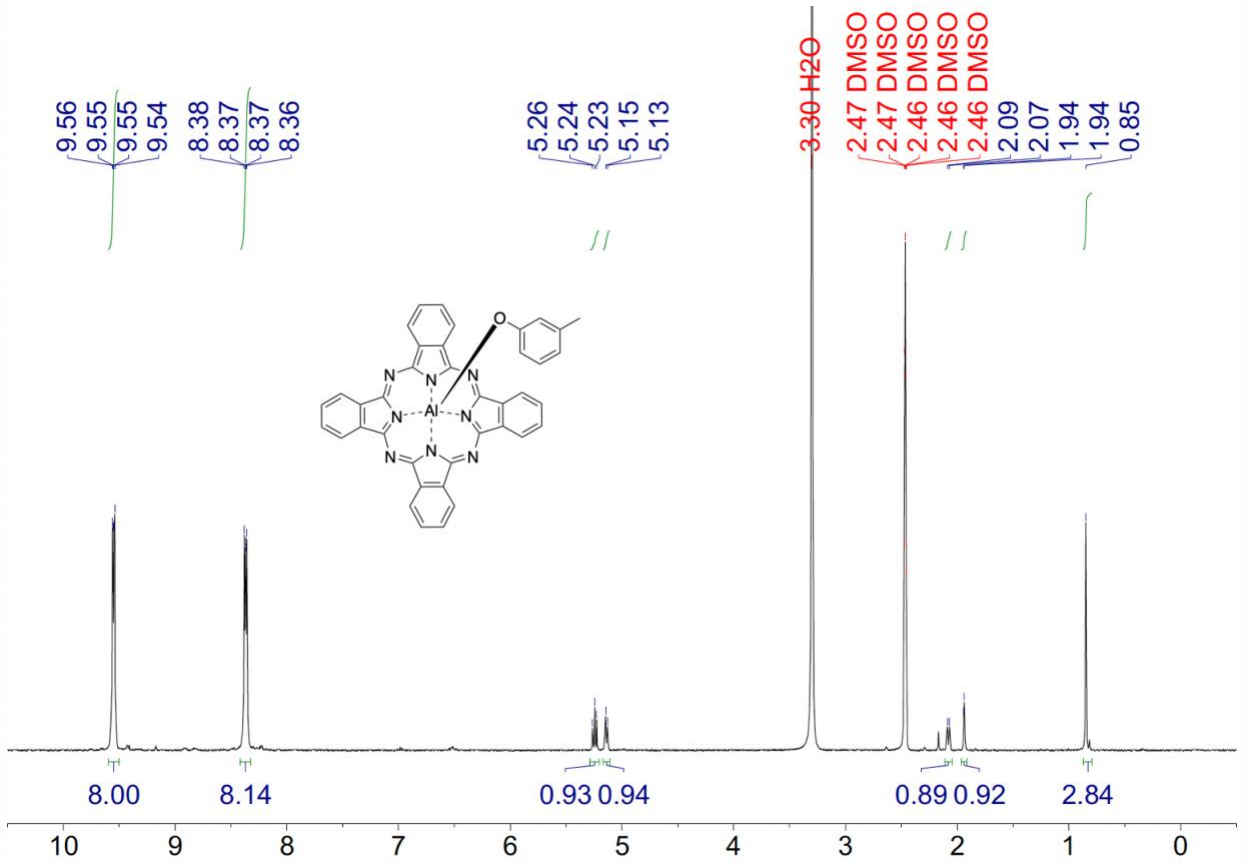

***Figure 3.10**. 1H-NMR of mCr-AlPc (5). (400 MHz; DMSO-d_6): δ 9.55 (m, 8H), 8.37 (m, 8H), 5.24 (t, J = 7.7 Hz, 1H), 5.14 (d, J = 7.3 Hz, 1H), 2.08 (d, J = 8.0 Hz, 1H), 1.94 (s, 1H), 0.85 (s, 3H).*

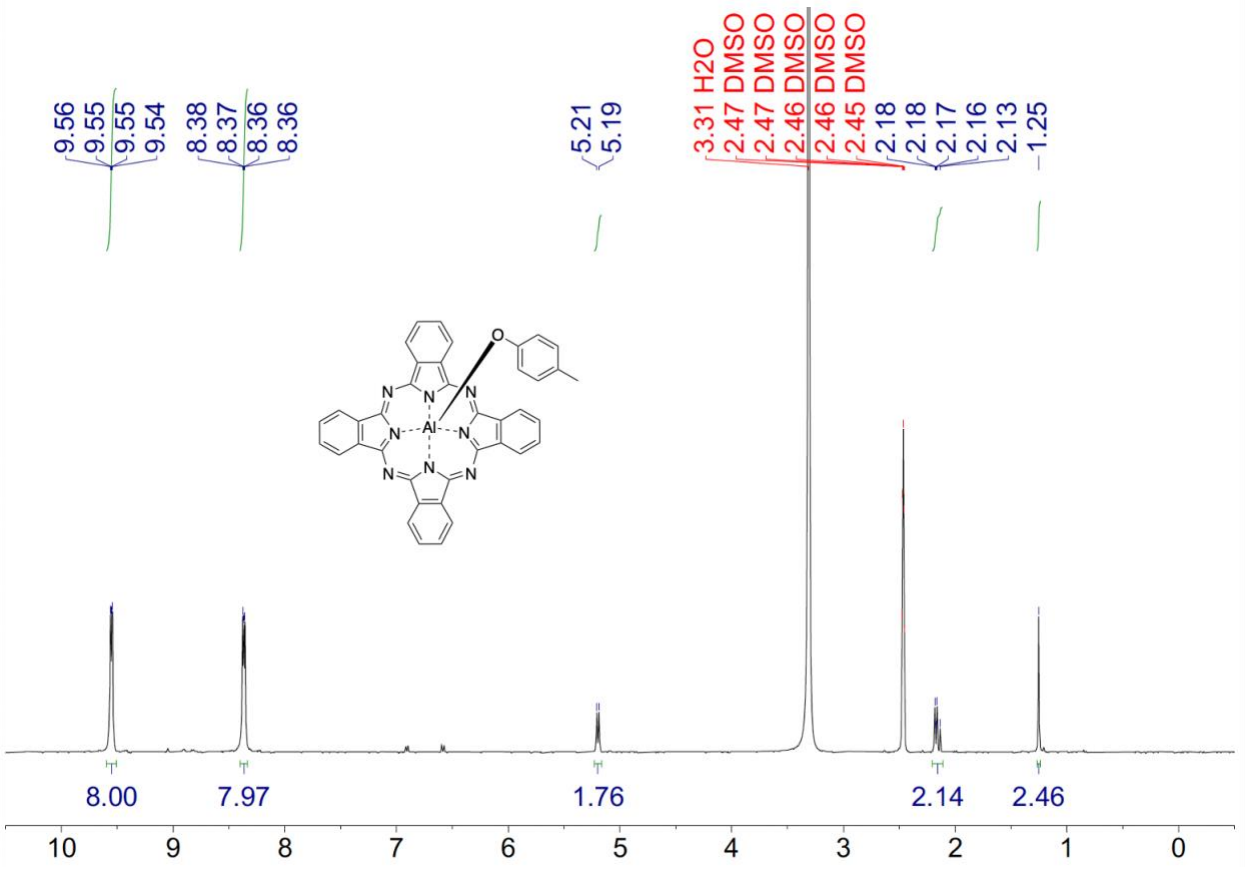

Figure 3.11. *1H-NMR of pCr-AlPc (6). (400 MHz; DMSO-d_6): δ 9.56 (m, 8H), 8.37 (m, 8H), 5.20 (d, J = 8.1 Hz, 2H), 2.16 (d, J = 7.3 Hz, 1H), 2.17 (m, 2H), 1.94 (s, 1H), 1.25 (s, 3H).*

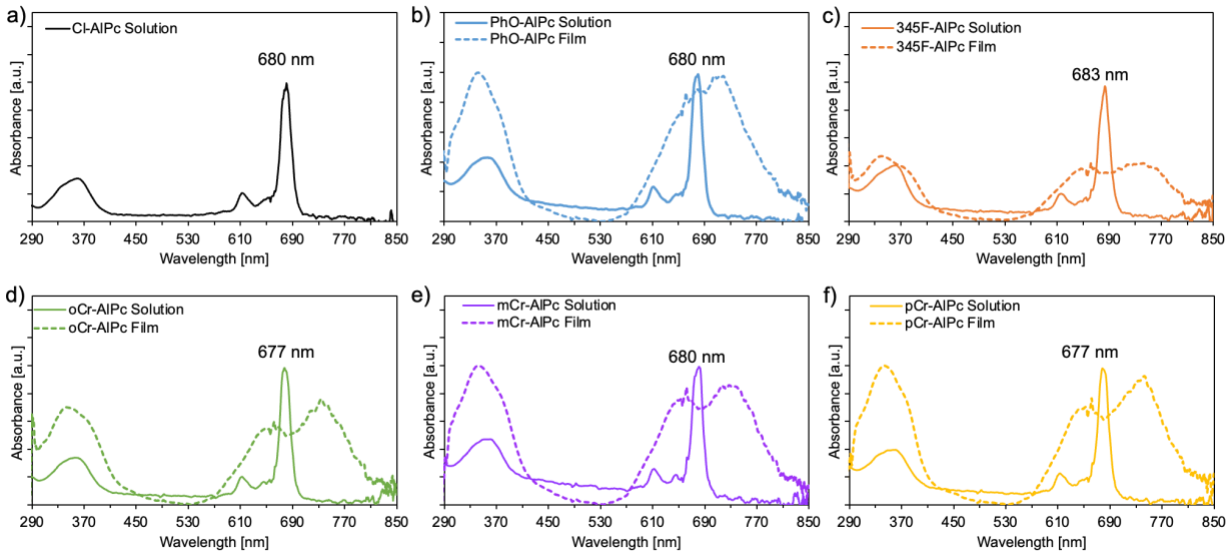

Figure 3.12. *UV-Vis of substituted aluminum phthalocyanine molecules, including (a) Cl-AlPc, (b) PhO-AlPc, (c) 345F-AlPc, (d) oCr-AlPc, (e) mCr-AlPc, and (f) pCr-AlPc. Solution samples are indicated by a solid line, and solid-state samples are indicated by a dashed line.*

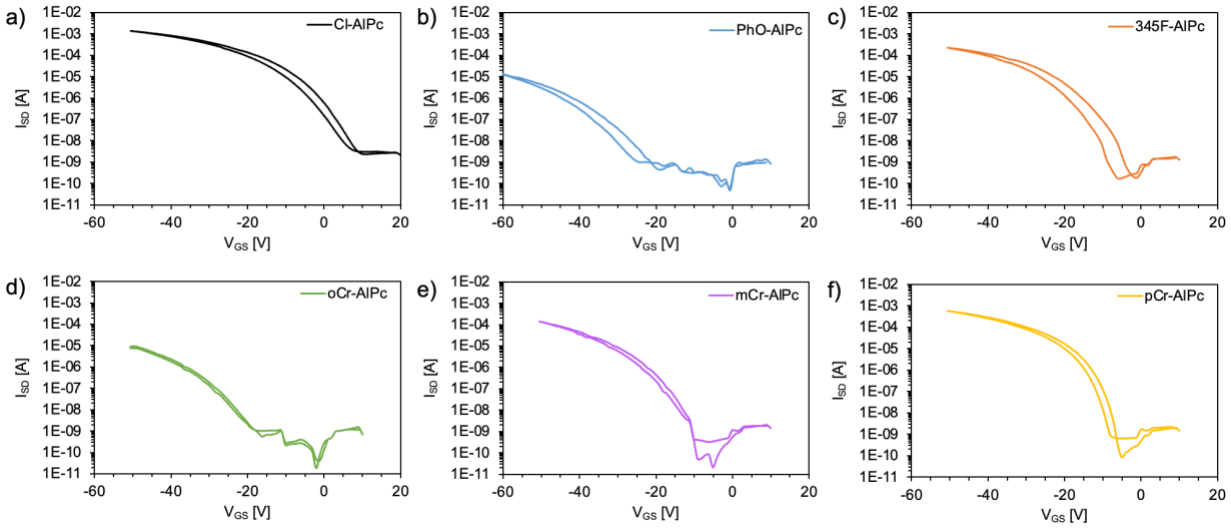

Figure 3.13. *Forward and reverse transfer curves of R-AlPc OTFTs, with a V_{SD} of -50 V, (a) Cl-AlPc, (b) PhO-AlPc, (c) 345F-AlPc, (d) oCr-AlPc, (e) mCr-AlPc, and (f) pCr-AlPc.*

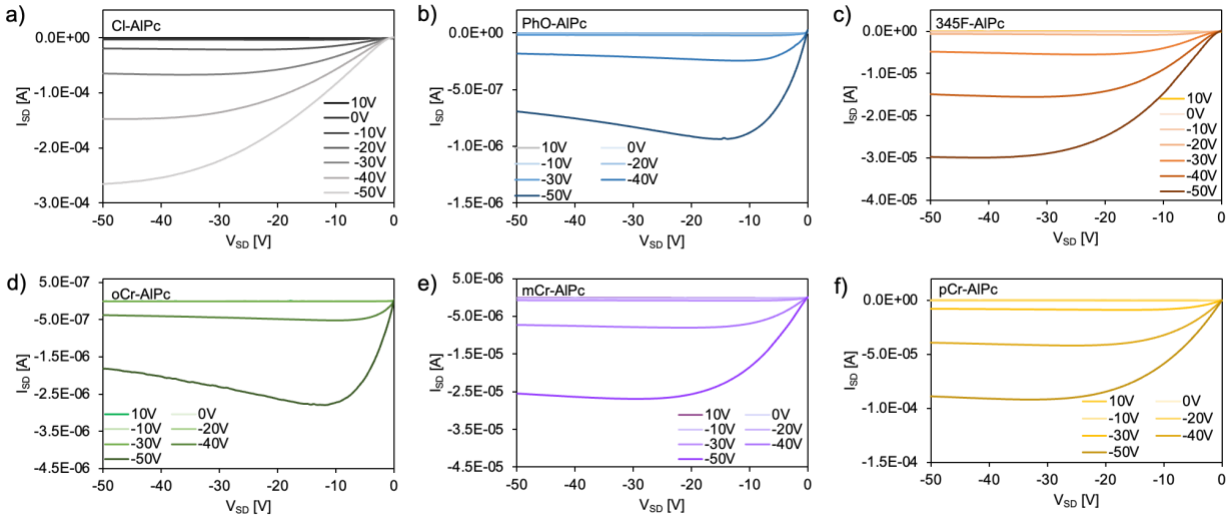

Figure 3.14. *Output curves R-AlPc OTFTs, (a) Cl-AlPc, (b) PhO-AlPc, (c) 345F-AlPc, (d) oCr-AlPc, (e) mCr-AlPc, and (f) pCr-AlPc.*

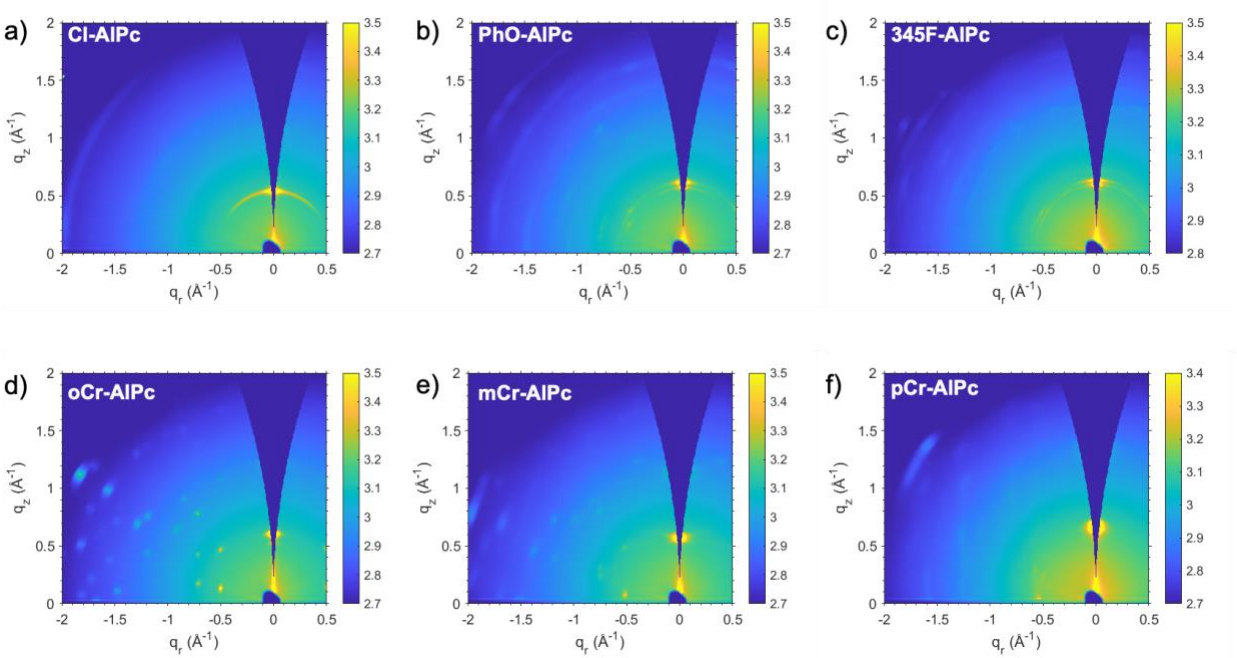

Figure 3.15. *2D GIWAXS spectra of (a) Cl-AlPc, (b) PhO-AlPc, (c) 345F-AlPc, (d) oCr-AlPc, (e) mCr-AlPc, and (f) pCr-AlPc films.*

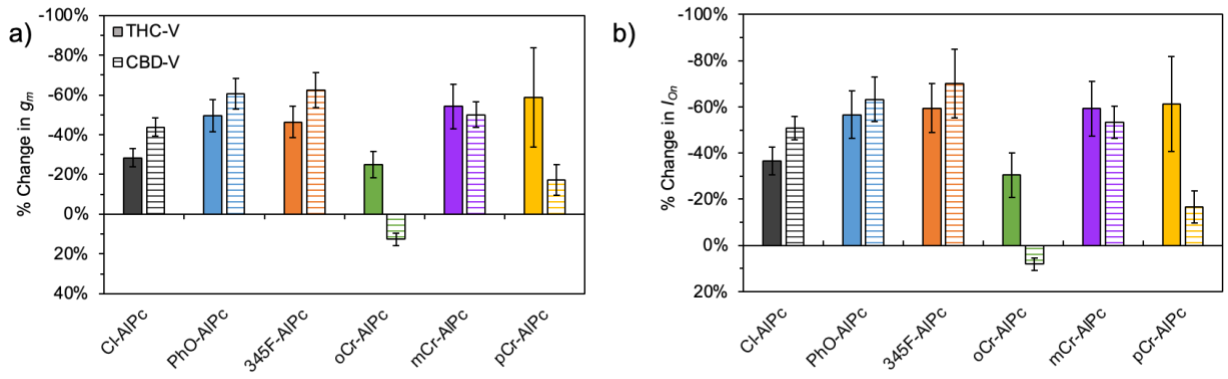

Figure 3.16. *OTFT performance before and after exposure to 300 ppm THC vapor (THC-V) or 300 ppm CBD vapor (CBD-V) for 90 seconds. The change in (a) g_m, and (b) I_{On} were determined from the average of a minimum of 10 devices.*

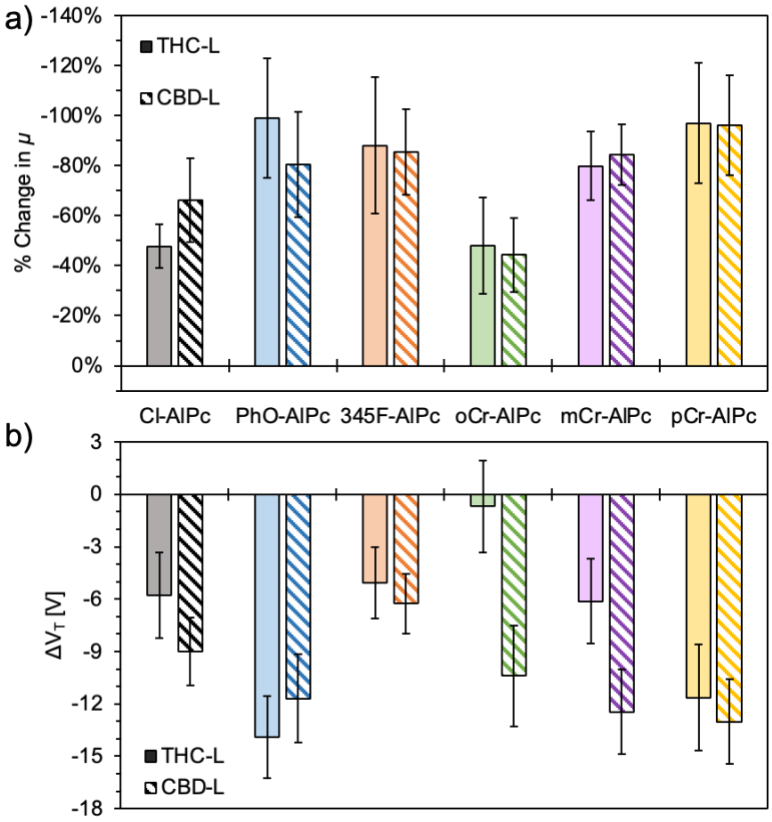

Figure 3.17. *OTFT performance before and after exposure to 20 μM THC (THC-L) or CBD (CBD-L) solution in hexanes. The change in (a) μ_h and (b) V_T were determined from the average of a minimum of 10 devices, where the x-axis legend is the same for both (a) and (b).*

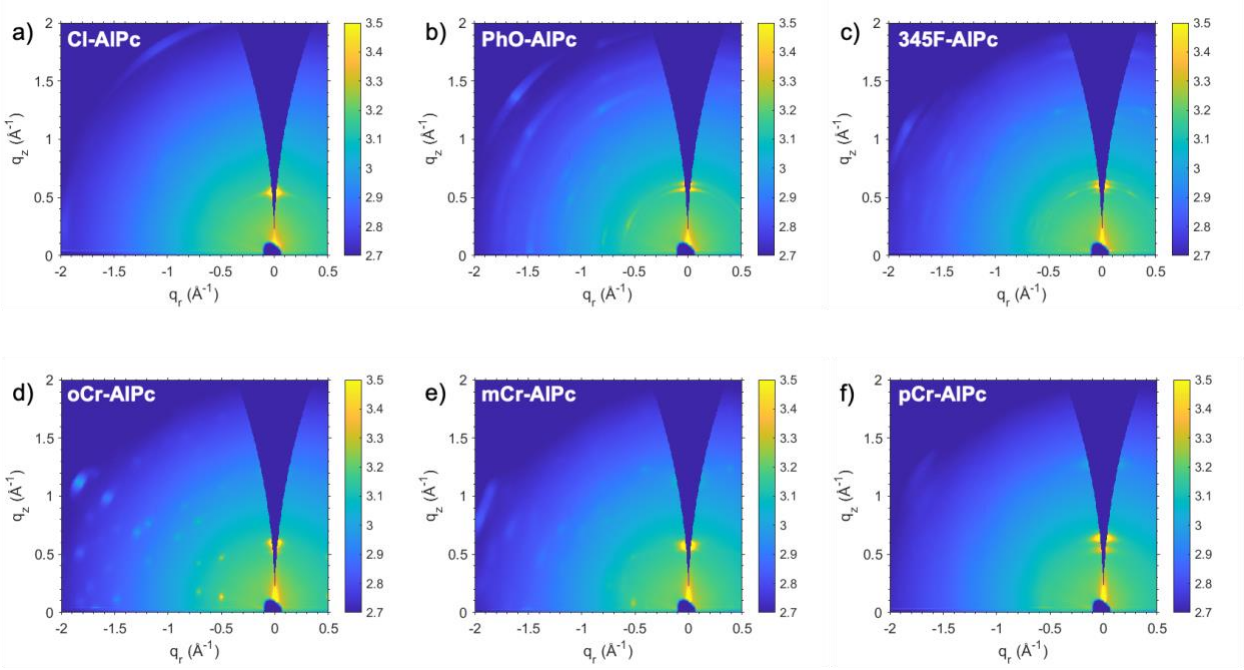

***Figure 3.18**. 2D GIWAXS spectra of (a) Cl-AlPc, (b) PhO-AlPc, (c) 345F-AlPc, (d) oCr-AlPc, (e) mCr-AlPc, and (f) pCr-AlPc films exposed to 300 ppm THC vapor for 90 seconds.*

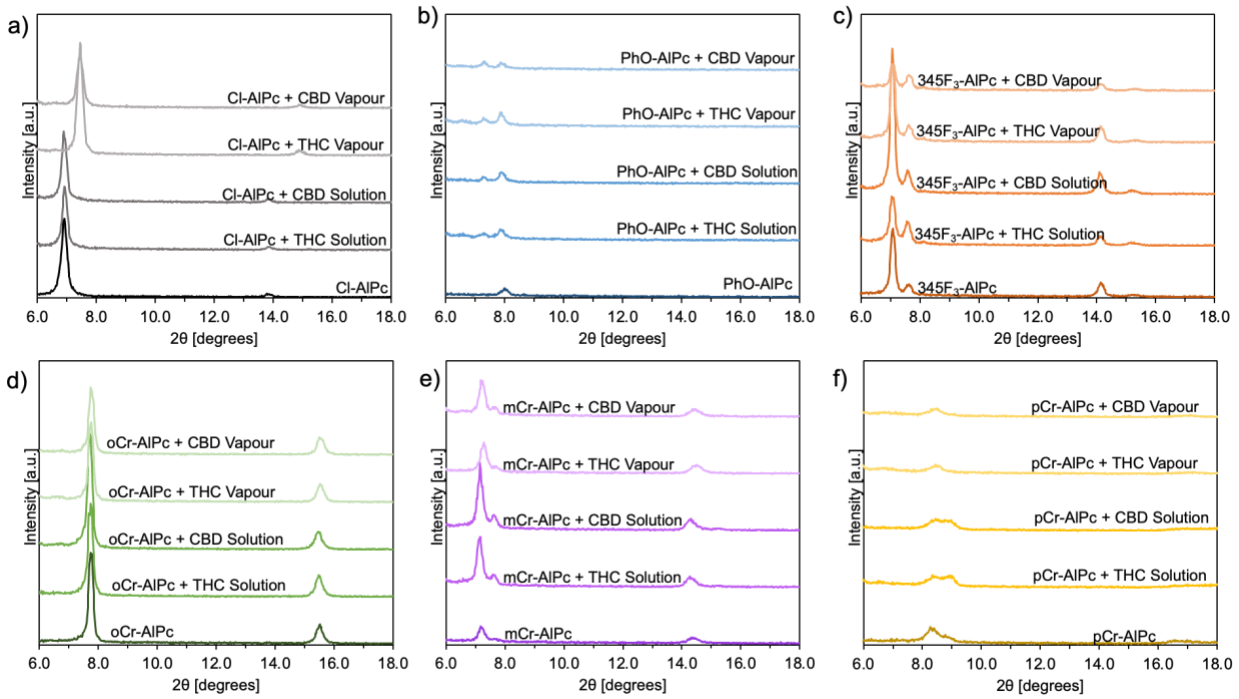

***Figure 3.19**. XRD spectra of (a) Cl-AlPc, (b) PhO-AlPc, (c) 345F-AlPc, (d) oCr-AlPc, (e) mCr-AlPc, and (f) pCr-AlPc thin films, before and after exposure to 20 μM of THC or CBD solution in hexanes, or 300 ppm THC or CBD vapor for 90 seconds.*

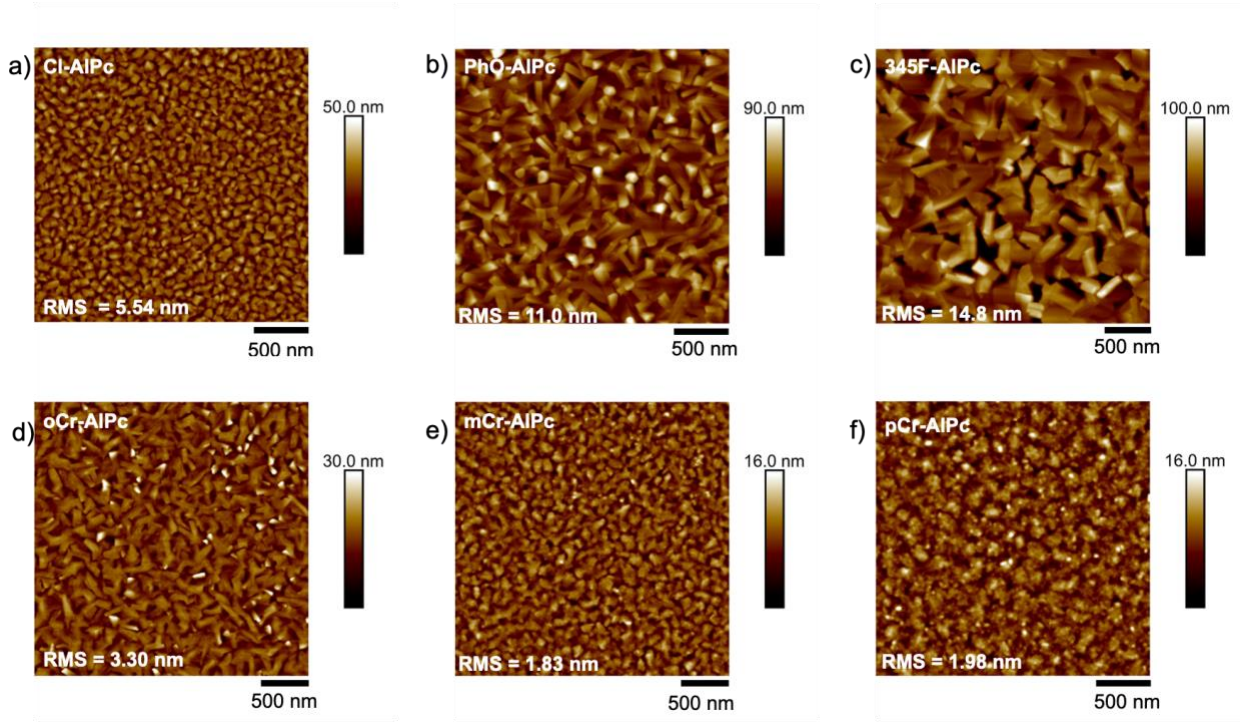

Figure 3.20. *AFM images of (a) Cl-AlPc, (b) PhO-AlPc, (c) 345F$_3$-AlPc, (d) oCr-AlPc, (e) mCr-AlPc, and (f) pCr-AlPc, after exposure to 300 ppm THC vapor for 90 seconds. All images are 2.5 µm x 2.5 µm, with a scale bar of 500 nm.*

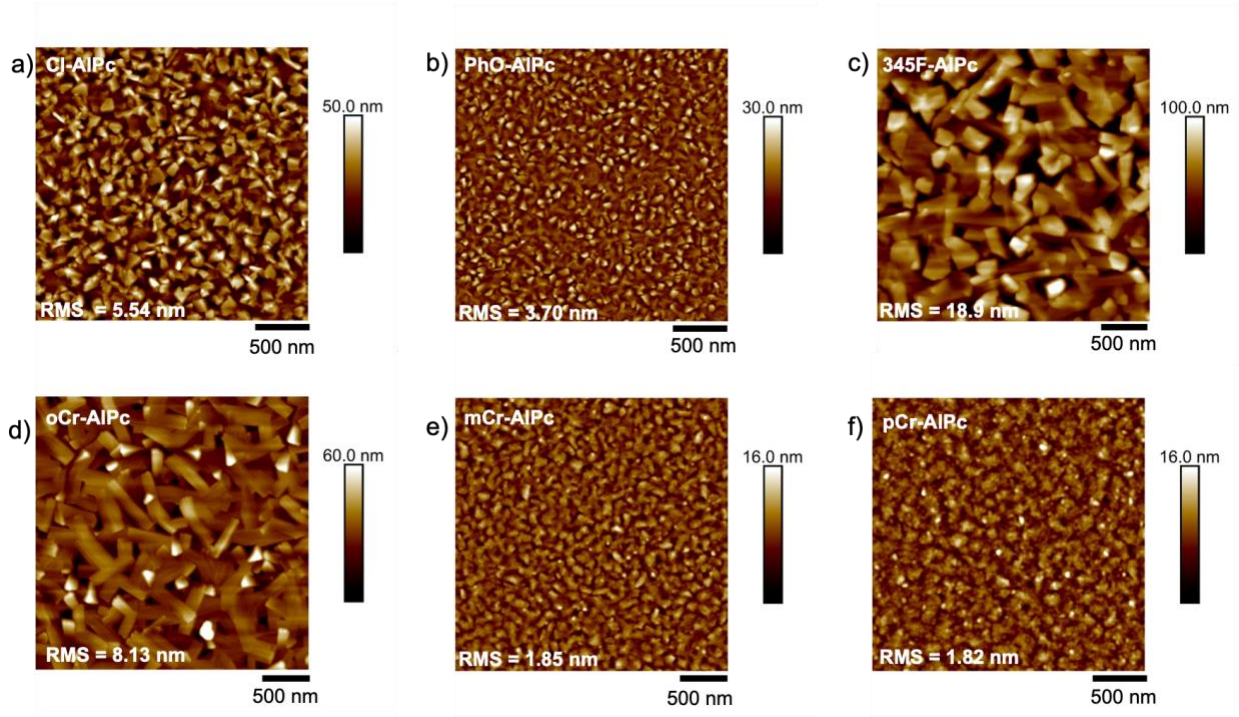

***Figure 3.21**. AFM images of (a) Cl-AlPc, (b) PhO-AlPc, (c) 345F$_3$-AlPc, (d) oCr-AlPc, (e) mCr-AlPc, and (f) pCr-AlPc, after exposure to 300 ppm CBD vapor for 90 seconds. All images are 2.5 µm x 2.5 µm, with a scale bar of 500 nm.*

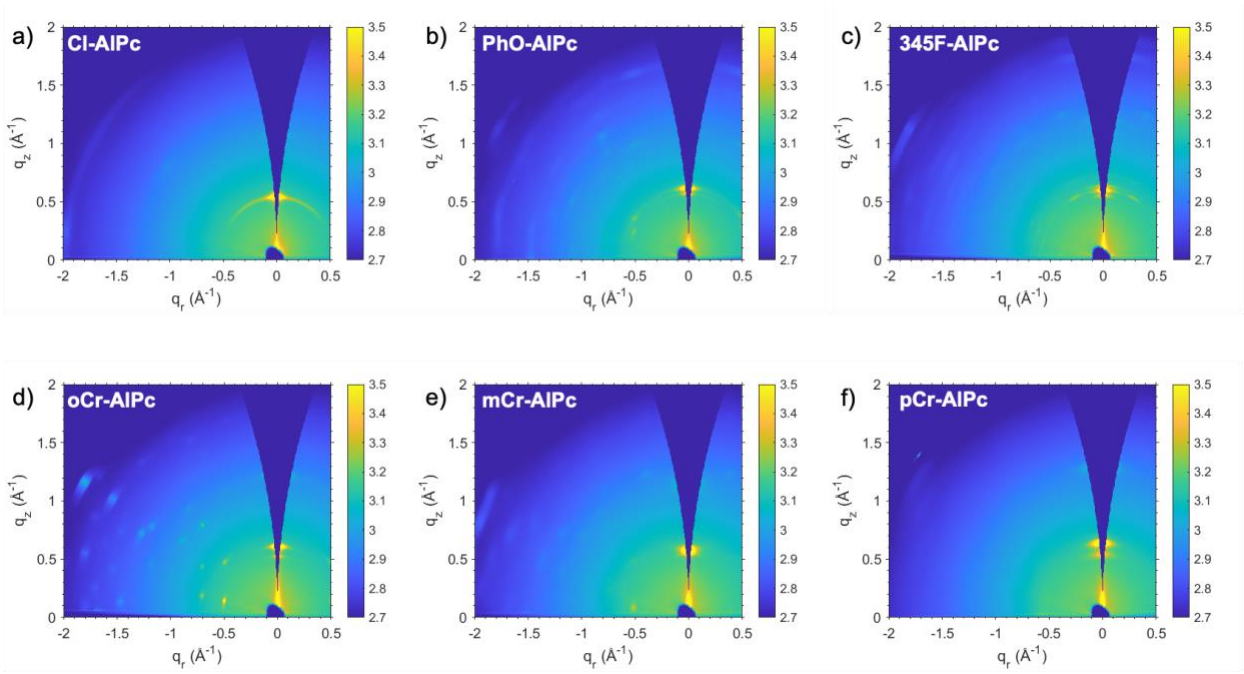

Figure 3.22. *2D GIWAXS spectra of (a) Cl-AlPc, (b) PhO-AlPc, (c) 345F-AlPc, (d) oCr-AlPc, (e) mCr-AlPc, and (f) pCr-AlPc films exposed to 300 ppm CBD vapor for 90 seconds.*

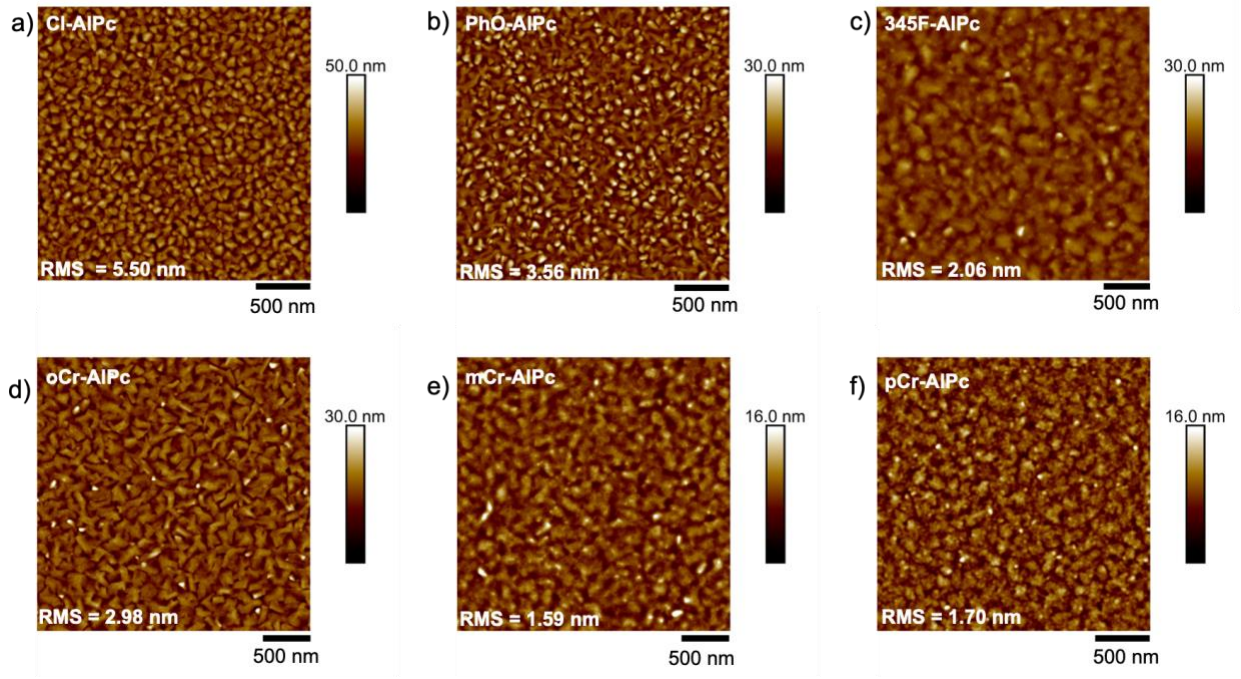

***Figure 3.23**. AFM images of (a) Cl-AlPc, (b) PhO-AlPc, (c) 345F$_3$-AlPc, (d) oCr-AlPc, (e) mCr-AlPc, and (f) pCr-AlPc, after exposure to 20 μM THC solution in hexanes. All images are 2.5 µm x 2.5 µm, with a scale bar of 500 nm.*

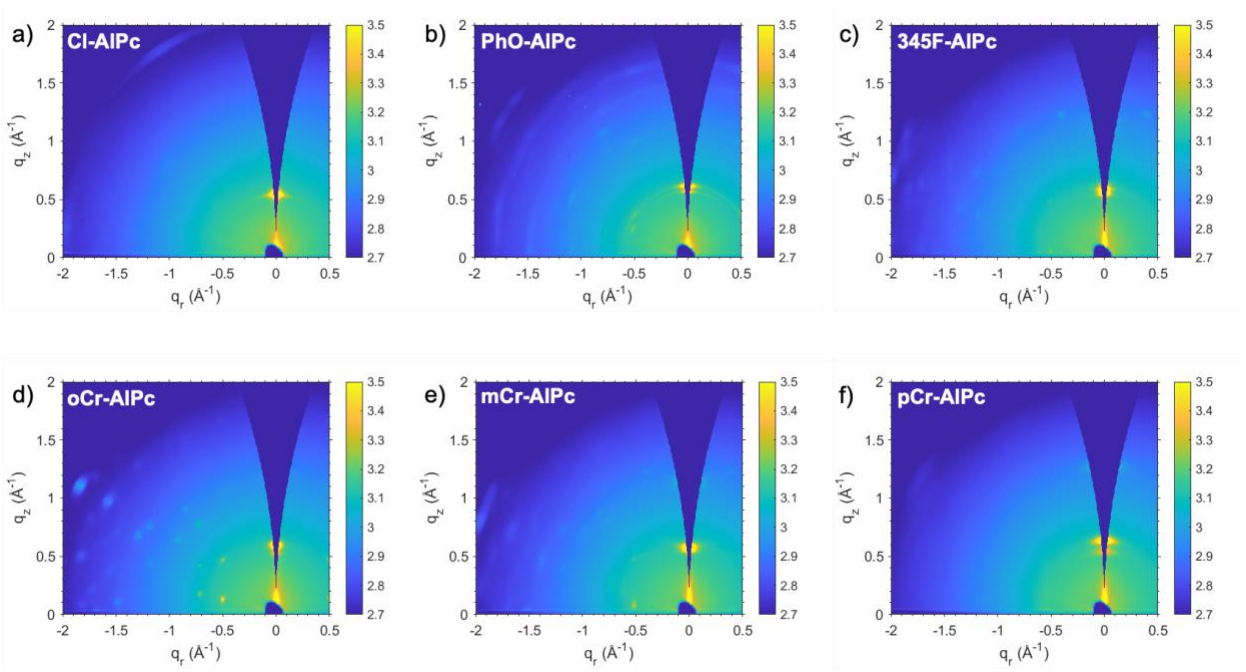

Figure 3.24. *2D GIWAXS spectra of (a) Cl-AlPc, (b) PhO-AlPc, (c) 345F-AlPc, (d) oCr-AlPc, (e) mCr-AlPc, and (f) pCr-AlPc films exposed to 20 μM THC solution in hexanes.*

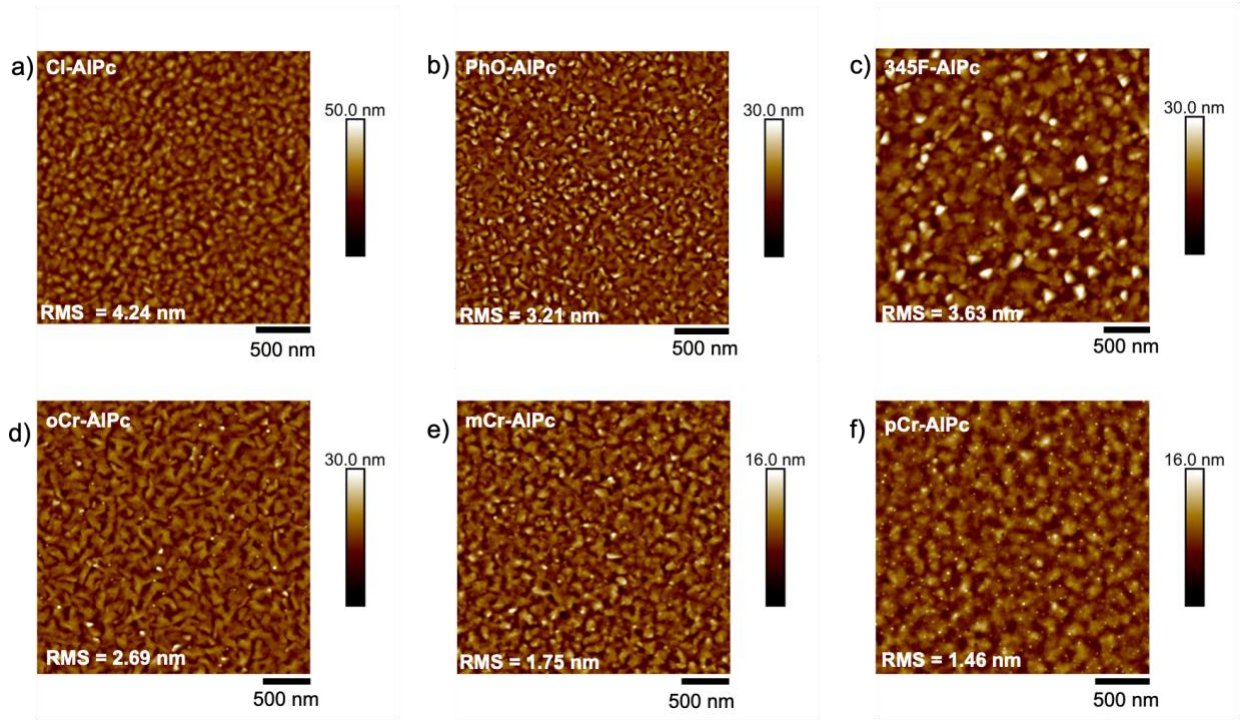

Figure 3.25. *AFM images of (a) Cl-AlPc, (b) PhO-AlPc, (c) 345F$_3$-AlPc, (d) oCr-AlPc, (e) mCr-AlPc, and (f) pCr-AlPc, after exposure to 20 μM CBD solution in hexanes. All images are 2.5 µm x 2.5 µm, with a scale bar of 500 nm.*

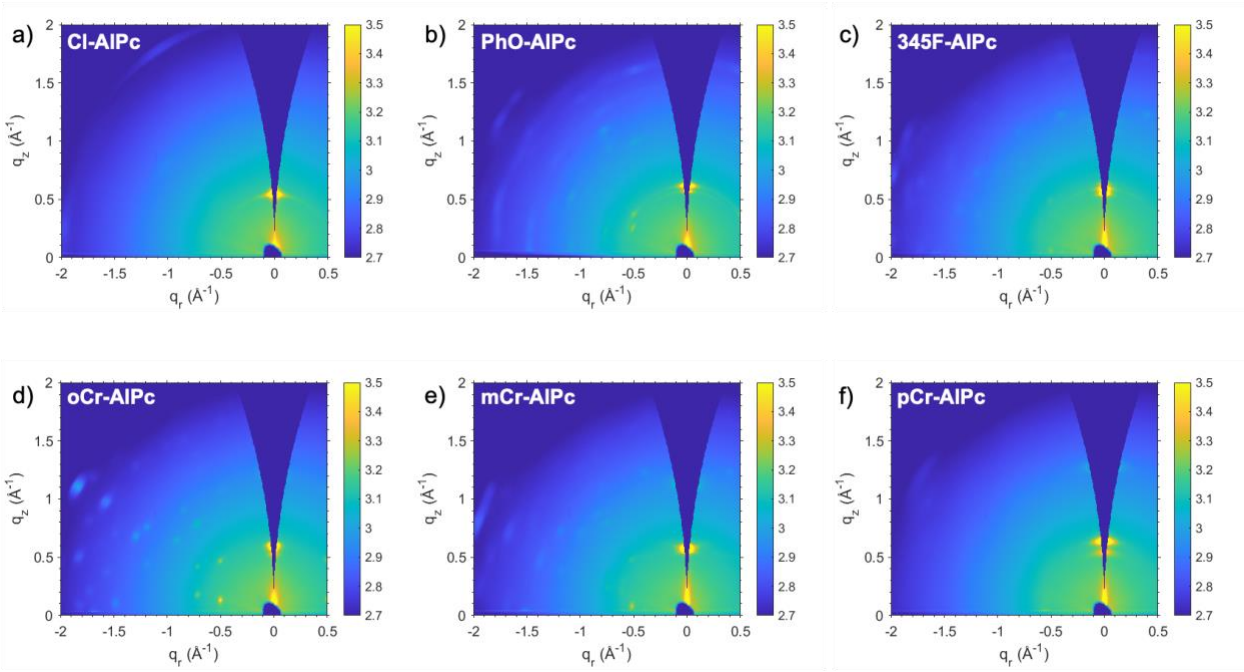

Figure 3.26. *2D GIWAXS spectra of (a) Cl-AlPc, (b) PhO-AlPc, (c) 345F-AlPc, (d) oCr-AlPc, (e) mCr-AlPc, and (f) pCr-AlPc films exposed to 20 μM CBD solution in hexanes.*

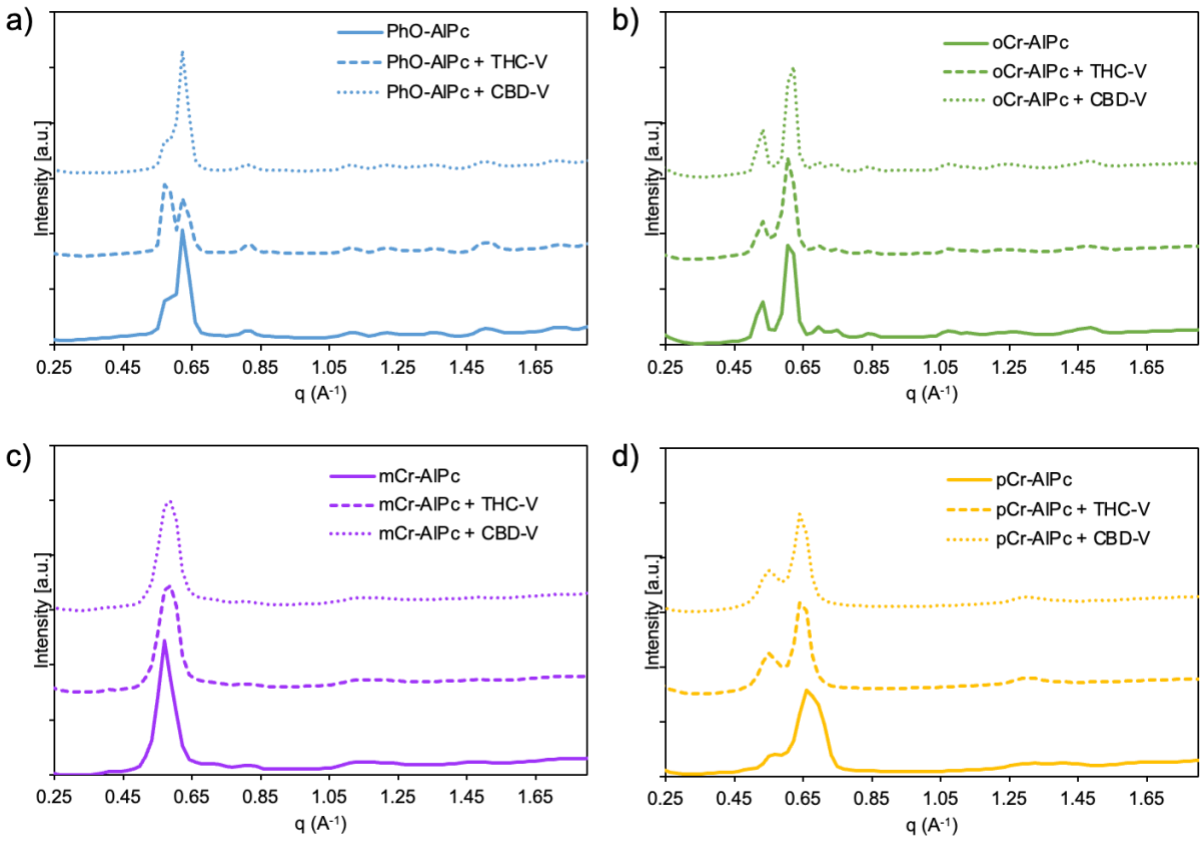

Figure 3.27. *Diffraction pattern of (a) PhO-AlPc, (b) oCr-AlPc, (c) mCr-AlPc, and (d) pCr-AlPc, before and after exposure to 300 ppm THC vapor (THC-V) or 300 ppm CBD vapor (CBD-V), determined by GIWAXS.*

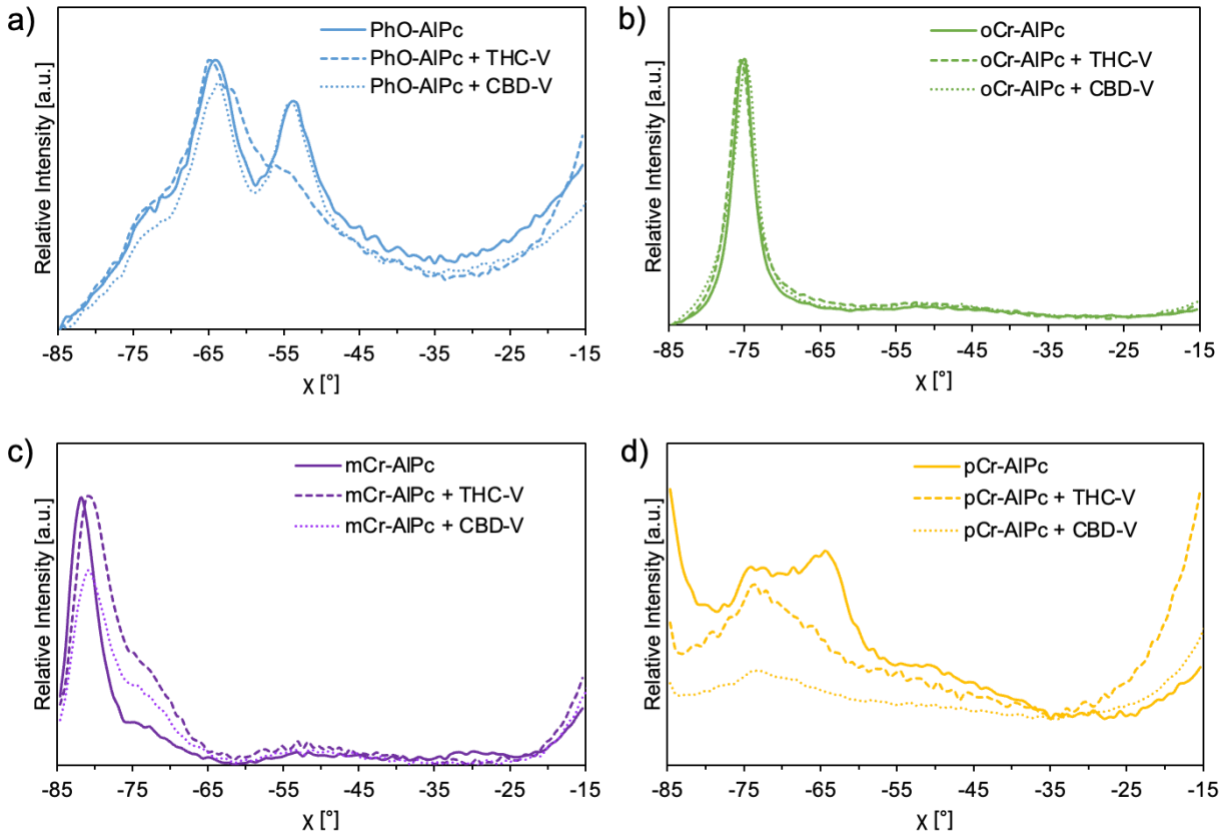

Figure 3.28. *Linecut profiles with respect to χ using a q range of 0.55-0.65 $Å^{-1}$ for (a) PhO-AlPc, (b) oCr-AlPc, (c) mCr-AlPc, and (d) pCr-AlPc before and after exposure to 300 ppm THC vapor (THC-V) or 300 ppm CBD vapor (CBD-V), determined by GIWAXS.*

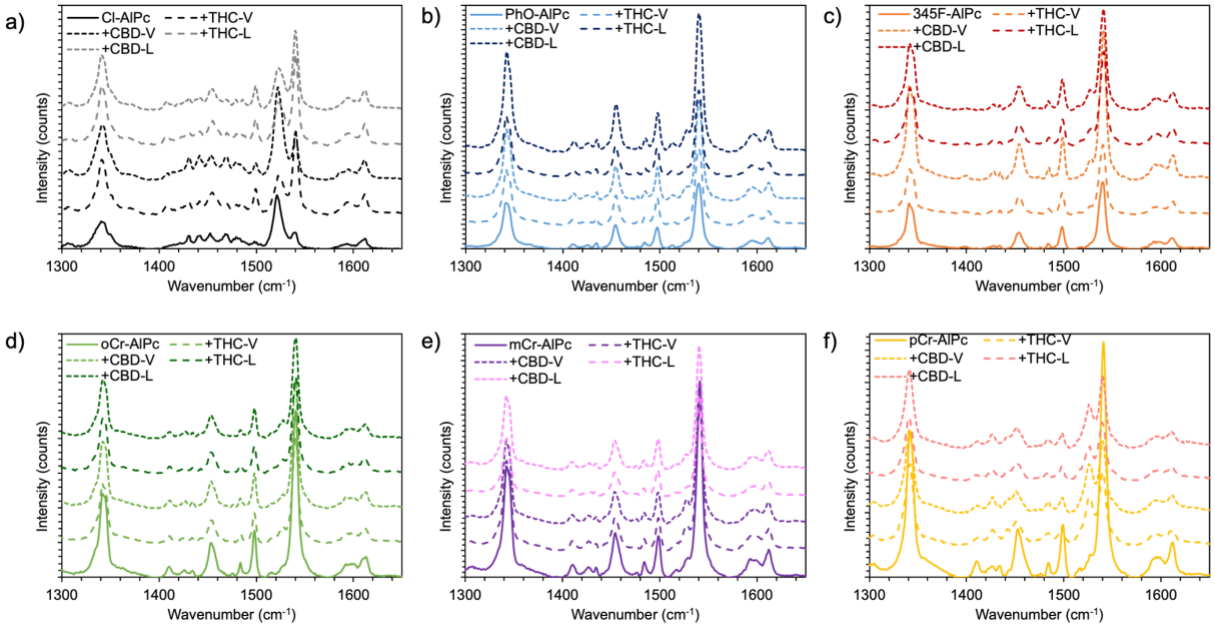

Figure 3.29. *Raman spectra of (a) Cl-AlPc, (b) PhO-AlPc, (c) 345F-AlPc, (d) oCr-AlPc, (e) mCr-AlPc, and (f) pCr-AlPc before and after exposure to THC and CBD vapor and solution. The spectra were collected with a 532 nm laser at 10% power and 1-second exposure.*

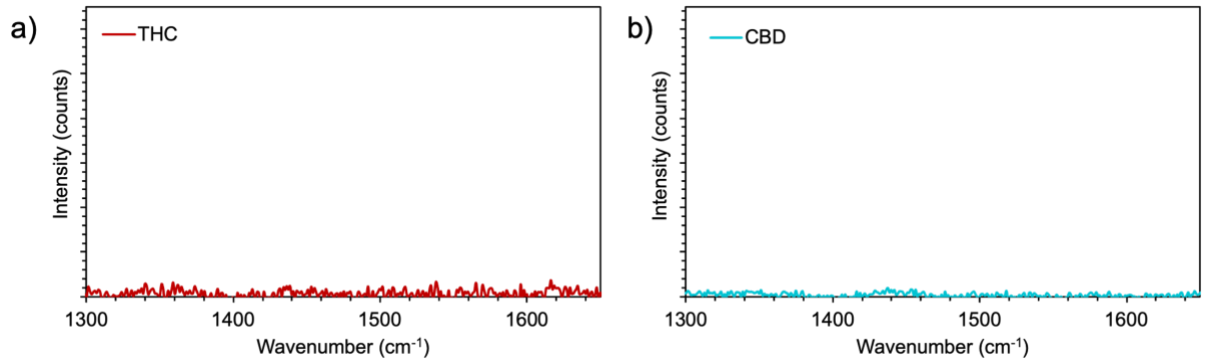

Figure 3.30. *Raman spectra of pure (a) THC and (b) CBD oil collected by a 532 nm laser at 10% power and 5-second exposure.*

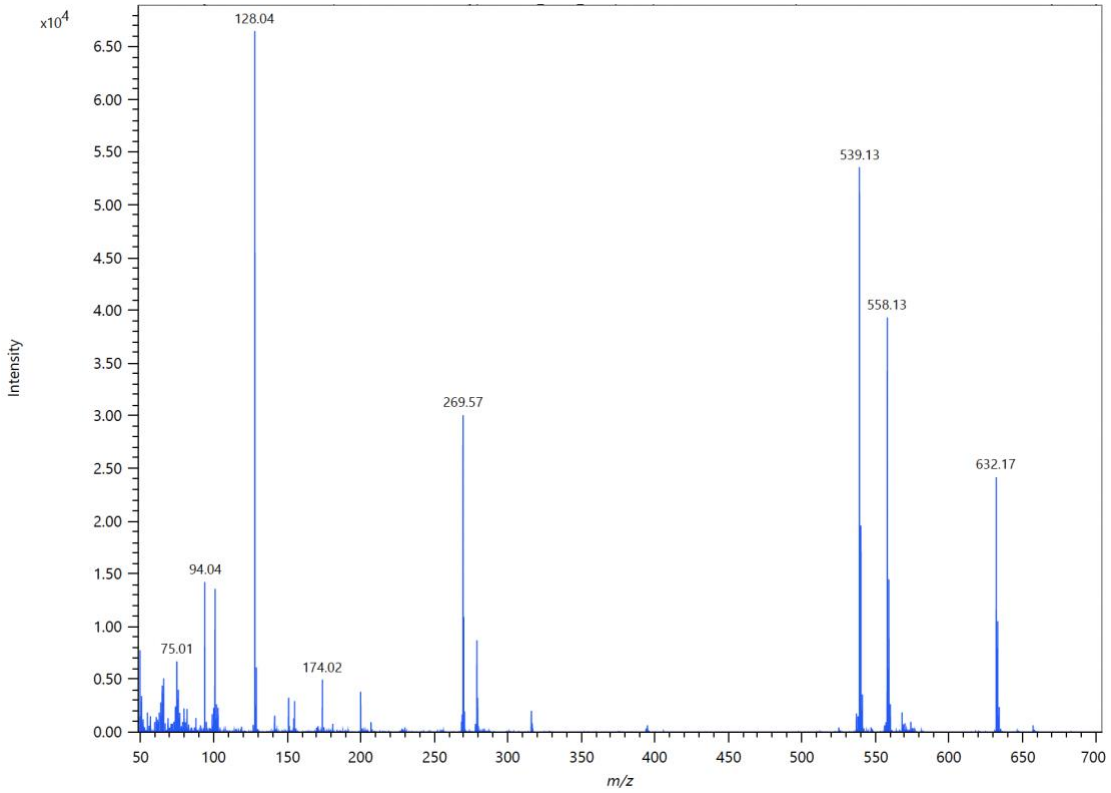

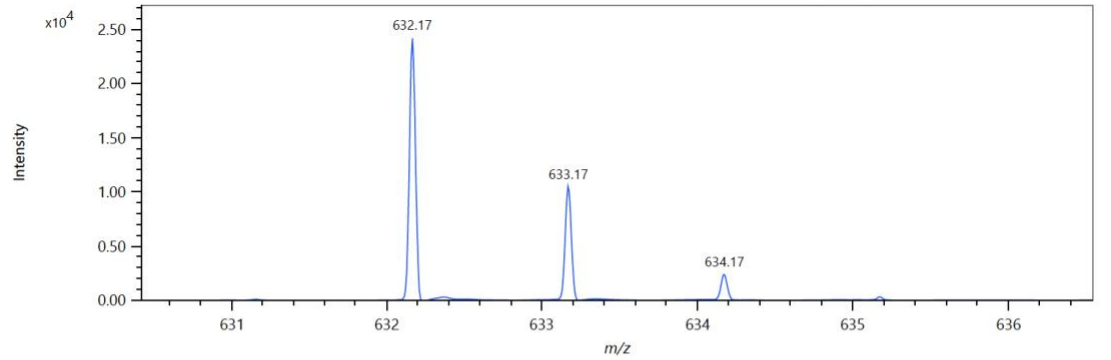

Elemental Composition

Parameters		Elements Set 1:					
Tolerance:	±100.00 mDa	Symbol	C	H	N	O	Al
Electron:	Odd/Even	Min	0	0	0	0	1
Charge:	+1	Max	100	150	10	10	1
DBE:	-1.5 - 60.0						

Results

Mass	Intensity	Formula	Calculated Mass	Mass Difference [mDa]	Mass Difference [ppm]	DBE
632.16519	24169.05	C39 H27 N O6 Al	632.16483	0.36	0.58	27.5
		C38 H21 N8 O Al	632.16482	0.37	0.58	33.0
		C40 H23 N5 O2 Al	632.16616	-0.97	-1.54	32.5
		C26 H25 N10 O8 Al	632.16667	-1.48	-2.34	20.0
		C37 H25 N4 O5 Al	632.16348	1.71	2.70	28.0
		C42 H25 N2 O3 Al	632.16751	-2.32	-3.66	32.0

Figure 3.31. *Low resolution (top) and high resolution mass spectrum (EI) of crude PhO-AlPc.*

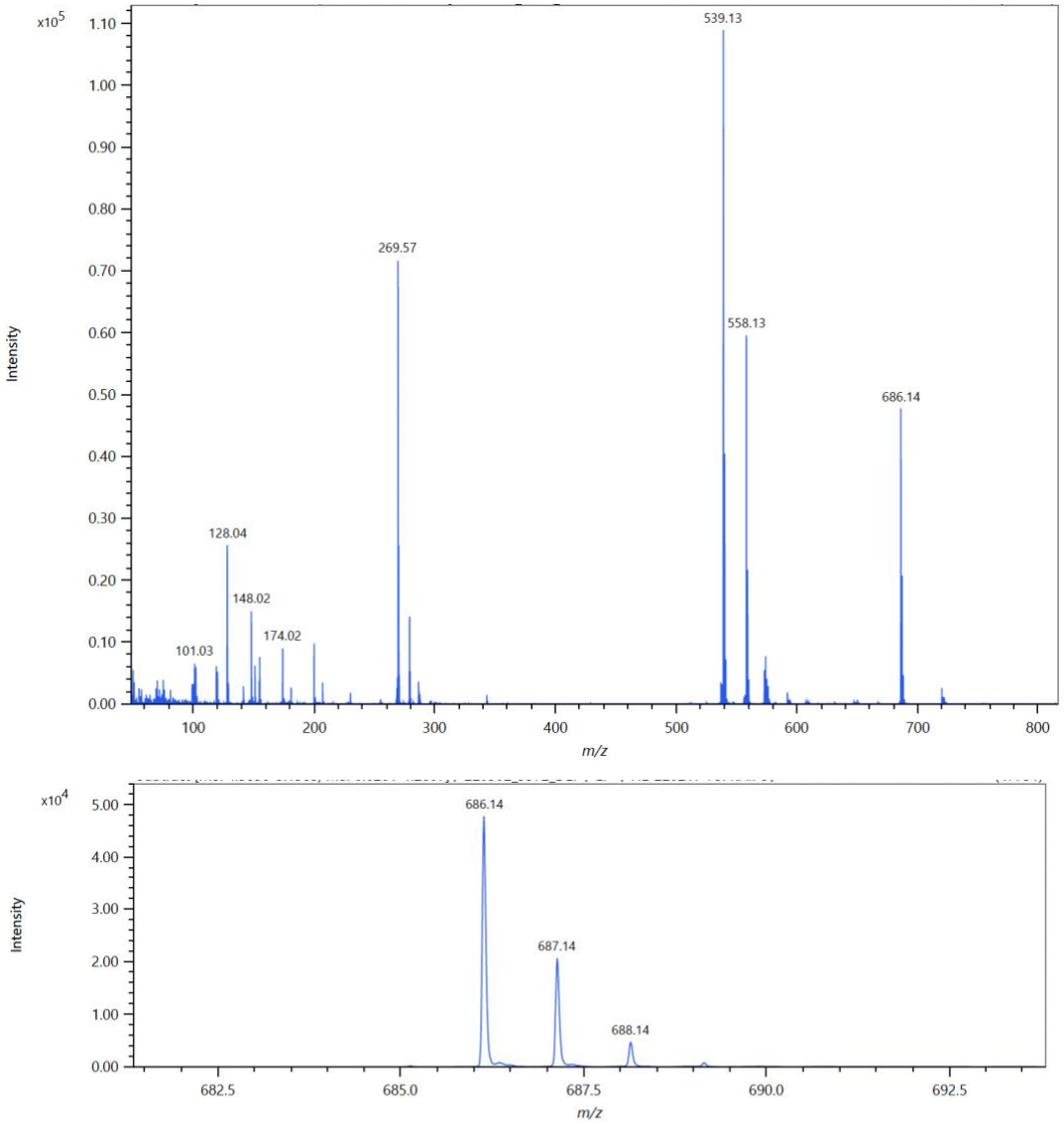

Elemental Composition

Parameters		Elements Set 1:						
Tolerance:	±40.00 mDa	Symbol	C	H	N	O	Al	F
Electron:	Odd/Even	Min	0	0	0	0	1	3
Charge:	+1	Max	100	150	10	10	1	3
DBE:	-1.5 - 60.0							

Results

Mass	Intensity	Formula	Calculated Mass	Mass Difference [mDa]	Mass Difference [ppm]	DBE
686.13704	47751.44	C39 H24 N O6 F3 Al	686.13656	0.48	0.70	27.5
		C38 H18 N8 O F3 Al	686.13656	0.48	0.71	33.0
		C40 H20 N5 O2 F3 Al	686.13790	-0.86	-1.25	32.5
		C26 H22 N10 O8 F3 Al	686.13841	-1.37	-1.99	20.0
		C37 H22 N4 O5 F3 Al	686.13522	1.82	2.66	28.0
		C42 H22 N2 O3 F3 Al	686.13924	-2.20	-3.21	32.0

Figure 3.32. *Low resolution (top) and high resolution (bottom) mass spectrum (EI) of crude 345F-AlPc.*

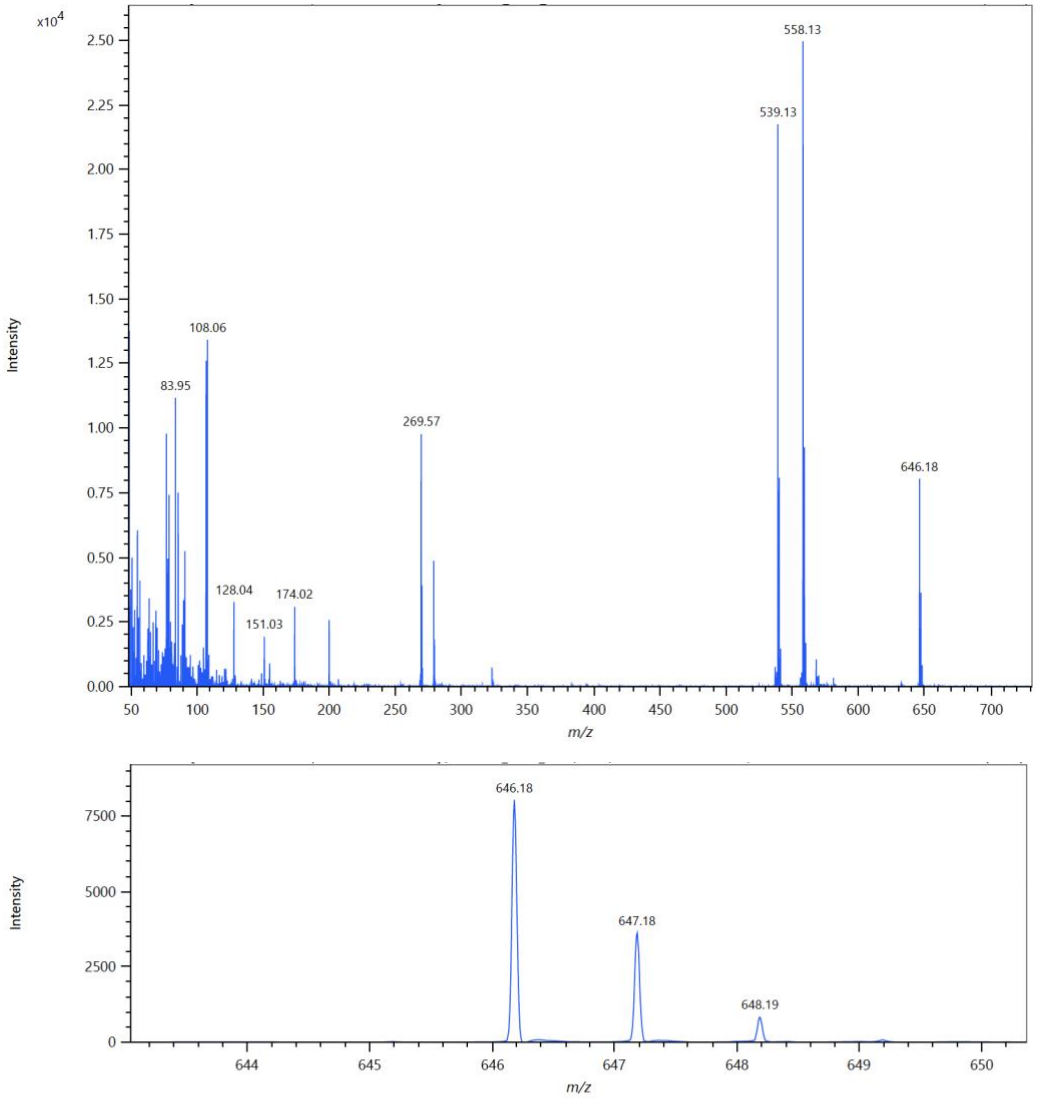

Elemental Composition

Parameters		Elements Set 1:					
Tolerance:	±100.00 mDa	Symbol	C	H	N	O	Al
Electron:	Odd/Even	Min	0	0	0	0	1
Charge:	+1	Max	100	150	10	10	1
DBE:	-1.5 - 60.0						

Results

Mass	Intensity	Formula	Calculated Mass	Mass Difference [mDa]	Mass Difference [ppm]	DBE
646.18154	8042.70	C41 H25 N5 O2 Al	646.18181	-0.28	-0.43	32.5
		C27 H27 N10 O8 Al	646.18232	-0.79	-1.22	20.0
		C40 H29 N O6 Al	646.18048	1.06	1.64	27.5
		C39 H23 N8 O Al	646.18047	1.07	1.65	33.0
		C43 H27 N2 O3 Al	646.18316	-1.62	-2.51	32.0
		C29 H29 N7 O9 Al	646.18367	-2.13	-3.29	19.5

***Figure 3.33**. Low resolution (top) and high resolution (bottom) mass spectrum (EI) of crude oCr-AlPc*

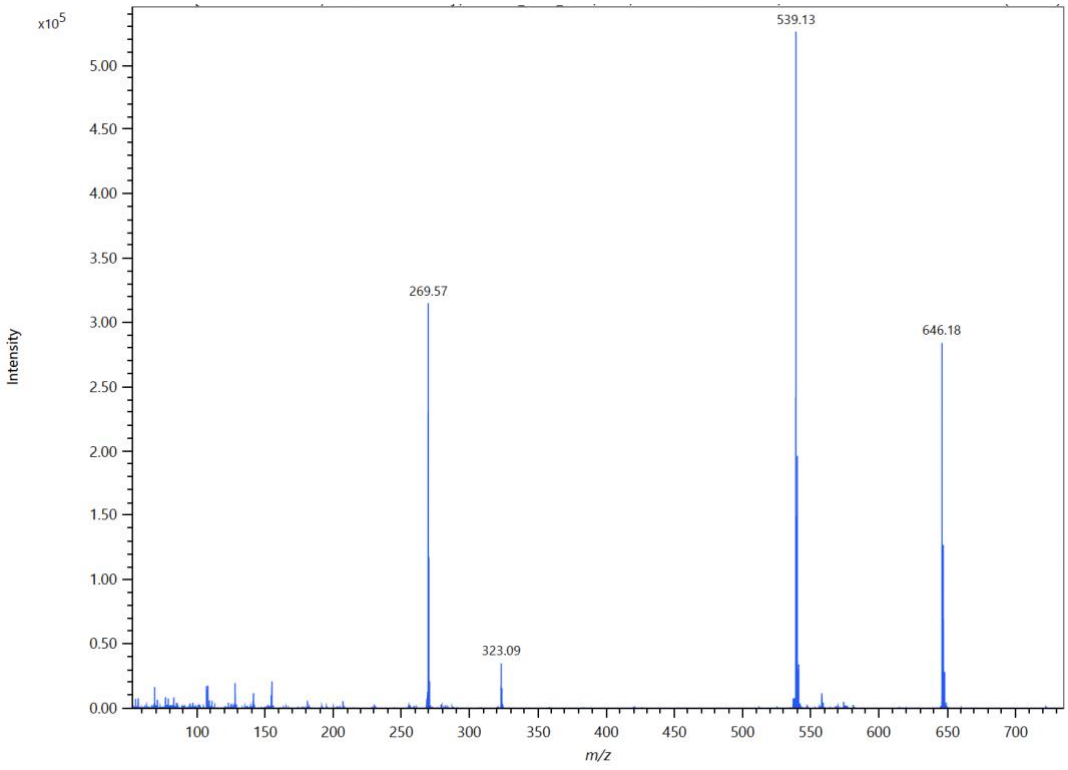

Elemental Composition

Parameters		Elements Set 1:					
Tolerance:	±100.00 mDa	Symbol	C	H	N	O	Al
Electron:	Odd/Even	Min	0	0	0	0	1
Charge:	+1	Max	100	150	10	10	1
DBE:	-1.5 - 60.0						

Results

Mass	Intensity	Formula	Calculated Mass	Mass Difference [mDa]	Mass Difference [ppm]	DBE
646.17852	283989.92	C38 H27 N4 O5 Al	646.17913	-0.62	-0.96	28.0
		C37 H31 O9 Al	646.17780	0.72	1.11	23.0
		C36 H25 N7 O4 Al	646.17779	0.73	1.12	28.5
		C39 H23 N8 O Al	646.18047	-1.95	-3.03	33.0
		C40 H29 N O6 Al	646.18048	-1.96	-3.03	27.5
		C35 H29 N3 O8 Al	646.17645	2.06	3.19	23.5

Figure 3.34. *Low resolution (top) and high resolution (bottom) mass spectrum (EI) of crude mCr-AlPc.*

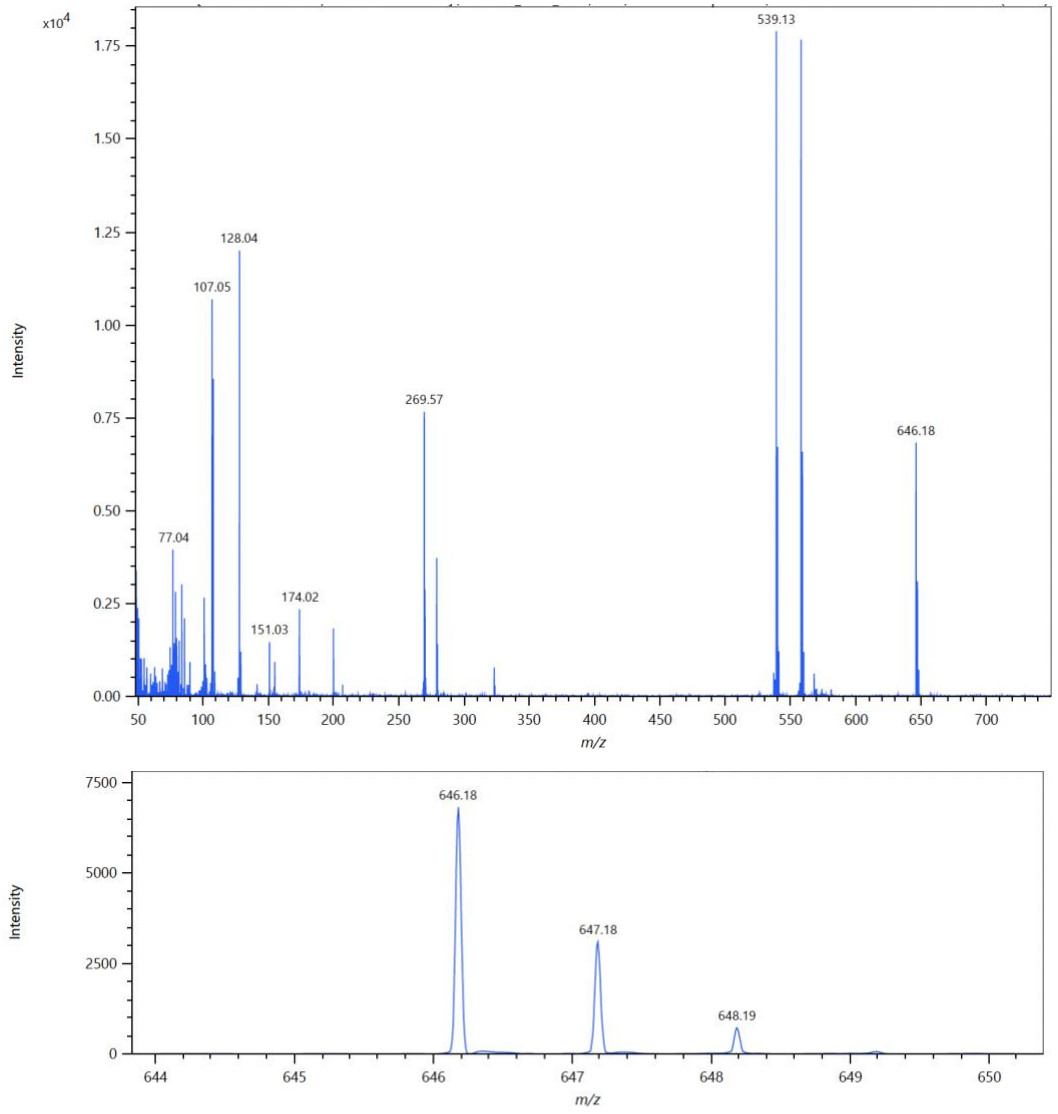

Elemental Composition

Parameters		Elements Set 1:					
Tolerance:	±100.00 mDa	Symbol	C	H	N	O	Al
Electron:	Odd/Even	Min	0	0	0	0	1
Charge:	+1	Max	100	150	10	10	1
DBE:	-1.5 - 60.0						

Results

Mass	Intensity	Formula	Calculated Mass	Mass Difference [mDa]	Mass Difference [ppm]	DBE
646.18114	6827.35	C40 H29 N O6 Al	646.18048	0.66	1.02	27.5
		C39 H23 N8 O Al	646.18047	0.67	1.03	33.0
		C41 H25 N5 O2 Al	646.18181	-0.68	-1.05	32.5
		C27 H27 N10 O8 Al	646.18232	-1.18	-1.83	20.0
		C38 H27 N4 O5 Al	646.17913	2.00	3.10	28.0
		C43 H27 N2 O3 Al	646.18316	-2.02	-3.12	32.0

***Figure 3.35**. Low resolution (top) and high resolution (bottom) mass spectrum (EI) of crude pCr-AlPc*

3.10 References

[1] L. Zuurman, C. Roy, R. Schoemaker, A. Hazekamp, J. den Hartigh, J. Bender, R. Verpoorte, J. Pinquier, A. Cohen, J. van Gerven, *J Psychopharmacol* **2008**, *22*, 707.
[2] J. Meehan-Atrash, I. Rahman, *Chem. Res. Toxicol.* **2021**, *34*, 2169.
[3] W. Guo, G. Vrdoljak, V.-C. Liao, B. Moezzi, *Front Chem* **2021**, *9*, 694905.
[4] A. Gowran, J. Noonan, V. A. Campbell, *CNS Neurosci Ther.* **2011**, *17*, 637.
[5] E. B. Russo, *Chem. Biodiversity* **2007**, *4*, 1614.
[6] A. DI, *Eur. J. Intern. Med.* **2018**, *49*, 7.
[7] A. A. M. Stolker, J. van Schoonhoven, A. J. de Vries, I. Bobeldijk-Pastorova, W. H. J. Vaes, R. van den Berg, *J. Chromatogr. A* **2004**, *1058*, 143.
[8] B. De Backer, B. Debrus, P. Lebrun, L. Theunis, N. Dubois, L. Decock, A. Verstraete, P. Hubert, C. Charlier, *J. Chromatogr. B Biomed. Appl.* **2009**, *877*, 4115.
[9] Z. J. Comeau, N. T. Boileau, T. Lee, O. A. Melville, N. A. Rice, Y. Troung, C. S. Harris, B. H. Lessard, A. J. Shuhendler, *ACS Sens.* **2019**, *4*, 2706.
[10] Z. J. Comeau, G. A. Facey, C. S. Harris, A. J. Shuhendler, B. H. Lessard, *ACS Appl Mater Interfaces* **2020**, *12*, 50692.
[11] Z. J. Comeau, N. A. Rice, C. S. Harris, A. J. Shuhendler, B. H. Lessard, *Adv. Funct. Mater.* **2022**, *32*, 2107138.
[12] H. R. Lamontagne, Z. J. Comeau, R. R. Cranston, N. T. Boileau, C. S. Harris, A. J. Shuhendler, B. H. Lessard, *Sens. Diagn.* **2022**, *1*, 1165.
[13] Z. J. Comeau, R. R. Cranston, H. R. Lamontagne, C. S. Harris, A. J. Shuhendler, B. H. Lessard, *Commun Chem* **2022**, *5*, 1.
[14] C. G. Claessens, U. Hahn, T. Torres, *Chem. Rec.* **2008**, *8*, 75.
[15] M. A. Dahlen, *Ind. Eng. Chem.* **1939**, *31*, 839.
[16] O. A. Melville, B. H. Lessard, T. P. Bender, *ACS Appl Mater Interfaces* **2015**, *7*, 13105.
[17] R. R. Cranston, B. King, C. Dindault, T. M. Grant, N. A. Rice, C. Tonnelé, L. Muccioli, F. Castet, S. Swaraj, B. H. Lessard, *J. Mater. Chem. C* **2022**, *10*, 485.
[18] R. R. Cranston, M. C. Vebber, N. A. Rice, C. Tonnelé, F. Castet, L. Muccioli, J. L. Brusso, B. H. Lessard, *ACS Appl. Electron. Mater.* **2021**, *3*, 1873.
[19] N. T. Boileau, O. A. Melville, B. Mirka, R. Cranston, B. H. Lessard, *RSC Advances* **2019**, *9*, 2133.
[20] R. Ben Chaabane, A. Ltaief, C. Dridi, H. Rahmouni, A. Bouazizi, H. Ben Ouada, *Thin Solid Films* **2003**, *427*, 371.
[21] X. Shao, S. Wang, X. Li, Z. Su, Y. Chen, Y. Xiao, *Dyes Pigm.* **2016**, *132*, 378.
[22] X. Li, Y. Jiang, G. Xie, H. Tai, P. Sun, B. Zhang, *Sens. Actuators B: Chem* **2013**, *176*, 1191.
[23] G. de la Torre, G. Bottari, T. Torres, *Adv. Energy Mater.* **2017**, *7*, 1601700.
[24] T. M. Grant, D. S. Josey, K. L. Sampson, T. Mudigonda, T. P. Bender, B. H. Lessard, *Chem. Rec.* **2019**, *19*, 1093.
[25] M. V. Martínez-Díaz, G. de la Torre, T. Torres, *Chem. Commun.* **2010**, *46*, 7090.
[26] E. R. L. Brisson, A. S. Paton, G. E. Morse, T. P. Bender, *Ind. Eng. Chem. Res.* **2011**, *50*, 10910.
[27] S. m. O'Flaherty, S. v. Hold, M. j. Cook, T. Torres, Y. Chen, M. Hanack, W. j. Blau, *Adv. Mater.* **2003**, *15*, 19.
[28] B. A. Kamino, T. P. Bender, *Dalton Trans.* **2013**, *42*, 13145.

[29] M. C. Vebber, B. King, C. French, M. Tousignant, B. Ronnasi, C. Dindault, G. Wantz, L. Hirsch, J. Brusso, B. H. Lessard, *Can J Chem Eng.* **2023**, *101*, 3019.
[30] M. V. Fulford, D. Jaidka, A. S. Paton, G. E. Morse, E. R. L. Brisson, A. J. Lough, T. P. Bender, *J. Chem. Eng. Data* **2012**, *57*, 2756.
[31] A. S. Paton, G. E. Morse, A. J. Lough, T. P. Bender, *Cryst Eng Comm* **2011**, *13*, 914.
[32] G. E. Morse, M. G. Helander, J. Stanwick, J. M. Sauks, A. S. Paton, Z.-H. Lu, T. P. Bender, *J. Phys. Chem. C* **2011**, *115*, 11709.
[33] J. Guilleme, L. Martínez-Fernández, D. González-Rodríguez, I. Corral, M. Yáñez, T. Torres, *J. Am. Chem. Soc.* **2014**, *136*, 14289.
[34] C. A. Barker, K. S. Findlay, S. Bettington, A. S. Batsanov, I. F. Perepichka, M. R. Bryce, A. Beeby, *Tetrahedron* **2006**, *62*, 9433.
[35] R. R. Cranston, M. C. Vebber, J. F. Berbigier, N. A. Rice, C. Tonnelé, Z. J. Comeau, N. T. Boileau, J. L. Brusso, A. J. Shuhendler, F. Castet, L. Muccioli, T. L. Kelly, B. H. Lessard, *ACS Appl Mater Interfaces* **2021**, *13*, 1008.
[36] R. R. Cranston, M. C. Vebber, J. Faleiro Berbigier, J. Brusso, T. L. Kelly, B. H. Lessard, *Adv. Electron. Mater.* **2022**, *8*, 2200696.
[37] B. King, A. J. Daszczynski, N. A. Rice, A. J. Peltekoff, N. J. Yutronkie, B. H. Lessard, J. L. Brusso, *ACS Appl. Electron. Mater.* **2021**, *3*, 2212.
[38] B. King, O. A. Melville, N. A. Rice, S. Kashani, C. Tonnelé, H. Raboui, S. Swaraj, T. M. Grant, T. McAfee, T. P. Bender, H. Ade, F. Castet, L. Muccioli, B. H. Lessard, *ACS Appl. Electron. Mater.* **2021**, *3*, 325.
[39] McKeown, Neil B., *Phthalocyanine Materials: Synthesis, Structure, and Function*, Cambridge University Press., **1998**.
[40] L. Li, Q. Tang, H. Li, W. Hu, X. Yang, Z. Shuai, Y. Liu, D. Zhu, *Pure Appl. Chem.* **2008**, *80*, 2231.
[41] G. de la Torre, C. G. Claessens, T. Torres, *Chem. Commun.* **2007**, 2000.
[42] G. de la Torre, P. Vázquez, F. Agulló-López, T. Torres, *J. Mater. Chem.* **1998**, *8*, 1671.
[43] B. H. Lessard, *ACS Appl Mater Interfaces* **2021**, *13*, 31321.
[44] M. C. Vebber, N. A. Rice, J. L. Brusso, B. H. Lessard, *ACS Appl. Energy Mater.* **2022**, *5*, 3426.
[45] O. A. Melville, T. M. Grant, K. Lochhead, B. King, R. Ambrose, N. A. Rice, N. T. Boileau, A. J. Peltekoff, M. Tousignant, I. G. Hill, B. H. Lessard, *ACS Appl. Electron. Mater.* **2020**, *2*, 1313.
[46] N. J. Yutronkie, B. King, O. A. Melville, B. H. Lessard, J. L. Brusso, *J. Mater. Chem. C* **2021**, *9*, 10119.
[47] L. Torsi, A. Dodabalapur, L. Sabbatini, P. G. Zambonin, *Sens. Actuators B: Chem* **2000**, *67*, 312.
[48] J. Liu, M. Agarwal, K. Varahramyan, *Sens. Actuators B: Chem* **2008**, *135*, 195.
[49] G. Seo, G. Lee, M. J. Kim, S.-H. Baek, M. Choi, K. B. Ku, C.-S. Lee, S. Jun, D. Park, H. G. Kim, S.-J. Kim, J.-O. Lee, B. T. Kim, E. C. Park, S. I. Kim, *ACS Nano* **2020**, *14*, 5135.
[50] S. Ganesh Moorthy, B. King, A. Kumar, E. Lesniewska, B. H. Lessard, M. Bouvet, *Adv. Sensor Res.* **2023**, *2*, 2200030.
[51] K. J. Wynne, *Inorg. Chem.* **1984**, *23*, 4658.

[52] J. D. Virdo, L. Crandall, J. D. Dang, M. V. Fulford, A. J. Lough, W. S. Durfee, T. P. Bender, *Cryst Eng Comm* **2013**, *15*, 8578.
[53] A. S. Paton, A. J. Lough, T. P. Bender, *Ind. Eng. Chem. Res.* **2012**, *51*, 6290.
[54] J. D. Virdo, Y. H. Kawar, A. J. Lough, T. P. Bender, *Cryst Eng Comm* **2013**, *15*, 3187.
[55] H. Raboui, M. AL-Amar, A. I. Abdelrahman, T. P. Bender, *RSC Adv.* **2015**, *5*, 45731.
[56] B. H. Lessard, T. M. Grant, R. White, E. Thibau, Z.-H. Lu, T. P. Bender, *J. Mater. Chem. A* **2015**, *3*, 24512.
[57] A. J. Pearson, T. Plint, S. T. E. Jones, B. H. Lessard, D. Credgington, T. P. Bender, N. C. Greenham, *J. Mater. Chem. C* **2017**, *5*, 12688.
[58] M.-T. Dang, T. M. Grant, H. Yan, D. S. Seferos, B. H. Lessard, T. P. Bender, *J. Mater. Chem. A* **2017**, *5*, 12168.
[59] R. R. Cranston, B. H. Lessard, *RSC Adv.* **2021**, *11*, 21716.
[60] N. T. Boileau, R. Cranston, B. Mirka, O. A. Melville, B. H. Lessard, *RSC Adv.* **2019**, *9*, 21478.
[61] M. Chen, L. Yan, Y. Zhao, I. Murtaza, H. Meng, W. Huang, *J. Mater. Chem. C* **2018**, *6*, 7416.
[62] A. Di Carlo, F. Piacenza, A. Bolognesi, B. Stadlober, H. Maresch, *Applied Physics Letters* **2005**, *86*, 263501.
[63] B. King, M. C. Vebber, R. Ewenike, M. Dupuy, C. French, J. L. Brusso, B. H. Lessard, *Chem. Mater.* **2023**, *35*, 8517.
[64] R. Aroca, C. Jennings, R. O. Loutfy, A.-M. Hor, *Spectrochim Acta A Mol Spectrosc* **1987**, *43*, 725.
[65] T. V. Basova, V. G. Kiselev, V. A. Plyashkevich, P. B. Cheblakov, F. Latteyer, H. Peisert, T. Chassè, *Chemical Physics* **2011**, *380*, 40.

Chapter 4: $(F_5PhO)_2$-F_{16}-SiPc as an Air-Stable, High-Performance *N*-Type Semiconductor with Poor Cannabinoid Sensing Capabilities

This chapter is adapted from: ***Halynne R. Lamontagne****, Mélanie Cyr, Mario Vebber, Sufal Swaraj, Cory S. Harris, Jaclyn L. Brusso, Adam J. Shuhendler & Benoît H. Lessard; RSC Applied Interfaces, 2024, 1, 1222-1232.*
DOI: 10.1039/D4LF00147H

4.1 Context

The library of available air-stable, *n*-type semiconductors is significantly smaller than their *p*-type counterparts due to their susceptibility to oxidation in air from their shallow LUMO levels, as described previously in **Chapter 1**. As a continuation of the strategy used in **Chapter 3**, my colleagues had chemically modified an *n*-type semiconductor, R_2-SiPc, with peripheral and axial fluorines to lower the LUMO level to make $(F_5PhO)_2$-F_{16}-SiPc, which was air-stable. Using this molecule in an OTFT sensor could potentially expand the useful *n*-type library, so I wanted to investigate the sensing properties of this material through electrical characterization. I also sought to investigate its thin film properties to explore why it was such a successful semiconductor, and if it experienced the same type of film reorganization upon exposure to THC and CBD. In the absence of single-crystal diffraction data for this molecule, I used a combination of NEXAFS and Raman with GIWAXS to characterize the orientation of the main isoindole plane to the substrate. $(F_5PhO)_2$-F_{16}-SiPc experienced no significant electrical response to THC or CBD and no thin film reorganization, likely due to the relatively low reactivity of the central metal, and the lack of hydrogens in the structure to interact with the cannabinoids. The thin-film characterization techniques all suggest a crystalline, mixed orientation film with the main plane oriented in the majority edge-on direction, which is advantageous for charge transport.

4.2 Contributions of Authors

I fabricated all devices and substrates for film characterization. I performed all OTFT characterization, interpreted the data, and performed all cannabinoid exposure

studies. I also performed all GIWAXS, Raman, and NEXAFS experiments and interpreted all the data. MC and MV synthesized and purified the $(F_5PhO)_2$-F_{16}-SiPc used in this study. SS assisted with the NEXAFS experiments and data interpretation. I authored the manuscript, and MC, SS, AJS, and BHL gave editorial contributions. This work was supervised by JLB, AJS, and BHL.

4.3 Abstract

Organic thin-film transistors (OTFTs) are an emerging platform for rapid, point-of-source detection and speciation of Δ^9-tetrahydrocannabinol (THC) and cannabidiol (CBD). $(F_5PhO)_2$-F_{16}-SiPc semiconductor was implemented into high performance, air stable *n*-type bottom gate, bottom contact OTFTs, however, the resulting device performance changes in response to THC and CBD were negligible. We explored the orientation of the corresponding thin films by synchrotron-based grazing incidence wide-angle x-ray scattering (GIWAXS) and angle-dependent near-edge X-ray absorption fine structure (NEXAFS), as well as polarized Raman microscopy. These techniques demonstrate for the first time that $(F_5PhO)_2$-F_{16}-SiPc molecules are at a 45-48° orientation to substrate; comparable to other reported R_2-SiPcs. This orientation did not change upon exposure to THC and CBD, which has previously been reported for phthalocyanine-based OTFT cannabinoid sensors. The presence of two bulky axial groups, along with the absence of hydrogens in the molecule and the low reactivity of silicon atom likely causes the lack of interaction with the cannabinoids. While $(F_5PhO)_2$-F_{16}-SiPc may be a successfully air stable *n*-type semiconductor for OTFTs, the changes to the chemical structure to make it air stable over traditional non-fluorinated silicon MPcs are likely responsible for its lack of response to cannabinoid exposure.

4.4 Introduction

Organic thin-film transistors (OTFTs) are an exciting platform for the detection various chemical and biological analytes.[1–5] Low temperature manufacturing and fine tuning of the semiconductor structure enable a wide breadth of highly sensitive and selective sensors. One interesting potential application for OTFT sensors is for the detection and speciation of Δ^9-tetrahydrocannabinol (THC) and cannabidiol (CBD).[6] As cannabis and its products are becoming increasingly legalized and regulated in countries

around the world, it has become necessary to quickly and accurately predict cannabinoid content in a variety of source samples.[7] Previously, our group has demonstrated that OTFT sensors, using metal phthalocyanines (MPcs) as the semiconductor, can effectively detect and differentiate THC and CBD in both solution and vapor samples.[6,8–11] THC and CBD interact with the inner nitrogen ring and central metal of the MPc molecule,[11] leading to unique recrystallization and film reorganization that drives the changes in device performance.[8,11] The choice of peripheral functional groups or metal inclusion within the macrocycle of the MPc has a significant effect on this recrystallization and the sensor response.[8,9,11,12] When using trivalent MPcs such as aluminum Pc (R-AlPc),[8,10] the axial group can be optimized to enhance film interactions and the response to cannabinoids.[12] In most cases, the use of divalent and trivalent MPcs as the semiconductor leads to p-type OTFT operation and hole transporting sensors, which results in a turn-off response upon exposure to cannabinoids. Silicon phthalocyanines (R_2-SiPcs), are tetravalent MPcs that have demonstrated *n*-type behavior, with good electron mobilities and operation in OTFTs[13–17] and organic photovoltaics (OPVs).[18–22] Our group has reported extensively on the fabrication of OTFTs using R_2-SiPcs, with studies focused on contact engineering[23], dielectric interface engineering[14,24,25], thin film processing[14–16,26], axial group functionalization,[16,17,24,27–29] and more.[30–33] To date, R_2-SiPcs have never been reported as the semiconductor in OTFT based cannabinoid sensors due to their poor air stability. Recently, we reported the air stable OTFT operation of fluorinated R_2-SiPcs due to the increased electron withdrawing nature of the fluorine groups, deepening the LUMO level and increasing its air stability.[13,21,27] Bis(pentafluorophenoxy) hexadecafluoro silicon (IV) phthalocyanine ($(F_5PhO)_2$-F_{16}-SiPc)[13] has demonstrated good air-stable *n*-type performance in OTFTs and is a promising candidate for further development.

In this study, we explore the use of $(F_5PhO)_2$-F_{16}-SiPc as the semiconductor in OTFT based cannabinoid sensors. The OTFT sensors did not respond to the presence of CBD or THC. Upon study of the thin films, including novel characterization of these materials, we demonstrate the surprising lack of change with exposure to cannabinoids.

4.5 Results and Discussion

4.5.1 Transistor Characterization

Bottom-gate bottom-contact (BGBC) devices were fabricated with a thermally

evaporated 50 nm layer of $(F_5PhO)_2$-F_{16}-SiPc as the semiconductor on octyltrichlorosilane (OTS)-functionalized SiO_2 as the dielectric with Au electrodes (W = 10 mm, L = 10 μm) (**Figure 4.1a**). F_2-F_{16}-SiPc was synthesized according to a previously reported literature procedure,[27] and the axial functionalization to obtain $(F_5PhO)_2$-F_{16}-SiPc was adapted from an original reaction by Vebber et al.[13] The output and transfer curves from a representative device tested in air are shown in **Figure 4.1b** and **4.1c**. The average electron mobility (μ_e) was 0.04 ± 0.01 cm^2/Vs, with a threshold voltage (V_T) of 9.9 V and a median on-current (I_{On}) of 0.32 mA, from a minimum of 20 transistors. These results surpass our previously recorded performance for $(F_5PhO)_2$-F_{16}-SiPc in air (**Table 4.1**), which were obtained in a bottom-gate top-contact (BGTC) architecture using Ag electrodes (W = 1 mm, L = 30 μm).[13] The improved performance is likely due to the improved electrode architecture and electrode material. While BGBC architectures are generally associated with higher contact resistance and reduced performance, the increased W/L would lead to an increased overall channel surface area, improving μ_e and I_{On}, as charge could move through the channel more quickly.

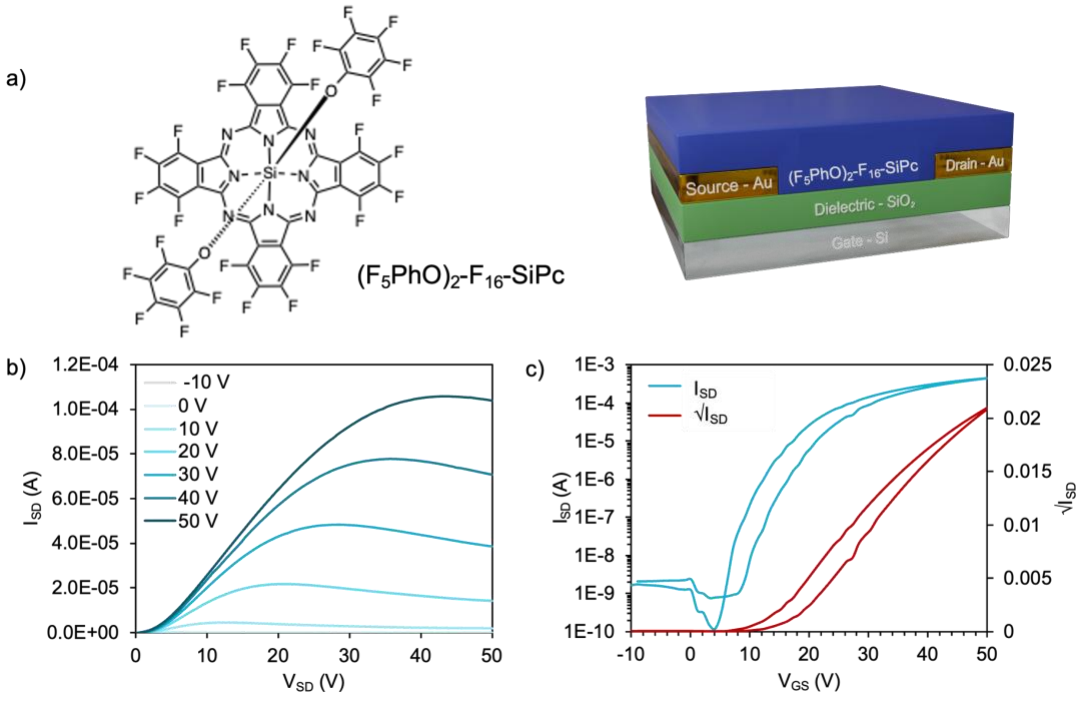

Figure 4.1. *(a) $(F_5PhO)_2$-F_{16}-SiPc chemical structure, and the bottom-gate bottom-contact (BGBC) device architecture used in this study, along with the associated (b) output curves and (c) transfer curves (V_{SD} = 50 V) of the $(F_5PhO)_2$-F_{16}-SiPc OTFTs tested in air.*

Table 4.1. *Comparison of in-air performance of $(F_5PhO)_2$-F_{16}-SiPc detailed in this work (BGBC, Au electrodes) with previously reported performance (BGTC, Ag electrodes).*

	This Work	Previous Work[13]
μ_e (cm^2/Vs)[a]	$(3.8 \pm 1.0) \times 10^{-2}$	$(8.1 \pm 0.3) \times 10^{-3}$
V_T (V)[a]	9.9 ± 1.9	10.1 ± 4.1
$I_{On/Off}$	10^4 - 10^5	10^3 - 10^4
I_{On} (A)[b]	3.16×10^{-4}	4.91×10^{-6}

[a] μ_e and V_T calculated from an average of a minimum of 20 devices; [b] I_{On} taken from the median.

The resulting $(F_5PhO)_2$-F_{16}-SiPc OTFTs were exposed to THC and CBD vapor (**Figure 4.3**, **Supporting Information**). A substrate was also left out in air for the time taken to expose and test the other devices to compare any changes in performance to those experienced by air exposure (control). As shown in **Figure 4.3** (**Supporting Information**), negligible changes in transfer characteristics were observed, where changes in μ_e and V_T were within statistical error of the controls. Unlike when using fluorinated copper MPc (F_{16}-CuPc)[6], another *n*-type semiconductor, the V_T did not reliably decrease for both cannabinoids, which would be indicative of a turn-on response. However, the μ_e was found to decrease as it had for F_{16}-CuPc, though not significantly more than what was experienced by the control. Interestingly, the defect density, *N*, for the exposed samples was shown to increase in relation to the air-only sample, indicating that exposure to cannabinoids potentially introduces additional charge traps to the film, which may help explain the slightly reduced μ_e. Regardless, we could not conclusively detect the cannabinoids using $(F_5PhO)_2$-F_{16}-SiPc OTFTs.

4.5.2 Thin-film Characterization

Typically, MPc films experience significant changes in morphology when exposed to cannabinoid vapors or solutions.[8–10,12] Therefore, $(F_5PhO)_2$-F_{16}-SiPc films were characterized using various synchrotron based techniques, for the first time, to investigate if any morphological or orientational changes would occur upon exposure to cannabinoids.

Angle-dependent near-edge X-ray absorption fine structure (NEXAFS) was performed at the carbon K-edge (280-310 eV) using monochromatic synchrotron X-ray beam polarized to linear horizontal (LH), where a 50 nm film of $(F_5PhO)_2$-F_{16}-SiPc on a

SiN membrane was rotated between 0° and 60° with respect to the sample surface normal (**Figure 4.2a**). The rotation of the sample causes a change in the relative intensity of peaks in the NEXAFS spectra.[34] By plotting the intensity of the peak associated with the $\pi^*_{C=C}$ bonds in the SiPc macrocycle, we can determine if the majority of the molecules in the film are more face-on or edge-on by determining the dichroic ratio, *R* (**Figure 4.2b, c**).[35–38] In the NEXAFS spectrum of $(F_5PhO)_2$-F_{16}-SiPc there are four major features: (i) a peak at 285.6 eV associated with the 1s to $\pi^*_{C=C}$ transition in unsaturated carbon bonds in the SiPc plane, (ii) a strong peak at 287.8 eV that can be attributed to the highly shifted $\pi^*_{C=C}$ from the fluorinated phenoxy substituents, (iii) a peak at 289 eV that is likely the highly shifted $\pi^*_{C=C}$ from the fluorinated substituents from the SiPc plane, and (iv) the multiple broad peaks above 293 eV associated with the 1s to σ^*_{C-C} transitions.[32] This spectra corresponds closely to that collected for $(F_5PhO)_2$-SiPc, with the addition of the signal at 289 eV for the additional peripheral fluorines.[32] To determine the orientation of the SiPc macrocycle plane to the substrate surface, the intensity of the 285.6 eV signal was plotted against the angle of substrate rotation to generate a linear fit. This intensity increases with increasing angle of rotation, exhibiting dichroic behaviour and allowing the calculation of *R*, determined to be 0.26 (**Equation 4.3**). This indicates a slight preference towards a pseudo edge-on orientation for molecules throughout the film; inclusive of both crystalline and amorphous regions. Edge-on orientation is preferred for OTFT applications, enabling charge transport through the film.

Angle-dependent NEXAFS was also performed on $(F_5PhO)_2$-F_{16}-SiPc films after exposure to THC and CBD (**Figure 4.4**, **Supporting Information**), where the same spectral features were observed, and the intensity of the $\pi^*_{C=C}$ peak increased with increasing substrate rotation. The calculated *R* for the THC and CBD exposed samples was 0.23 and 0.22, respectively, indicating that the molecules remained primarily edge-on after cannabinoid exposure. Previous cannabinoid sensors, such as those fabricated with zinc Pc (ZnPc) and Cl-AlPc and its substituted derivatives, saw success due to their ability to adopt new polymorphs and crystal structures in films after exposure to cannabinoids.[8–10,12] This small change in *R* experienced by $(F_5PhO)_2$-F_{16}-SiPc indicates that this molecule does not undergo this same crystal rearrangement, and may be more stable in its thin film structure than other MPcs.

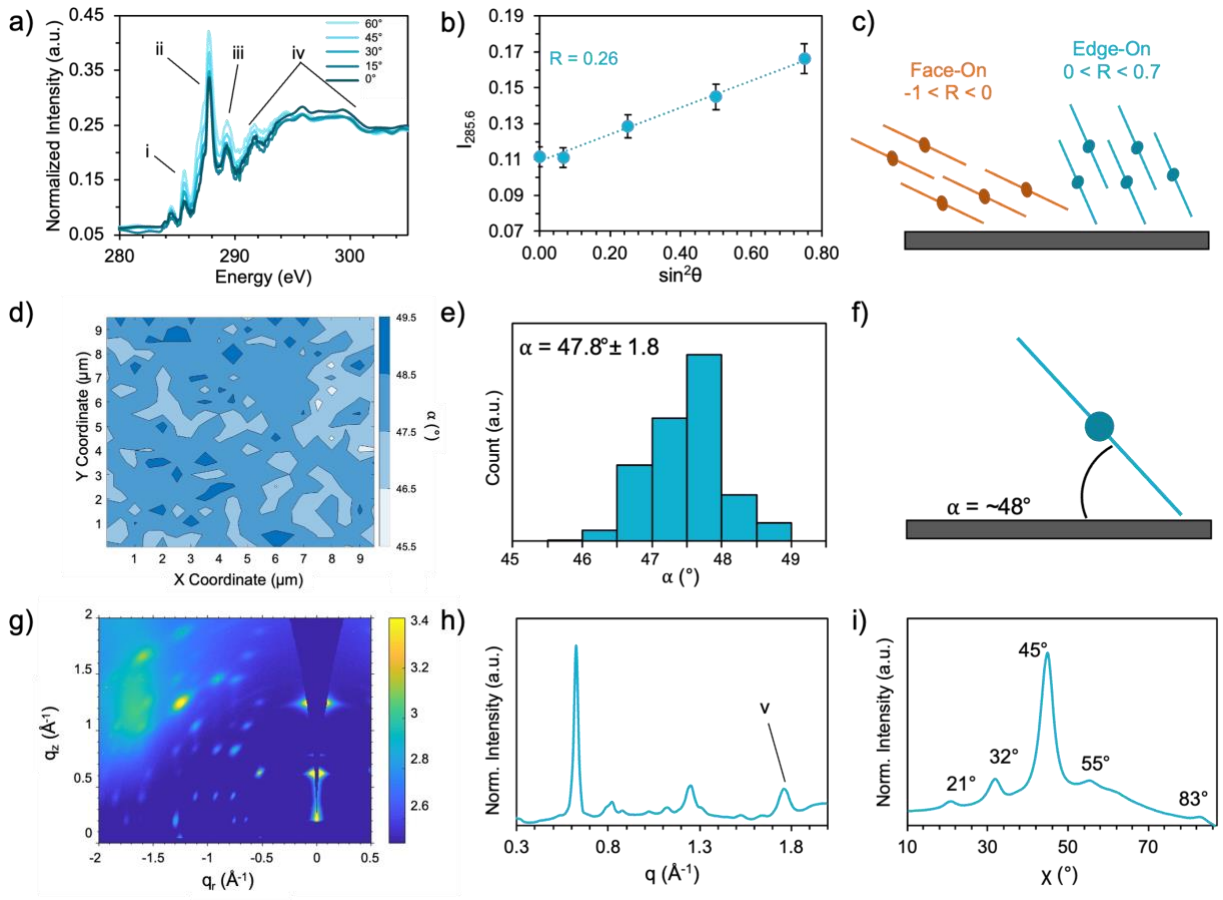

Figure 4.2. *Thin film characterization to elucidate the molecular orientation of $(F_5PhO)_2$-F_{16}-SiPc, including (a) normalized angle-dependent NEXAFS spectra. (b) The intensity of the peak of the $\pi^*_{C=C}$ transition of the SiPc plane was plotted against $\sin^2\theta$ to generate a linear fit, allowing the calculation of the dichroic ratio, R, which indicates tendency towards face-on or edge-on orientation of the molecules to the surface, as shown in (c). (d) Polarized Raman microscopy mapping on a 10 x 10 μm area with a 0.5 μm step size to generate a contour plot of the average $(F_5PhO)_2$-F_{16}-SiPc angle to the surface, with the (e) angle distribution, showing an average angle of 47.8° to the surface, as illustrated in (f). (g) 2D GIWAXS spectra and (h) the corresponding diffraction pattern and (i) linecut profile with respect to χ for a q-range of 1.7-1.9.*

The $(F_5PhO)_2$-F_{16}-SiPc films were also analyzed by polarized Raman microscopy, where Z(XX)Z' and Z(XY)Z' polarized Raman spectra were collected every 0.5 μm over a 10 x 10 μm area over the $(F_5PhO)_2$-F_{16}-SiPc surface. The full baseline Raman spectrum can be found in **Figure 4.7** (**Supporting Information**). As we have previously demonstrated,[26] we can use the ratio of intensities of the isoindole peak of the SiPc (~1555 cm^{-1} in this case) at each polarization to find the average orientation of the SiPc molecule to the surface with **Equation 4.2**.[26,39–43] The results were mapped on a contour plot (**Figure 4.2d**), and the angle distribution plotted (**Figure 4.2e**), showing an average molecular orientation of 47.8° to the surface (**Figure 4.2f**). The distribution of average

angles is tight, ranging from a minimum of 45.5° to a maximum of 49.5°. This is to be expected for a film deposited by physical vapor deposition, and is consistent with previous studies for vapor deposited R_2-SiPcs, where angles between 44° and 52° have been found by Polarized Raman microscopy.[26] This calculated orientation is slightly more edge-on than face-on, supporting the NEXAFS results. Raman maps and angle distribution plots were also generated for the cannabinoid exposed samples (**Figure 4.6**, **Supporting Information**), where the average angles were determined to be within standard deviation from the baseline sample. Again, this supports the NEXAFS results, indicating that $(F_5PhO)_2$-F_{16}-SiPc films did not significantly change upon exposure to cannabinoids.

Grazing-incidence wide-angle X-ray scattering (GIWAXS) is a useful technique to identify the molecular structure and crystallinity of MPc thin films. As seen in **Figure 4.2g**, 2D GIWAXS spectra was obtained for $(F_5PhO)_2$-F_{16}-SiPc, and the corresponding diffraction pattern was generated (**Figure 4.2h**). The resulting pattern has very sharp, spot-like scattering features throughout, indicating a high level of crystallinity with narrow orientation distributions through the film; similar to what has been seen with $(F_5PhO)_2$-SiPc on OTS-treated substrates.[24] The π-π stacking diffraction signal of MPcs attributed to the orientation of the central Pc plane is known to be associated with peaks in the upper *q*-range, around 1.7-2.1.[9,10,16,24,25] Integration of the linecut profile of the GIWAXS spectra in a *q*-range of 1.7-1.9 (**Figure 4.2i**), corresponding with the peak in the diffraction pattern indicated by (v) in **Figure 4.2h**, gives a predominant $(F_5PhO)_2$-F_{16}-SiPc angle of 45° to the substrate, with less intense peaks at 21°, 32°, 55°, and 83° indicating a mixed orientation film. These results agree with those observed by both Raman and NEXAFS, and are similar to those obtained previously for $(F_5PhO)_2$-SiPc on OTS by GIWAXS. Multiple orientations have been observed for other R_2-SiPcs by GIWAXS, depending on their deposition technique and surface treatment,[14,25] but the appearance of the more edge-on orientations of 45°, 55° and 83° is common for high-performing SiPcs like $(F_5PhO)_2$-SiPc, and causes improved horizontal charge transfer through the film, increasing the μ_e.[14,24] GIWAXS is a higher resolution technique than Raman and NEXAFS for identifying specific polymorphs and molecular angles, but it can only identify the orientation of molecules in crystalline regions of thin films that generate a diffraction

pattern (not the amorphous regions), where Raman and NEXAFS identify average orientations.[44] The primary orientation of 45°, while considering the other observed orientations would correlate to a slight preference to edge-on obtained by NEXAFS and Raman.

GIWAXS was also performed on $(F_5PhO)_2$-F_{16}-SiPc films exposed to THC and CBD (**Figure 4.5**, **Supporting Information**), and the same molecular orientations can be observed, with no significant new diffraction pattern indicating the appearance of new polymorphs. As previously mentioned, high performing MPc-based OTFT cannabinoid sensors have experienced significant film reorganization in response to cannabinoids, and this has been observed through changes in orientation by GIWAXS.[9,12] $(F_5PhO)_2$-F_{16}-SiPc did not experience these types of changes in the molecular orientations, or in the relative intensity of these angles, which is consistent with the lack of significant change in device performance upon exposure.

In previous reports we have explored various MPcs as semiconductors in cannabinoid sensors and have found that the central atom plays a significant role in the sensitivity.[8,11] For example, through solution based spectroelectrochemistry and 2D NMR experiments,[11] along with thin film characterization,[8] we have found that ZnPc and R-AlPc result in more sensitive devices.[9,10,12] We have also explored different levels of fluorination in ZnPcs with 0, 4, and 16 peripheral fluorine groups and found that while all were effective sensors, the unfluorinated ZnPc was the most sensitive.[9] In this study, we expand on our previous work by exploring the first use of an R_2-SiPc in these sensors, which is also the first report of a tetravalent MPc used in cannabinoid sensors. We surmise the axial groups above and below the central silicon atom prevent significant interaction with the cannabinoid. As THC and CBD were found to primarily interact with the central ring of nitrogens in MPc molecules, the presence of bulky, inflexible axial groups on both sides of the central SiPc plane likely sterically hinder any potential cannabinoid interaction. Furthermore, the lack of any hydrogen groups could prevent hydrogen bonding interactions, and the fact that silicon is a relatively inert metalloid rather than a reactive metal, might also contribute to the observed reduced interactions. It would appear that the structural changes implemented to make $(F_5PhO)_2$-F_{16}-SiPc a semiconductor for air stable, *n*-type OTFT operation, have also made it resistant to

interactions with cannabinoids, preventing its use as a sensing element.

4.6 Conclusion

We report the application of the air stable *n*-type semiconductor $(F_5PhO)_2$-F_{16}-SiPc in BGBC OTFTs. We explored the corresponding thin films by synchrotron-based GIWAXS and NEXAFS, as well as Polarized Raman microscopy. These complimentary techniques demonstrate for the first time that the $(F_5PhO)_2$-F_{16}-SiPc molecules are at a 45-48° angle from the substrate with relatively homogeneous morphology, which is comparable to the orientations previously found for $(F_5PhO)_2$-SiPc and other SiPcs. We also explored the use of $(F_5PhO)_2$-F_{16}-SiPc based OTFTs as cannabinoid sensors and found no statistical difference in performance before and after exposure to CBD and THC. The film characterization also revealed negligible changes in structure with exposure to cannabinoids which has been reported for high performing MPc OTFT cannabinoid sensors. Overall, $(F_5PhO)_2$-F_{16}-SiPc is among the most air-stable silicon based MPcs used in OTFTs, but the very structural changes that lead to this air stability and high performance are what prevent its use as a cannabinoid sensing molecule.

4.7 Experimental Methods

4.7.1 Materials

Tetrafluorophthalonitrile (97%) and pentafluoro phenol (99%) were purchased from Ambeed. Lithium bis(trimethylsilylamide) (97%) was purchased from Sigma Aldrich and the etherate was prepared as outlined in literature.[45] Silicon tetrachloride (99%), boron trichloride (1 M in heptane), anhydrous tetraline, chlorobenzene and (octyl)trichlorosilane (OTS, 97%) were purchased from Sigma Aldrich and used as received. All solvents used in device fabrication were HPLC grade and purchased from Fisher Scientific. Toronto Research Chemicals supplied the cannabinoid standards.

4.7.2 Chemical Synthesis

Synthesis of Si,Si-difluoro hexadecafluoro silicon(IV) phthalocyanine (F_2-F_{16}-SiPc)

Based from previously reported procedure,[27] tetrafluorophthalonitrile (5.g, 25.0 mmol) was charged in a 500 mL round-bottom flask (RBF) under argon. Anhydrous tetraline (125 mL) was transferred to RBF via canula and mixture was stirred until phthalonitrile was completely dissolved. LiHMDS·Et_2O (3.0 g, 12.4 mmol) was added to

the solution and stirred for 2 h at room temperature. $SiCl_4$ (3.54 ml, 30.0 mmol) was added and the resulting mixture was stirred for 24 h at 200 °C. The mixture was then brought to 50 °C and filtered twice through a coarse porosity fritted funnel. The resulting filter cake was sonicated for 15 min in 200 mL of methanol, refiltered and washed with 150 mL of acetone, then sonicated for 15 min with 150 mL of hexanes and filtered once again. The resulting crude was dried overnight under high vacuum to give the title product as a blue powder (3.17 g), used in subsequent steps without further purification.

Synthesis of Si,Si-dichloro hexadecafluoro silicon(IV) phthalocyanine (Cl_2-F_{16}-SiPc)

Based from previous literature,[27] F_2-F_{16}-SiPc (1.6g, 1.8 mmol) was dissolved in anhydrous chlorobenzene (60 mL) in a 100 mL RBF under argon. BCl_3 (11.0 mmol) was added and the resulting mixture was stirred at 130 °C for 72 h. The mixture was then brought to room temperature and filtered under vacuum to recover the crude title product (1.4 g) as a blue powder, which was used in subsequent steps without further purification.

Synthesis of bis(pentafluorophenoxy) hexadecafluoro silicon(IV) phthalocyanine ($(F_5PhO)_2$-F_{16}-SiPc)

Based from previous literature,[13] Cl_2-F_{16}-SiPc (1.4 g, 1.6 mmol) was dissolved in anhydrous chlorobenzene (60 mL) in a 100 mL RBF under argon. Pentafluoro phenol (1.6g, 8.5 mmol) was added and the resulting mixture was stirred at 130 °C for 72 h. The mixture was then brought to room temperature and filtered under vacuum. The resulting filtrate was concentrated down via rotary evaporation, then sonicated in 50 mL of MeOH and refiltered to recover a dark blue powder as the crude title product (136 mg). The crude product was further purified via train sublimation at 125 mTorr with a temperature of 260 °C using CO_2 as a carrier gas. HR-MS expected mass: 1193.95; obtained mass: 1193.95084

4.7.3 Thin-film Deposition

Fraunhofer IPMS supplied custom prefabricated devices to make BGBC transistors, each consisting of a 230 nm thermally grown SiO_2 dielectric layer on an Si gate, and prepatterned source-drain electrodes with a *W/L* of 1000 (*W* = 10 mm, *L* = 10 μm). Silicon (Si) substrates from WaferPro were used for GIWAXS sample preparation. The substrates were washed with acetone to remove the photoresist, then with isopropanol and dried under a N_2 gas stream. They were then treated with oxygen plasma

for 15 minutes, briefly rinsed with water, isopropanol, and dried with N_2. Once dry, they were immersed in a 1% v/v OTS solution in toluene for 1 hour at 70 °C. The substrates were then rinsed with toluene and isopropanol, dried with N_2, and placed in a vacuum oven at 70 °C for 1 hour to remove trace solvent. The substrates were placed in an Angstrom EvoVac thermal evaporator at a pressure below 2 x 10^{-6} Torr, where $(F_5PhO)_2$-F_{16}-SiPc was deposited by sublimation at 0.2 Å s^{-1} until a thickness of 500 Å was reached.

4.7.4 OTFT Characterization

Transistors were tested using a custom-built auto tester machine and run using a Keithley 2614B SourceMeter and Labview software. The V_{DS} and V_{GS} were set and the I_{SD} was measured to obtain both output and transfer curves. Five transfer curves were taken for each transistor and the final three were averaged. From the transfer curve, the V_T, N and μ_e could be extracted, the latter using Equation 2, for saturation operation.

$$I_{SD} = \frac{\mu C_i W}{2L}(V_{GS} - V_T)^2 \quad (4.1)$$

Once the baseline performance of the $(F_5PhO)_2$-F_{16}-SiPc devices was assessed, transistors were exposed to either THC vapor (300 ppm concentration) or CBD vapor (300 ppm concentration) by vaporizing a pure cannabinoid sample into an 8 L bag using the Vapormed Volcano Medic. The bag was slowly emptied over the devices in a chamber for 90 seconds. New output and transfer curves were then obtained for all exposed devices, allowing for a comparison with the baseline values.

4.7.5 GIWAXS Characterization

Grazing incidence wide angle X-ray scattering (WAXS) data was collected using the Brockhouse X-ray Diffraction and Scattering (BXDS) low energy wiggler beamline (04ID-2)[46]. 04ID-2 employed a Si (111) single side-bounce monochromator crystal to select a photon energy of ~15.1 keV (wavelength = 0.81931 A). The beamline employs a Huber four-circle diffractometer end-station which was used to select grazing incidence angles of 0.1 and 0.3 degrees. The sample position was oriented using an automated, iterative procedure to scan the sample height and incidence (theta) angle. WAXS data was collected on a Rayonix MX300 CCD detector using a detector distance of ~474 mm to obtain a Q value of 2. The sample-detector distance and tilt were calibrated using a silver behenate reference material. Samples and reference materials were collected with

acquisition times ranging from 0.1 to 30 s. Silver beheanate (AgBeh) standards were used to calibrate the data, and the data was analyzed using the GIXSGUI software package in MatLab.

4.7.6 Polarized Raman Microscopy and Angle Mapping

Thin films of $(F_5PhO)_2$-F_{16}-SiPc were characterized by polarized Raman microscopy (Z(X,X)Z' and Z(X,Y)Z') on a Renishaw inVia InSpec confocal microscope, which uses a Leica Microsystems bright field microscope with a DM2700 light source. A 500 mW 532 nm laser with a 2400 l/mm grating was used to collect spectra between 550 cm^{-1} and 1700 cm^{-1} at 5% laser power (25 mW) and an exposure time of 2 sec. Individual spectra were taken every 0.5 μm over a 10 x 10 μm area at X50L microscope magnification at both polarizations for a total of 441 spectra per polarization. With the objective and laser combination used, the Raman microscope has a spectral resolution of 0.3 cm^{-1} (FWHM), a theoretical spatial resolution of 640 nm, and a theoretical depth of focus of 3.0 um. Calibration was performed prior to all measurements against the 520 cm^{-1} silicon reference peak within 0.5 cm^{-1}. The intensity of the Raman peak at 1555 cm^{-1}, the B_{1g} pyrrole stretch, was obtained by WiRE 5.6 inVia software for both polarizations (I_{XX} and I_{XY}) was used to calculate the angle of the planar $(F_5PhO)_2$-F_{16}-SiPc core using Equation 2 (CITE Rose's paper).[39–43] The resulting angles were then mapped on a contour plot using MatLab software.

$$\frac{I_{XX}}{I_{XY}} = 2\cot^2\alpha \tag{4.2}$$

A baseline Raman spectrum was also collected for THC and CBD alone, and is shown in **Figure S4.5** (Supporting Information).

4.7.7 Near-edge X-ray Absorption Fine Structure (NEXAFS)

Samples for near edge X-ray absorption fine structure (NEXAFS) were prepared on custom substrates purchased from NORCADA Inc with two transparent silicon nitride (SiN) membranes (0.10 mm x 0.25 mm, thickness = 50 nm) on a Si frame. The membranes were treated with oxygen plasma and OTS following the same procedure as transistor substrate preparation, followed by the deposition of 50 nm of $(F_5PhO)_2$-F_{16}-SiPc, taking care to not damage the delicate membrane. After removal from the evaporator, the membranes were inspected for damage under a bright field microscope

before NEXAFS characterization.

NEXAFS experiments were conducted using a Research Instruments scanning transmission x-ray microscopy (STXM) apparatus, provided by RI Research Instruments GmbH, Germany, at the HERMES beamline (73)[47] at the synchrotron SOLEIL facility. A Fresnel Zone Plate with a 25 nm outer zone radius was used to focus a monochromatic X-ray beam onto the sample. The sample was attached to a stage capable of raster scanning and polar angle rotation. A Photomultiplier Tube (PMT) was used to detect the transmitted X-rays. Polarization switching was facilitated by automated adjustments of the undulators, all the while preserving beam alignment and flux. Throughout all measurements, the microscope chamber was held under vacuum at a pressure of 10^{-4} mbar. Energy data sets comprised of line scans were acquired at the carbon K-edge, from 280 to 310 eV. For each line scan a region of 5 µm length was scanned with step size of 250 nm and a dwell time of 100. The lines scans were repeated at various X-ray incident angles (θ) of 0°, 15°, 30°, 45°, and 60° with respect to the sample surface normal. The set up and rotation of sample has been detailed previously by our group.[48]

The dichroic ratio, R, was calculated using Equation 3, which is an indication of orientation tendency. I(90°) is determined using the linear fit from the plot of the intensity of the $\pi^*_{C=C}$ signal ($I_{285.6}$) against $\sin^2\theta$.

$$R = \frac{I(90°) - I(0°)}{I(90°) + I(0°)} \quad (4.3)$$

Energy calibration was accomplished using the well-resolved 3p Rydberg peak at 294.96 eV of gaseous CO_2.[49] Data was processed using the aXis2000 software (accessible at http://unicorn.chemistry.mcmaster.ca/aXis2000.html) suite. Raw individual energy images were transformed into optical density (OD) images, utilizing the reference intensity (I_0) from an uncoated silicon nitride (SiN) membrane sample. To ensure accurate alignment, energy stacks were aligned following the Jacobsen method.

4.8 Acknowledgments

This work was supported by NSERC Discovery grant RGPIN 2015-05796 (A.J.S.), 2015-05453 (C.S.H.), and 2020-04079 (B.H.L.), the Canada Research Chairs Program 950-230754 (A.J.S.) and 950-230724 (B.H.L.). Student support was acquired through NSERC PGS-D (H.L) and CGS-D (M.C). GIWAXS was performed at the Canadian Light

Source, a national research facility of the University of Saskatchewan, which is supported by the Canada Foundation for Innovation (CFI), the Natural Sciences and Engineering Research Council (NSERC), the National Research Council (NRC), the Canadian Institutes of Health Research (CIHR), the Government of Saskatchewan, and the University of Saskatchewan. The authors would also like to thank Synchrotron SOLEIL for providing beamtime at the HERMES beamline for the NEXAFS characterization.

4.9 Supporting Information

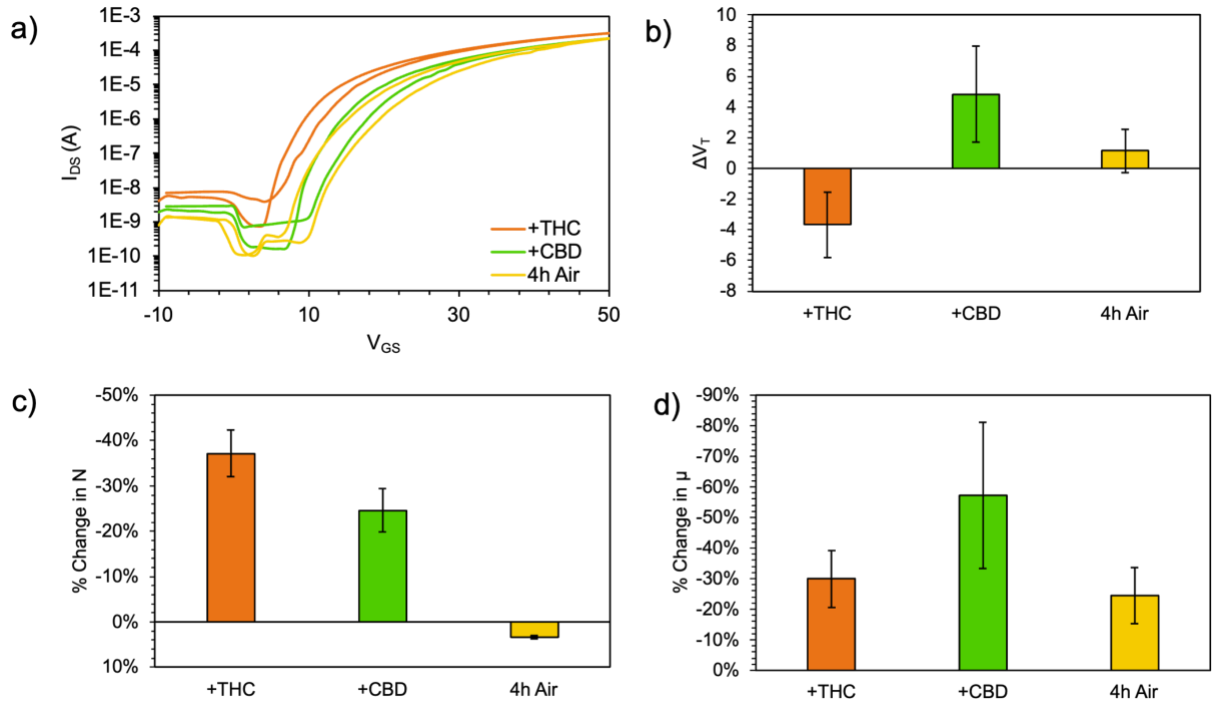

Figure 4.3. *($F_5PhO)_2$-F_{16}-SiPc performance after exposure to THC and CBD, demonstrated by the (a) transfer curve (V_{SD} = 50 V) of a representative device, (b) average change in threshold voltage, V_T, (c) average change in defect density, N, and (d) the average change in electron mobility, μ_e. All averages are for a minimum of 10 transistors.*

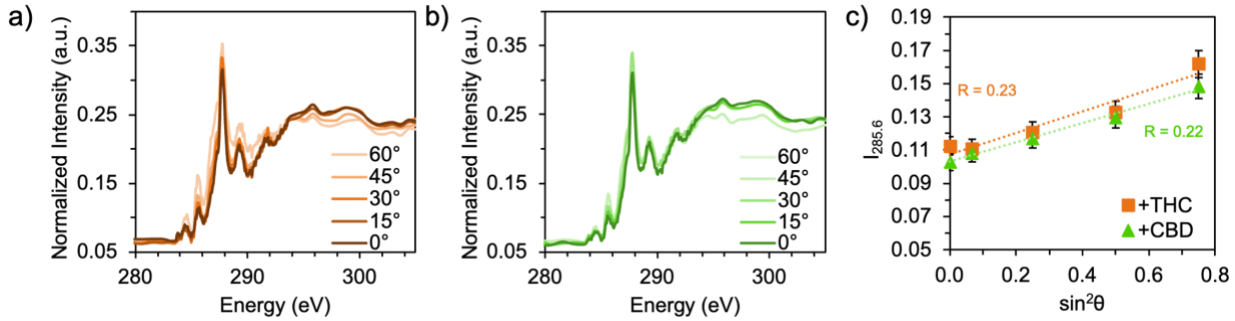

Figure 4.4. *Angle-dependent near-edge X-ray absorption fine structure (NEXAFS) spectroscopy of $(F_5PhO)_2$-F_{16}-SiPc thin films after exposure to (a) THC and (b) CBD, with the intensity of the 285.6 eV peak plotted against $\sin^2\theta$ to generate a linear fit, with the corresponding calculated dichroic ratio, R.*

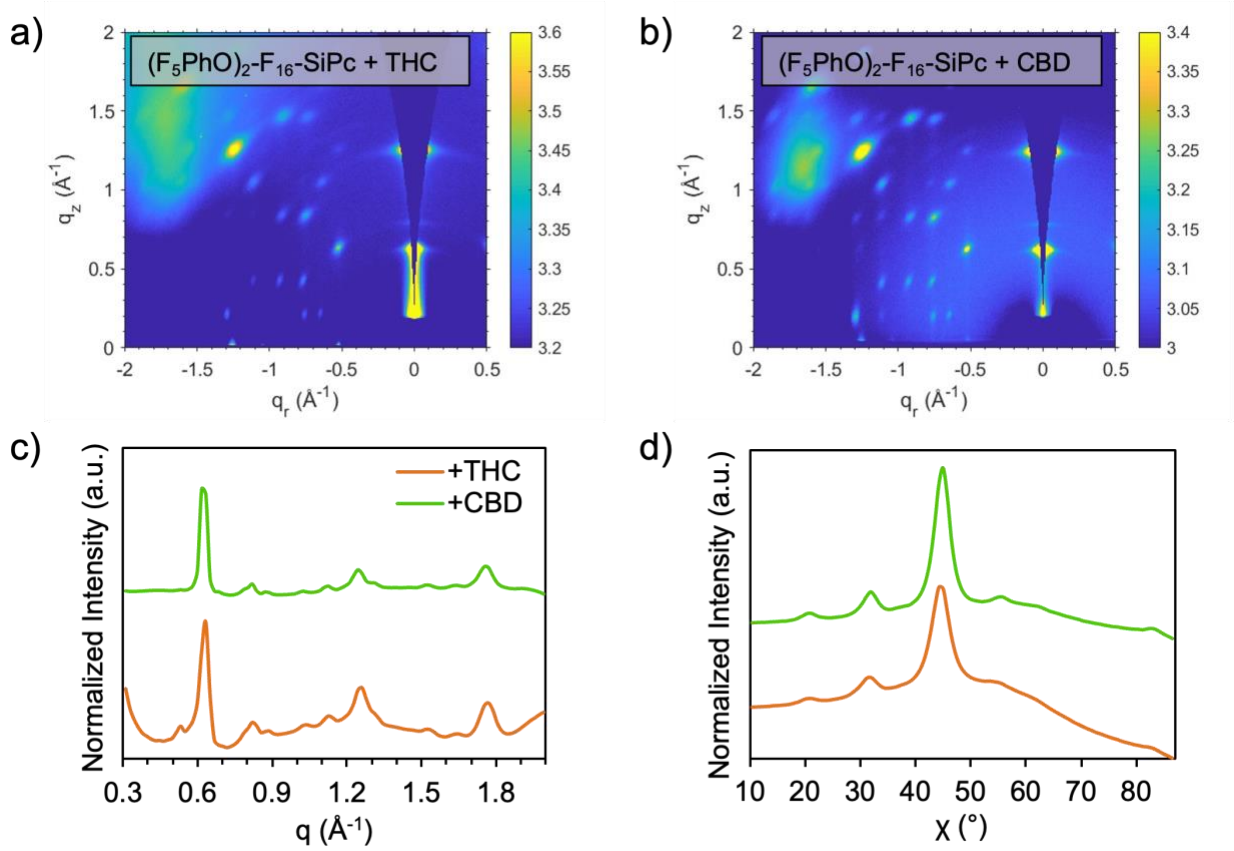

Figure 4.5. *2D Grazing-incidence wide-angle X-ray scattering (GIWAXS) of $(F_5PhO)_2$-F_{16}-SiPc thin films on Si substrates after exposure to (a) THC and (b) CBD, with (c) the corresponding diffraction patterns and (d) linecut profiles with respect to χ for a q-range of 1.7-1.9.*

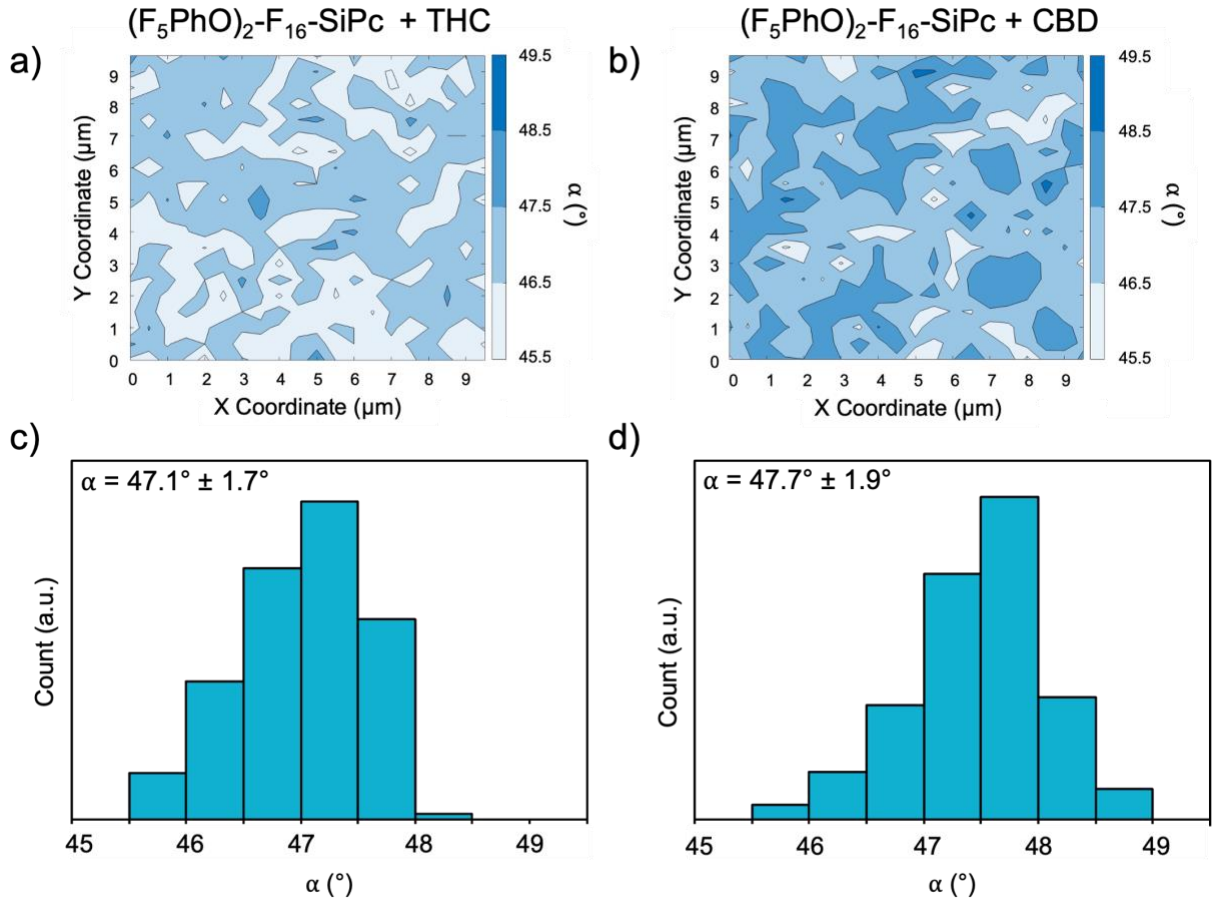

Figure 4.6. *Raman microscopy maps and angle distribution graphs of $(F_5PhO)_2$-F_{16}-SiPc after exposure to (a,c) THC and (b,d) CBD.*

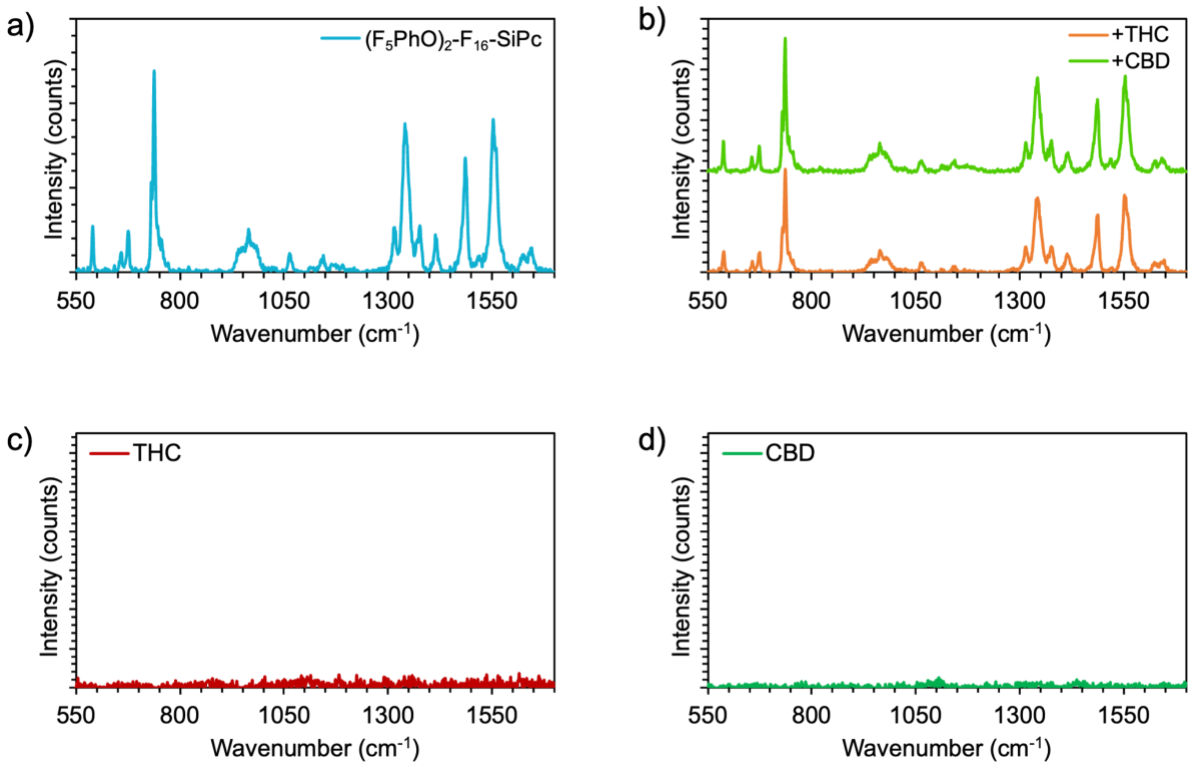

Figure 4.7. *Raman spectra of (a) $(F_5PhO)_2$-F_{16}-SiPc and (b) $(F_5PhO)_2$-F_{16}-SiPc after exposure to THC and CBD. The baseline spectra of (c) THC and (d) CBD are included.*

4.10 References

[1] B. King, B. H. Lessard, *J. Mater. Chem. C* **2024**, DOI 10.1039/D3TC03611A.
[2] P. Lin, F. Yan, P. Lin, F. Yan, *Adv. Mater.* **2012**, *24*, 34.
[3] J.-H. Kwon, M.-H. Kim, J.-H. Bae, *J. Mater. Chem. C* **2023**, *12*, 29.
[4] C. Sun, T. Wang, *Nano Res.* **2024**, *17*, 426.
[5] M. Wu, S. Hou, X. Yu, J. Yu, *J. Mater. Chem. C* **2020**, *8*, 13482.
[6] Z. J. Comeau, N. T. Boileau, T. Lee, O. A. Melville, N. A. Rice, Y. Troung, C. S. Harris, B. H. Lessard, A. J. Shuhendler, *ACS Sens.* **2019**, *4*, 2706.
[7] A. DI, *Eur. J. Intern. Med.* **2018**, *49*, 7.
[8] Z. J. Comeau, N. A. Rice, C. S. Harris, A. J. Shuhendler, B. H. Lessard, *Adv. Funct. Mater.* **2022**, *32*, 2107138.
[9] Z. J. Comeau, R. R. Cranston, H. R. Lamontagne, C. S. Harris, A. J. Shuhendler, B. H. Lessard, *Commun Chem* **2022**, *5*, 1.
[10] H. R. Lamontagne, Z. J. Comeau, R. R. Cranston, N. T. Boileau, C. S. Harris, A. J. Shuhendler, B. H. Lessard, *Sens. Diagn.* **2022**, *1*, 1165.
[11] Z. J. Comeau, G. A. Facey, C. S. Harris, A. J. Shuhendler, B. H. Lessard, *ACS Appl. Mater. Interfaces* **2020**, *12*, 50692.
[12] H. R. Lamontagne, R. R. Cranston, Z. J. Comeau, C. S. Harris, A. J. Shuhendler, B. H. Lessard, *Adv. Sci.* **2024**, *11*, 2305515.
[13] B. King, M. C. Vebber, R. Ewenike, M. Dupuy, C. French, J. L. Brusso, B. H. Lessard, *Chem. Mater.* **2023**, *35*, 8517.
[14] R. R. Cranston, M. C. Vebber, J. F. Berbigier, N. A. Rice, C. Tonnelé, Z. J. Comeau, N. T. Boileau, J. L. Brusso, A. J. Shuhendler, F. Castet, L. Muccioli, T. L. Kelly, B. H. Lessard, *ACS Appl Mater Interfaces* **2021**, *13*, 1008.
[15] R. R. Cranston, B. King, C. Dindault, T. M. Grant, N. A. Rice, C. Tonnelé, L. Muccioli, F. Castet, S. Swaraj, B. H. Lessard, *J. Mater. Chem. C* **2022**, *10*, 485.
[16] R. R. Cranston, M. C. Vebber, J. Faleiro Berbigier, J. Brusso, T. L. Kelly, B. H. Lessard, *Adv. Electron. Mater.* **2022**, *8*, 2200696.
[17] B. King, A. J. Daszczynski, N. A. Rice, A. J. Peltekoff, N. J. Yutronkie, B. H. Lessard, J. L. Brusso, *ACS Appl. Electron. Mater.* **2021**, *3*, 2212.
[18] M.-T. Dang, T. M. Grant, H. Yan, D. S. Seferos, B. H. Lessard, T. P. Bender, *J. Mater. Chem. A* **2017**, *5*, 12168.
[19] T. M. Grant, D. S. Josey, K. L. Sampson, T. Mudigonda, T. P. Bender, B. H. Lessard, *Chem. Rec.* **2019**, *19*, 1093.
[20] B. H. Lessard, *ACS Appl Mater Interfaces* **2021**, *13*, 31321.
[21] B. H. Lessard, T. M. Grant, R. White, E. Thibau, Z.-H. Lu, T. P. Bender, *J. Mater. Chem. A* **2015**, *3*, 24512.
[22] M. C. Vebber, N. A. Rice, J. L. Brusso, B. H. Lessard, *ACS Appl. Energy Mater.* **2022**, *5*, 3426.
[23] O. A. Melville, T. M. Grant, K. Lochhead, B. King, R. Ambrose, N. A. Rice, N. T. Boileau, A. J. Peltekoff, M. Tousignant, I. G. Hill, B. H. Lessard, *ACS Appl. Electron. Mater.* **2020**, *2*, 1313.
[24] B. King, C. L. Radford, M. C. Vebber, B. Ronnasi, B. H. Lessard, *ACS Appl. Mater. Interfaces* **2023**, *15*, 14937.
[25] R. B. Ewenike, B. King, A. M. Battaglia, J. D. Quezada Borja, Z. S. Lin, J. G. Manion, J. L. Brusso, T. L. Kelly, D. S. Seferos, B. H. Lessard, *ACS Appl. Electron. Mater.*

2023, *5*, 7023.
[26] R. R. Cranston, T. D. Lanosky, R. Ewenike, S. Mckillop, B. King, B. H. Lessard, *Small Sci.* **2024**, *n/a*, 2300350.
[27] M. C. Vebber, B. King, C. French, M. Tousignant, B. Ronnasi, C. Dindault, G. Wantz, L. Hirsch, J. Brusso, B. H. Lessard, *Can J Chem Eng.* **2023**, *101*, 3019.
[28] N. J. Yutronkie, B. King, O. A. Melville, B. H. Lessard, J. L. Brusso, *J. Mater. Chem. C* **2021**, *9*, 10119.
[29] B. King, O. A. Melville, N. A. Rice, S. Kashani, C. Tonnelé, H. Raboui, S. Swaraj, T. M. Grant, T. McAfee, T. P. Bender, H. Ade, F. Castet, L. Muccioli, B. H. Lessard, *ACS Appl. Electron. Mater.* **2021**, *3*, 325.
[30] R. R. Cranston, M. C. Vebber, N. A. Rice, C. Tonnelé, F. Castet, L. Muccioli, J. L. Brusso, B. H. Lessard, *ACS Appl. Electron. Mater.* **2021**, *3*, 1873.
[31] S. Ganesh Moorthy, B. King, A. Kumar, E. Lesniewska, B. H. Lessard, M. Bouvet, *Adv. Sensor Res.* **2023**, *2*, 2200030.
[32] C. Dindault, B. King, P. Williams, J. H. Absi, M. D. M. Faure, S. Swaraj, B. H. Lessard, *Chem. Mater.* **2022**, *34*, 4496.
[33] B. King, S. G. Moorthy, E. Lesniewska, R. Meunier-Prest, M. Bouvet, B. H. Lessard, *Sensors and Actuators B: Chemical* **2024**, *408*, 135507.
[34] A. Salleo, R. J. Kline, D. M. DeLongchamp, M. L. Chabinyc, *Adv. Mater.* **2010**, *22*, 3812.
[35] D. DeLongchamp, E. Lin, D. Fischer, in *Proc. SPIE 5940, Organic Field-Effect Transistors IV, 59400A*, San Diego, California, United States, **n.d.**
[36] T. Schuettfort, L. Thomsen, C. R. McNeill, *J. Am. Chem. Soc.* **2013**, *135*, 1092.
[37] M. G. Samant, J. Stöhr, H. R. Brown, T. P. Russell, J. M. Sands, S. K. Kumar, *Macromolecules* **1996**, *29*, 8334.
[38] J. Stöhr, M. G. Samant, J. Lüning, A. C. Callegari, P. Chaudhari, J. P. Doyle, J. A. Lacey, S. A. Lien, S. Purushothaman, J. L. Speidell, *Science* **2001**, *292*, 2299.
[39] M. Szybowicz, J. Makowiecki, *J Mater Sci* **2012**, *47*, 1522.
[40] M. Szybowicz, W. Bała, K. Fabisiak, K. Paprocki, M. Drozdowski, *J Mater Sci* **2011**, *46*, 6589.
[41] M. Szybowicz, W. Bała, K. Fabisiak, K. Paprocki, M. Drozdowski, *Cryst. Res. Technol.* **2010**, *45*, 1265.
[42] M. Szybowicz, W. Bała, S. Dümecke, K. Fabisiak, K. Paprocki, M. Drozdowski, *Thin Solid Films* **2011**, *520*, 623.
[43] M. Szybowicz, T. Runka, M. Drozdowski, W. Bała, A. Grodzicki, P. Piszczek, A. Bratkowski, *J. Mol. Struct.* **2004**, *704*, 107.
[44] J. Rivnay, S. C. B. Mannsfeld, C. E. Miller, A. Salleo, M. F. Toney, *Chem. Rev.* **2012**, *112*, 5488.
[45] R. T. Boeré, R. T. Oakley, R. W. Reed, *J. Organomet. Chem.* **1987**, *331*, 161.
[46] A. F. G. Leontowich, A. Gomez, B. Diaz Moreno, D. Muir, D. Spasyuk, G. King, J. W. Reid, C.-Y. Kim, S. Kycia, *J Synchrotron Rad* **2021**, *28*, 961.
[47] R. Belkhou, S. Stanescu, S. Swaraj, A. Besson, M. Ledoux, M. Hajlaoui, D. Dalle, *J Synchrotron Rad* **2015**, *22*, 968.
[48] B. Ronnasi, B. King, S. Brixi, S. Swaraj, J. Niskanen, B. H. Lessard, *Adv. Electron. Mater.* **2024**, 2300810.
[49] Y. Ma, C. T. Chen, G. Meigs, K. Randall, F. Sette, *Phys. Rev. A* **1991**, *44*, 1848.

Chapter 5: Conclusions and Future Work

5.1 Summary of Conclusions

Previous work has demonstrated that phthalocyanine-based OTFTs are a promising platform for high-sensitivity cannabinoid detection,[1–4] but factors involved in device fabrication and material design were not fully explored. This thesis aimed to address gaps in our understanding of how device architecture, film structure, and material properties can influence cannabinoid sensor performance and response to assess the viability of these devices, determine optimized conditions for sensor fabrication, and to inform decisions in the development of future sensor applications.

In **Chapter 2** of this thesis, I investigated the interactions between Cl-AlPc and THC or CBD in a thin-film, and how factors like channel surface area, and film roughness and thickness influenced sensor response. This work demonstrated that the conditions for optimal device performance are not necessarily associated with improved sensor response. Increased film roughness and decreased film thickness showed a reduced baseline device performance, but an improved response to cannabinoids. The quality of charge transport pathways available influenced the sensing response, where 30 nm films with higher grain ordering, but a rougher overall film, had the greatest response to cannabinoids. This highlights the importance of optimizing film thickness and deposition conditions during sensor fabrication to increase the exposed surface area of the film. This study also validated a new channel architecture design with a large overall channel surface area, and our automated device testing setup for use in BGBC OTFT sensor platforms.

In **Chapter 3** of this thesis, I utilized simple phenoxylation reactions to substitute the axial chlorine of Cl-AlPc with bulkier phenol groups to improve the response of R-AlPc OTFTs to cannabinoids. These reactions were successful and produced functional OTFTs with marginally lower baseline performance to Cl-AlPc. However, many of these phenoxy-AlPc films exhibited stronger responses to cannabinoid solution and vapor samples than Cl-AlPc, which aligns with the findings of **Chapter 2**. The improved sensor response, investigated by AFM, GIWAXS, and XRD, can be attributed to the mixed crystal arrangement of the thin films, which were generally rougher, showed signs of multiple

polymorphs, and experienced greater rearrangement upon cannabinoid exposure compared to Cl-AlPc. Raman characterization also indicated a change in the isoindole ring environment of the phenoxy-AlPcs after cannabinoid exposure that was not observed with Cl-AlPc. These findings suggest that the axial phenoxylations introduced new thin film motifs that improved MPc-cannabinoid interactions on the film surface that led to the improved sensing response I observed. This illustrates the usefulness of simple substitution reactions to tune the response of MPc-based sensors, and is a strategy that can be readily utilized in similar material families and in other MPc-based sensor applications.

Chapter 4 of this thesis builds on the work in **Chapter 3**, utilizing simple substitution reactions to tune the material properties of MPcs in sensor applications. In this work, I used the air stable *n*-type $(F_5PhO)_2$-F_{16}-SiPc in our cannabinoid sensor platform, where it proved unsuccessful as a sensing molecule, showing no change in electrical performance after cannabinoid exposure. This confirmed the importance of the reactivity of the metal in the cannabinoid sensing response of MPcs, as silicon is a relatively unreactive metal compared to other metal centres used in previous cannabinoid sensing work. Additionally, this validated the integral role the hydrogens in the isoindole ring of MPcs play in the interaction with cannabinoids in a thin film. I characterized these films by GIWAXS, and in the absence of single crystal diffraction data, confirmed these findings by Raman and NEXAFS. I determined that the $(F_5PhO)_2$-F_{16}-SiPc films are highly crystalline and the main plane is oriented slightly edge-on, which promotes efficient charge transport. The highly crystalline nature of the film, while ideal for high device performance and stability, likely contributes to its weak sensing response. As demonstrated in both **Chapters 2** and **3**, more amorphous, mixed orientation films were found to be more successful sensors.

In **Chapter 5** of this thesis, I demonstrated my contributions to various OTFT projects within our group, helping to expand our group's understanding of x-ray characterization of small molecule and polymer thin films, physical vapour deposition of various materials, and the integration of these materials into new sensor platforms. My work contributed to the development of a new technique for the direct measurement of film density, which has the potential to impact multiple adjacent fields beyond organic

electronics, and improve the modelling and prediction of physical properties of thin films. My expertise in film fabrication and characterization has improved our understanding of the effect of surface treatment and thermal annealing on the crystal structure of F_{10}-SiPc, POtbc, and $^{iso}(Si_3O)_2$SiPc films, among others, and its subsequent effect on OTFT performance. These findings can be extrapolated to similar materials, and the knowledge gained from these studies can be utilized in the integration of other new small molecules into OTFTs. As the field of OTFTs and OTFT-based sensors continues to advance towards commercialization, generalized knowledge of material behaviour and optimization strategies for new material integration is vital, and the work I have demonstrated in this thesis has contributed to this basis of knowledge.

5.2 Recommendations for Future Work

Since the initial development of OTFTs as a functioning device platform,[5] the field has come a long way; significant strides have been made in improving the electrical performance of the materials used in each layer, and in improving their environmental stability. However, the commercialization of OTFTs to user-facing sensors continues to be an uphill battle. Persistent issues with the operational and environmental instability of many synthetically accessible materials, high operational voltages, and inconsistent performances currently make OTFTs a suboptimal platform for most applications. Ultimately, OTFTs are currently more suited to highly niche applications, where material tunability and biocompatibility are assets over inorganic counterparts. With the rise of OECTs, which are better suited for liquid-based sensing and bio-facing applications, OTFTs are potentially positioned to break through as highly sensitive gas or vapor sensors, for which there is an economic incentive to deal with the previously mentioned issues. As the field works to solve these issues, OTFTs are a useful platform to study and advance our understanding of material and thin film properties of semiconductors that may be used in other device architectures or platforms. Additionally, expanding our library of semiconducting materials and our understanding of their structure-property relationships, and the influence of various fabrication parameters on device and sensor performance is integral to commercialization efforts.

In the lens of my thesis work, MPcs remain a viable material for future commercial OTFTs due to their inexpensive synthesis and tunable material properties that allow for

both solution and vapor deposition, and their biological and environmental compatibility.[6,7] In order to advance the integration of these materials in sensor applications and improve their performance, I see three potential avenues worthy of exploration. Firstly, further investigation into the dynamics of the sensing mechanism through *in situ* GIWAXS characterization during cannabinoid vapor exposure would help to determine the kinetics of the sensing mechanism. Secondly, the integration of polymer dielectrics into MPc-based OTFT sensors could help achieve lower operational voltages. Finally, the strategy of axial phenoxylation could be further exploited to add reactive groups to the MPc, which could improve analyte-MPc interactions on the film surface. Each of these ideas builds on the work explored in this thesis, some of which I had begun to explore at various points during my graduate studies and would present opportunities for future graduate students in our research group or others to advance.

5.2.1 *In situ* cannabinoid vapor exposure of MPc films with simultaneous X-ray characterization

As demonstrated by numerous publications in the field of perovskite solar cells, *in situ* GIWAXS experiments can be run while spin-coating perovskite solutions to elucidate the kinetics of crystallite formation during these dynamic processes.[8–11] The ability to run GIWAXS scans while solutions are being applied to a surface enables the application of this technique to the addition of analyte solutions to film surfaces, or exposure of analyte vapors/gases over time. We could specifically apply this to our cannabinoid sensor platform and expose MPc films to cannabinoid solutions or vapor to clarify the kinetics of the sensing response as the analyte is introduced to the film. In previous work, we have seen that there is a reversible and irreversible component to cannabinoid vapor sensing, where part of the initial performance is recovered after removal of cannabinoid vapor from the testing environment, but some performance reduction is permanent.[3] It would be worthwhile to understand if any crystallization or changes in the film structure occur during this reversible sensing response. Additionally, from a sensor workflow development context, it would be extremely useful to understand how long the irreversible recrystallization takes to occur, and the dose of cannabinoid required to cause this change.

The challenges of exposing thin film samples to cannabinoid vapor in a shared

government research facility are of course not trivial. The proposed set up would require proper ventilation and a specialized chamber to remove all vapors from the environment after the measurements are run to avoid public exposure and to protect the equipment from cannabinoid residue. If successful, this type of experiment opens the door to real-time characterization of both liquid and vapor cannabinoid sensing, continuing the work explored in **Chapters 2** and **3** of my thesis, as well as previous work explored by my colleague Dr. Zachary Comeau. It could also be expanded to the sensing of other gases, such as ammonia,[12] which our lab has also explored in MPc-based OTFTs, or upon the development of other OTFT sensor platforms. We have been in discussions with the scientists at the Canadian Light Source to develop a suitable chamber for this type of vapor exposure and testing, and I hope to see this work carried out by my colleagues in the near future.

5.2.2 Integration of polymer dielectrics in MPc-based OTFT sensors to reduce operating voltage

One of the biggest challenges with the current MPc OTFT platform is the high operating voltage required to turn on and operate the devices. In a practical setting, operating a sensor at +/-50V is not ideal, and would require a significant power supply, which would add more equipment and mass to the final product. If we can reduce the operating voltage, we can reduce the overall footprint of the final consumer product. Members of our group have successfully integrated poly(methyl methacrylate)-based polymer dielectrics into devices with F_{10}-SiPc[13] and pentafluorostyrene-co-methyl methacrylate dielectrics into CuPc-based OTFTs[14], and there is current work to expand the library of MPcs used in these devices. It is important that the polymer dielectric used is compatible with the semiconductor. Poly(ionic liquids) (PILs), which make for high-performing dielectrics, have mobile counter ions which would need to be the opposite charge of the charges transported by the semiconductor in order to function and promote proper *p*- or *n*-type operation. Similarly, the electron donating or withdrawing behaviour should be considered based on the semiconductor type as well. As most MPc cannabinoid sensors have employed *p*-type materials like CuPc, ZnPc and Cl-AlPc, the polymers should be more electron withdrawing,[14,15] or could be PILs with negatively charged mobile counter ions to promote the negative polarization of the dielectric-

semiconductor interface,[16,17] and efficient transport of holes through the channel.

The reduction of the operating voltage upon integration of polymer dielectrics into these OTFT sensors could affect the analyte response by changing the operability region of the OTFT (linear vs saturation regime of the semiconductor). Additionally, the presence of an uneven, porous polymer film could affect analyte diffusion and retention within the device, its overall environmental stability, and its operational consistency. It will affect its interface properties, likely leading to a more amorphous semiconductor film, lower subthreshold slope (higher defect density), and lower overall μ, which has been seen in our group's previous work.[13,14] However, as demonstrated in **Chapter 2**, this lower baseline performance could be conducive to a higher sensor performance. A higher film porosity and roughness could promote analyte-semiconductor interactions on the film surface, and the amorphous nature of the film could allow for a greater degree of change in the film structure in response to analyte exposure. Our group's expertise both in polymer dielectric development and characterization, paired with our understanding of cannabinoid detection mechanisms and optimization, makes this project a logical next step for our group.

5.2.3 Addition of analyte reactive group to MPc *via* axial phenoxylation

To further the work explored in **Chapters 3** and **4**, the relatively simple axial phenoxylation strategy could be utilized to add a reactive group to any trivalent or tetravalent MPc to promote interactions between an analyte of interest and the MPc film. To continue with cannabinoid sensing, one could add a diazonium group to the molecule, which are known to react with cannabinoids through their phenol groups and is the basis for the colorimetric sensing dye, Fast Blue BB.[1] Since diazonium functional groups can be unstable, the phenoxylation would likely have to be performed using a nitrophenol[18] that would be converted to the diazophenol upon addition to the MPc. Other possible useful functional groups include hydrazines, which are aldehyde-reactive and would enable aldehyde sensing for multiple applications, like the detection of volatile aldehydes in blood samples for early tumor detection.[19–21] We have used a hydrazine-based probe in previous electrochemical sensor work (**Chapter 5**) that can react with aldehydes and simple ketones that could be easily modified and potentially axially substituted on a MPc that could be suitable for this work.

The addition of these reactive groups, while potentially increasing specificity of the sensing response, would likely come at the cost of electrical performance. The proposed phenol compounds are bulkier than the phenoxy groups tested in **Chapter 3**, which may impart a less efficient crystal packing on the thin film that may cause the OTFTs to be non-functional. The presence of a charged species on the molecule could also act as a charge trap, making charge transport difficult. A potential solution to this could be a mixed film (co-deposition or blend), with a small population of the reactive MPc mixed with a non-substituted MPc to minimize the charge trapping (**Figure 6.1a**). Alternatively, a bilayer device could be used, where a thin layer of the reactive MPc is deposited on top of a layer of unsubstituted MPc or another high-performing semiconductor. The top layer would interact directly with the analyte, and the bottom layer would act as the main charge transporting layer. Bilayer devices as described have been demonstrated previously to act as successful gas sensors,[22,23] but considerable effort has to be put toward optimizing the interface between the two layers to ensure efficient charge transport between them to maximize device sensitivity. A schematic of the proposed device structure is shown in **Figure 6.1b,** where the thin reactive layer is analyte-facing, and most charge transport occurs through the high-μ semiconductor beneath. The concept of bilayers for sensor applications is also used in organic heterojunction devices,[12] although often in reverse, where a low-mobility material is deposited underneath a material with a high charge density that is analyte-interfacing. Our group has experience optimizing physical vapor deposition parameters and characterizing thin film morphology through a variety of useful techniques, such as AFM, XRD and Raman. In this case, x-ray reflectivity (XRR) could be useful in this optimization process to characterize the interfacial roughness of the bilayers.

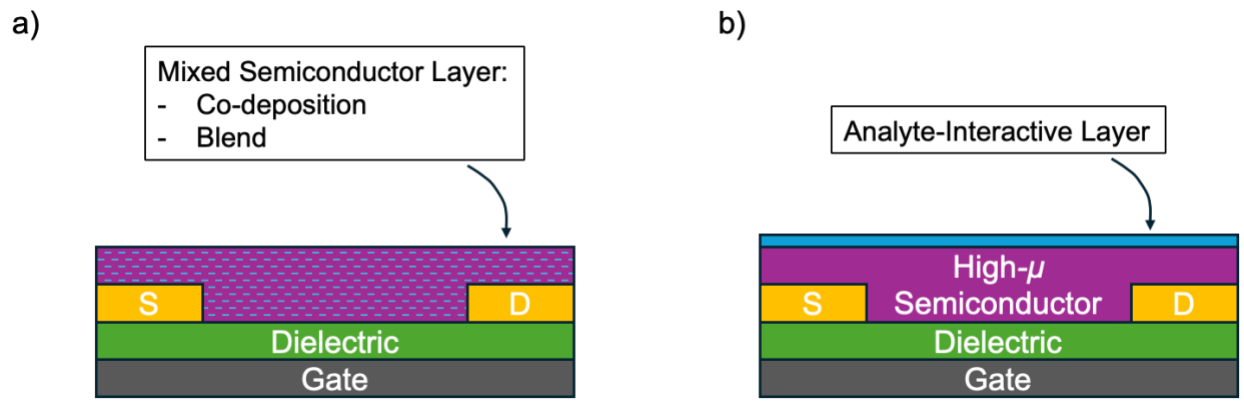

Figure 5.1. *Proposed device architectures for the incorporation of a reactive MPc in an OTFT sensor. a) mixed semiconductor layer from co-deposition or blending, and b) semiconductor bilayer with thin reactive MPc on the surface.*

Overall, these three proposed projects represent realistic and achievable steps forward to improve the performance and the commercialization potential of MPc-based sensors. Through *in-situ* film characterization, we can uncover the kinetics of film recrystallization during cannabinoid sensing, potentially helping to identify the mechanism for both the reversible and non-reversible sensing response observed by Comeau *et al.* (2022)[3] and advance commercialization efforts. The integration of polymer dielectrics will reduce operating voltage and allow for the use of lightweight substrates, while potentially improving the recyclability and degradability of the devices. This is especially important considering their single-use nature due to the irreversible sensing response observed thus far. Finally, the addition of axial reactive groups onto the MPc core could improve selectivity and sensitivity while widening the range of analytes sensed by this platform by tuning the reactive group to different functional groups of interest. Each of these advancements deepen our understanding of the sensing mechanisms at play in MPc-based OTFT sensors, while improving their appeal for the goal of sensor commercialization.

5.3 References

[1] Z. J. Comeau, N. T. Boileau, T. Lee, O. A. Melville, N. A. Rice, Y. Troung, C. S. Harris, B. H. Lessard, A. J. Shuhendler, *ACS Sens.* **2019**, *4*, 2706.

[2] Z. J. Comeau, N. A. Rice, C. S. Harris, A. J. Shuhendler, B. H. Lessard, *Adv. Funct. Mater.* **2022**, *32*, 2107138.

[3] Z. J. Comeau, R. R. Cranston, H. R. Lamontagne, C. S. Harris, A. J. Shuhendler, B. H. Lessard, *Commun Chem* **2022**, *5*, 1.

[4] Z. J. Comeau, G. A. Facey, C. S. Harris, A. J. Shuhendler, B. H. Lessard, *ACS Appl. Mater. Interfaces* **2020**, *12*, 50692.

[5] A. Tsumura, H. Koezuka, T. Ando, *Appl. Phys. Lett.* **1986**, *49*, 1210.

[6] C. G. Claessens, U. Hahn, T. Torres, *Chem. Rec.* **2008**, *8*, 75.

[7] B. H. Lessard, *ACS Appl Mater Interfaces* **2021**, *13*, 31321.

[8] Z. Xie, Y. Duan, M. Cheng, Y. Li, Z. Liu, H. Li, Y. Chen, Z. Zang, S. Liu, Q. Peng, *Angew. Chem. Int. Ed.* **2025**, *64*, e202419070.

[9] Z. Liang, Y. Zhang, H. Xu, W. Chen, B. Liu, J. Zhang, H. Zhang, Z. Wang, D.-H. Kang, J. Zeng, X. Gao, Q. Wang, H. Hu, H. Zhou, X. Cai, X. Tian, P. Reiss, B. Xu, T. Kirchartz, Z. Xiao, S. Dai, N.-G. Park, J. Ye, X. Pan, *Nature* **2023**, *624*, 557.

[10] R. Szostak, A. de Souza Gonçalves, J. N. de Freitas, P. E. Marchezi, F. L. de Araújo, H. C. N. Tolentino, M. F. Toney, F. das Chagas Marques, A. F. Nogueira, *Chem. Rev.* **2023**, *123*, 3160.

[11] A. H. Proppe, A. Johnston, S. Teale, A. Mahata, R. Quintero-Bermudez, E. H. Jung, L. Grater, T. Cui, T. Filleter, C.-Y. Kim, S. O. Kelley, F. De Angelis, E. H. Sargent, *Nat Commun* **2021**, *12*, 3472.

[12] B. King, S. G. Moorthy, E. Lesniewska, R. Meunier-Prest, M. Bouvet, B. H. Lessard, *Sens. Actuators B: Chem* **2024**, *408*, 135507.

[13] B. Ronnasi, B. King, S. Brixi, S. Swaraj, J. Niskanen, B. H. Lessard, *Adv. Electron. Mater.* **2024**, *10*, 2300810.

[14] A. J. Peltekoff, M. N. Tousignant, V. E. Hiller, O. A. Melville, B. H. Lessard, *Polymers* **2020**, *12*, 1231.

[15] L. Li, S. Liu, K. Wang, B. Wu, S. Zhang, *Macromol. Chem. Phys.* **2025**, *226*, 2400540.

[16] J. H. Cho, J. Lee, Y. Xia, B. Kim, Y. He, M. J. Renn, T. P. Lodge, C. Daniel Frisbie, *Nature Mater* **2008**, *7*, 900.

[17] L. Herlogsson, Y.-Y. Noh, N. Zhao, X. Crispin, H. Sirringhaus, M. Berggren, *Adv. Mater.* **2008**, *20*, 4708.

[18] H. Raboui, M. AL-Amar, A. I. Abdelrahman, T. P. Bender, *RSC Adv.* **2015**, *5*, 45731.

[19] M. Kusano, E. Mendez, K. G. Furton, *J. Forensic Sci.* **2013**, *58*, 29.

[20] A. H. Jalal, F. Alam, S. Roychoudhury, Y. Umasankar, N. Pala, S. Bhansali, *ACS Sens.* **2018**, *3*, 1246.

[21] Y. Wei, M. Wang, H. Liu, Y. Niu, S. Wang, F. Zhang, H. Liu, *J. Chromatogr. B* **2019**, *1118–1119*, 85.

[22] J. Huang, J. Miragliotta, A. Becknell, H. E. Katz, *J. Am. Chem. Soc.* **2007**, *129*, 9366.

[23] M. E. Roberts, A. N. Sokolov, Z. Bao, *J. Mater. Chem.* **2009**, *19*, 3351.

Chapter 6: Additional Work

My contributions in various additional published and ongoing projects are extensions of the techniques developed during my own cannabinoid OTFT sensor projects and highlight the versatility of my work and skillset. The work described encompasses a variety of materials, device platforms, and thin film characterization techniques, including advanced x-ray characterization techniques like GIWAXS, NEXAFS and STXM of both small molecule and polymer thin films, for applications in OTFTs and sensor platforms.

The various contributions can be classified generally into three categories, either involving thin-film morphological characterization, device fabrication through physical vapor deposition and subsequent OTFT characterization, or chemical and biological sensor development and characterization. During my graduate studies, I have been involved in two research trips to the Canadian Light Source for GIWAXS, two trips to Synchrotron SOLEIL for GIWAXS, and two trips to Synchrotron SOLEIL for NEXAFS/STXM. During these trips, I had the opportunity to learn these advanced techniques and collaborate on multiple projects within our group to run samples and interpret data for high-impact publications. My extensive experience in physical vapor deposition and OTFT characterization also led to frequent collaborations with group members to assist with these steps, particularly when chemists would make new molecules they would want to see integrated into new devices. Finally, my background in biochemistry and experience with sensor operation and characterization led to my consultation on various new sensor projects within our group. The work described herein illustrates my contributions to collaborative projects which have led to join peer reviewed journal publications.

6.1 Surface engineering of zinc phthalocyanine organic thin-film transistors results in part-per-billion sensitivity towards cannabinoid vapor

*Zachary J. Comeau, Rosemary R. Cranston, **Halynne R. Lamontagne**, Cory S. Harris, Adam J. Shuhendler & Benoît H. Lessard, Communications Chemistry, 2022, 5, 178*

DOI: 10.1038/s42004-022-00797-y

6.1.1 Abstract

Phthalocyanine-based organic thin-film transistors (OTFTs) have been demonstrated as sensors for a range of analytes, including cannabinoids, in both liquid and gas phases. Detection of the primary cannabinoids, Δ^9-tetrahydrocannabinol (THC) and cannabidiol (CBD), is necessary for quality control and regulation, however, current techniques are often not readily available for consumers, industry, and law-enforcement. The OTFT characteristics, X-ray diffraction (XRD) spectra, and grazing incident wide angle x-ray scattering (GIWAXS) spectra of two copper and three zinc phthalocyanines, with varying degrees of peripheral fluorination, were screened to determine sensitivity to THC vapor. Unsubstituted ZnPc was found to be the most sensitive material and, by tuning thin-film morphology, crystal polymorphs, and thickness through altered physical vapor deposition conditions, we increased the sensitivity to THC by 100x. Here we demonstrate that deposition conditions, and the resulting physical film characteristics, play a significant role in device sensitization.

6.1.2 Context and Contributions

I was involved in the device fabrication and GIWAXS data collection for this study, where we fabricated and optimized a sensor able to detect 40 ppb THC vapor. I also contributed to the manuscript editing.

6.2 Strong Magnetic Field Annealing for Improved Phthalocyanine Organic Thin-Film Transistors

Zachary J. Comeau, Rosemary R. Cranston, ***Halynne R. Lamontagne****, Adam J. Shuhendler & Benoît H. Lessard, Small, 2023, 19 (12), 2206792*
DOI: 10.1002/smll.202206792

6.2.1 Abstract

Thin-film microstructure, morphology, and polymorphism can be controlled and optimized to improve the performance of carbon-based electronics. Thermal or solvent vapor annealing are common post-deposition processing techniques; however, it can be difficult to control or destructive to the active layer or substrates. Here, the use of a static, strong magnetic field (SMF) as a non-destructive process for the improvement of phthalocyanine (Pc) thin-film microstructure, increasing organic thin-film transistor (OTFTs) mobility by twofold, is demonstrated. Grazing incident wide-angle X-ray scattering (GIWAXS), X-ray diffraction (XRD), and atomic force microscopy (AFM) elucidate the effect of SMF on both para- and diamagnetic Pc thin-films when subjected to a magnetic field. A SMF is found to increase the concentration of oxygen-induced radical species within the Pc thin-film, lending a paramagnetic character to ordinarily diamagnetic metal-free Pc and resulting in magnetic field induced changes to its thin-film microstructures. In a nitrogen environment, without competing degradation effects of molecular oxygen, SMF processing is found to favorably improve charge transport characteristics and increase OTFT mobility. Thus, post-deposition thin-film annealing with a magnetic field is presented as an alternative and promising technique for future thin-film engineering applications.

6.2.2 Context and Contributions

I was involved in device fabrication and GIWAXS data collection, where we were able to elucidate the influence of a strong magnetic field on device performance and thin film reorganization. I was also involved in manuscript editing.

6.3 Exposure to solvent vapours for enhanced *N*-type OTFT stability

Samantha Brixi, ***Halynne R. Lamontagne****, Benjamin King, Adam J. Shuhendler & Benoît H. Lessard, Materials Advances, 2023, 4, 4707-4711*

DOI: 10.1039/D3MA00402C

6.3.1 Abstract

To achieve commercialization of organic electronics, the field must see an improvement in both performance and material stability while maintaining a low cost of fabrication. To achieve this, low-cost additives provide a viable solution. A variety of additives containing amine and silane functional groups were tested to determine their impact on the performance and air-stability of *n*-type semiconductor poly{[*N*,*N*′-bis(2-octyldodecyl)-naphthalene-1,4,5,8-bis(dicarboximide)-2,6-diyl]-*alt*-5,5′-(2,2′-bithiophene) } (P(NDI2OD-T2)) in organic thin film transistors. Aniline and pyridine were found to both have a minimal impact on P(NDI2OD-T2) performance in an inert environment, but to improve stability of electron mobility and threshold voltage in air. Therefore, these compounds, or other compounds based on their structure, would be ideal candidates as additives for the improvement of *n*-type transistors.

6.3.2 Context and Contributions

I was involved in GIWAXS data collection for this study, to confirm that the resulting device performance was due to an interaction between the additives and semiconductor and not from a change in film morphology. I was also involved in manuscript editing.

6.4 Poly(2-vinylpyridine) as an Additive for Enhancing *N*-Type Organic Thin-Film Transistor Stability

Samantha Brixi, Chloé Dindault, Benjamin King, ***Halynne R. Lamontagne****, Adam J. Shuhendler, Sufal Swaraj & Benoît H. Lessard, Advanced Electronic Materials, 10 (2), 2300660*

DOI: 10.1002/aelm.202300660

6.4.1 Abstract

N-type organic semiconductors are particularly susceptible to degradation by ambient air. One such solution to this issue is to include additives in the inks these semiconductors would be cast from that would enhance device stability after film deposition. This method would reduce the number of processing steps needed to fabricate devices compared to other stabilization methods, such as encapsulation. In this study, the stabilization of *n*-type performance of the semiconductor poly{[N,N′-bis(2-octyldodecyl)-naphthalene-1,4,5,8-bis(dicarboximide)-2,6-diyl]-alt-5,5′-(2,29-bisthiophene)} (P(NDI2OD-T2)) when it is blended with an increasing proportion by weight of poly(2-vinylpyridine) (P2VP) is reported. The simple synthesis of P2VP also makes it an ideal candidate material for large-scale applications. Concentrations as low as 0.1% P2VP incorporated into the P(NDI2OD-T2) blends provided an immediate stabilization effect, and at 10% and 50%, longer-term stability after one week is observed.

6.4.2 Context and Contributions

I was involved in STXM data collection to generate composition maps through the film for different P2VP loadings, and GIWAXS data collection to characterize the influence of P2VP on the crystalline domains of P(NDI2OD-T2). I was also involved in manuscript editing.

6.5 Soluble zinc phthalocyanines as chemical probes for Δ-9-tetrahydrocannabinol in different solvents

*Laura Karlin, **Halynne R. Lamontagne**, Sumit Chaurasia, Michael Triglav, Cory S. Harris, Adam J. Shuhendler, Jaclyn L. Brusso & Benoît H. Lessard, Journal of Porphyrins and Phthalocyanines, 2024, 28 (6), 349-357*

DOI: 10.1142/S1088424624500081

6.5.1 Abstract

The detection of Δ-9-tetrahydrocannabinol (THC) is important for several applications from agriculture and pharmaceuticals to law enforcement. Two novel soluble zinc phthalocyanines were synthesized and their interaction with THC was studied. We report the change in the electrochemical and spectroelectrochemical response of the two zinc derivatives in the presence of THC using different organic solvents (DCM, THF, and DMF). The greatest change in spectroelectrochemical response was found when DCM was employed, whereas when THF was used an increase in higher energy π-π* transitions within the Pc cores was observed. Using DMF on the other hand demonstrated little change in response. We also found that the functional group used to solubilize the ZnPc played a significant role in the observed spectrochemical response to THC. These results demonstrate the potential for ZnPc-based chemical probes for the use in detection of THC.

6.5.2 Context and Contributions

LK was my undergraduate student, and I mentored her and guided the project through its completion and assisted in editing the manuscript. We received peripherally-modified ZnPc molecules from SC that were soluble in many organic solvents, allowing for extensive electrochemical and spectroelectrochemical characterization to investigate their interactions with THC and the influence of peripheral group and solvent on these interactions, as the performance of these molecules in OTFTs was found to be poor in separate, unpublished work.

6.6 Oxy Phosphorus Triazatetrabenzocorrole as a *p*-Type Organic Semiconductor in Organic Thin Film Transistors

*Mélanie Cyr, **Halynne R. Lamontagne**, Benoît H. Lessard & Jaclyn L. Brusso, ACS Applied Electronic Materials, 2024, 6 (8), 6275-6283*
DOI: 10.1021/acsaelm.4c01129

6.6.1 Abstract

Triazatetrabenzocorroles (Tbc) consist of a class of molecules derived from the phthalocyanine and porphyrin families that are less commonly synthesized and utilized in applications for organic electronics. In this work, we have synthesized oxy phosphorus Tbc (POTbc) and integrated it as an organic semiconductor in organic thin film transistors (OTFTs). Both bottom-gate bottom-contact (BGBC) and bottom-gate top-contact (BGTC) OTFTs fabricated with POTbc resulted in a clear *p*-type performance both in air and under inert conditions. A series of solution-based silanes and thermally evaporated *p*-sexiphenylene were utilized as dielectric surface treatments as a means to modify the surface energy of the dielectric surface prior to depositing the POTbc thin films. Other fabrication conditions were also explored, such as deposition rate of POTbc, substrate surface temperature during deposition, and post-deposition annealing. Of these, optimized POTbc-based OTFTs were obtained from *n*-octadecyltrichlorosilane (ODTS)-coated substrates, with a heated deposition, which afforded an average field effect mobility of 8.18×10^{-3} $cm^2 V^{-1} s^{-1}$ and a threshold voltage of −23.2 V. X-ray diffraction and polarized Raman microscopy indicated a significant increase in the POTbc film crystallinity and a film morphology with a more molecular face-on configuration when deposited on ODTS-treated surfaces. These results represent the first report of OTFTs fabricated using POTbc, including structure–property relationships related to thin film optimization and device performance.

6.6.2 Context and Contributions

I assisted with device fabrication through PVD of POtbc on various surface-treated substrates, and the subsequent electrical characterization of the OTFTs. I also performed the polarized Raman microscopy to determine the orientation of the molecules to relate thin film morphology to electrical performance and assisted in manuscript preparation.

6.7 High Throughput Characterization of Organic Thin Film Transistors

Nicholas Dallaire, Nicholas T. Boileau, Ian Myers, Samantha Brixi, May Ourabi, Ewenike Raluchukwu, Rosemary Cranston, ***Halynne R. Lamontagne****, Benjamin King, Bahar Ronnasi, Owen A. Melville, Joseph G. Manion, Benoît H. Lessard, Advanced Materials, 2024, 36 (44), 2406105*

DOI: 10.1002/adma.202406105

6.7.1 Abstract

Automation is vital to accelerating research. In recent years, the application of self-driving labs to materials discovery and device optimization has highlighted many benefits and challenges inherent to these new technologies. Successful automated workflows offer tangible benefits to fundamental science and industrial scale-up by significantly increasing productivity and reproducibility all while enabling entirely new types of experiments. However, it's implementation is often time-consuming and cost-prohibitive and necessitates establishing multidisciplinary teams that bring together domain-specific knowledge with specific skillsets in computer science and engineering. This perspective article provides a comprehensive overview of how the research group has adopted “hybrid automation” over the last 8 years by using simple automatic electrical testers (autotesters) as a tool to increase productivity and enhance reproducibility in organic thin film transistor (OTFT) research. From wearable and stretchable electronics to next-generation sensors and displays, OTFTs have the potential to be a key technology that will enable new applications from health to aerospace. The combination of materials chemistry, device manufacturing, thin film characterization and electrical engineering makes OTFT research challenging due to the large parameter space created by both diverse material roles and device architectures. Consequently, this research stands to benefit enormously from automation. By leveraging the multidisciplinary team and taking a user-centered design approach in the design and continued improvement of the autotesters, the group has meaningfully increased productivity, explored research avenues impossible with traditional workflows, and developed as scientists and engineers capable of effectively designing and leveraging automation to build the future of their fields to encourage this approach, the files for replicating the infrastructure are included, and questions and potential collaborations are welcomed.

6.7.2 Context and Contributions

This paper was a collaborative and multi-year effort that involved the expertise and input of every graduate student who has fabricated, tested, and characterized OTFTs in our group since its inception. As such, I contributed my experiences in OTFT and sensor fabrication to the manuscript preparation and editing process.

6.8 Engineering the Template Layer for Silicon Phthalocyanine-Based Organic Thin Film Transistors

Raluchukwu B. Ewenike, Zheng Sonia Lin, Rosemary R. Cranston, ***Halynne R. Lamontagne****, Adam J. Shuhendler, Chang-Hyun Kim, Jaclyn L. Brusso, Benoît H. Lessard, Advanced Functional Materials, 2024, 34 (48), 2408779*

DOI: 10.1002/adfm.202408779

6.8.1 Abstract

Multi-phenyl and multi-thiophene rod-like molecules are typically used for weak epitaxial growth (WEG) of highly ordered organic semiconductor films enabling controllable microstructure properties and improved device performance. However, very few templating molecules have been reported, making it challenging to establish structure-property relationships. As semiconductors are integrated into organic thin film transistors (OTFTs), the impact of templating layers on semiconductor microstructure and device performance must be established. Herein, four aromatic molecules with similar structure to para-sexiphenyl (*p*-6P) are synthesized and incorporated as the template layer in bis (pentafluoro phenoxy) silicon phthalocyanine (F_{10}-SiPc) OTFTs. The use of fluorinated *p*-6P (*p*-6PF) yields devices with the highest electron field-effect mobility of 0.14 $cm^2 V^{-1} s^{-1}$ while a partially fluorinated *p*-6P (*p*-6PF_4) results in improved threshold voltage. X-ray diffraction (XRD) demonstrates varying F_{10}-SiPc crystallinity with choice of templating layer with the most crystalline films resulting from the use of *p*-6PF. By grazing incidence wide angle X-ray scattering (GIWAXS) and polarized Raman microscopy, all templating layers yield films with F_{10}-SiPc molecules predominantly aligned face-on to the substrate. However, rod-like *p*-6P derivatives increased the face-on orientation of F_{10}-SiPc. This study highlights the importance of template layer selection and deposition optimization in WEG-based OTFTs.

6.8.2 Context and Contributions

I was involved in GIWAXS data collection and interpretation, where we compared the degree of crystallinity and molecular orientation of F_{10}-SiPc on different templating layers and related the thin film microstructure to the device performance. I also assisted with manuscript preparation and editing.

6.9 Monitoring ketoacidosis and ketosis through electrochemical sensing of acetone and acetoacetate in biological fluids after dilution

Ahmed A. Khorshed, ***Halynne R. Lamontagne****, Lauren Healy, Adam J. Shuhendler, Benoît H. Lessard, Sensors and Actuators B: Chemical, 2025, 433, 137557*
DOI: 10.1016/j.snb.2025.137557

6.9.1 Abstract

The detection and monitoring of ketone metabolic markers is essential to accurately diagnose ketoacidosis in diabetic patients, safely manage ketogenic diets, and reduce complications associated with ketosis. There is a need for low-cost point-of-use sensors which can accurately monitor ketone bodies (including acetoacetate, acetone, and β-hydroxybutyrate) in biological fluids with minimal sample handling. In this study, we developed an electrochemical sensor for the detection of two ketone bodies, acetone and acetoacetate, using square wave voltammetry with bare/unmodified screen-printed carbon electrodes (SPCEs). This method involves direct electrochemical oxidation after derivatization with 2-hydrazinobenzoic acid as an electrochemical probe, eliminating the need for enzymes as recognition elements and thus providing enhanced long-term stability for the sensor. While acetone and acetoacetate lack inherent electrochemical activity, they generate a new peak upon reacting with the probe, indicating the formation of hydrazone derivatives corresponding to each ketone body. The method exhibits excellent linearity over a concentration range of 0.125 – 1.25 mM, with limits of detection of 0.034 mM for acetone and 0.037 mM for acetoacetate. The proposed voltammetric method was successfully applied to the detection of acetone in spiked artificial saliva and acetoacetate in spiked rat urine samples, without significant interference from the sample matrices. The reaction mechanism between the probe and the ketone bodies was further confirmed using liquid chromatography-mass spectrometry (LC-MS). These results represent a significant step forward towards the monitoring of ketone bodies through the use of low-cost, point-of-use sensors.

6.9.2 Context and Contributions

I had demonstrated the usefulness of the 2-hydrazinobenzoic acid probe to detect ketone bodies in previous unpublished electrochemical and UV-vis experiments, which

laid the groundwork for the expansion of this project to the use of electrochemical-based sensors for ketone body detection. I assisted AAK in the development of the baseline reaction procedure for the probe with the ketone body, and assisted with manuscript editing.

6.10 Operational and Environmental Stability Assessment of Silicon and Copper Phthalocyanine-based OTFTs

Nicholas Dallaire, Joon Hyung Park, Raluchukwu Ewenike, ***Halynne R. Lamontagne****, Chang-Hyun Kim and Benoît H. Lessard*, *Small Methods, 2025, Under Review*

6.10.1 Abstract

When developing new materials for organic electronics it is critical to understand how these devices will perform over time and how changes in molecular structure will influence their degradation in performance. Environmental stability is often assessed by exposing devices to an environment while testing at regular intervals, whereas bias stress is often assessed by constant current application. These techniques do not provide a complete assessment of the materials' performance in applications which involve multiple charging and discharging steps. In this study we developed a cycling approach which provides statistically significant evaluation of four different semiconductors in organic thin film transistors (OTFT) and quantified the effect of both operational and environmental stress on their performance. We characterized OTFTs using an in-house built automated tester for 48-72 hours straight in air and in N_2. We demonstrate that the structure of the phthalocyanine leads to significant differences in response to bias stress, such as F_{10}-SiPc showing much more air-stable *p*-type device compared to CuPc and $(F_5PhO)_2$-F_{16}-SiPc showing much more air-stable *n*-type performance compared to F_{16}-CuPc. Raman microscopy of the films revealed that no changes in morphology resulted from the stress testing. We also modelled our devices using the two-dimensional (2D) finite-element method which suggests that most of the changes in device performance are due to the traps near the semiconductor/insulator interface. Overall, we demonstrated by OTFT stress testing that important structure property relationships can be established between semiconductor molecular structure and device performance.

6.10.2 Context and Contributions

I performed the device fabrication by PVD for the $(F_5PhO)_2$-F_{16}-SiPc and CuPc based OTFTs. I also assisted in the Raman characterization of the films to determine the effect of long-term electrical testing and oxygen exposure and assisted in manuscript editing.

6.11 When Siloxane Meets Silicon Phthalocyanine: an Original Phthalocyanine Design to Achieve a Hole Mobility Over 1 $cm^2 V^{-1} s^{-1}$

Nicolas Ledos, ***Halynne R. Lamontagne****, Joseph Manion, Jaclyn Brusso, Benoît H. Lessard, 2025, Under Review*

6.11.1 Abstract

Phthalocyanines are widely used in organic electronics due to their excellent chemical stability and tunable electronic properties, but their synthesis and purification often present significant challenges due to their low solubility. We report an alternative synthesis for a siloxane-substituted silicon phthalocyanine ($^{iso}(Si_3O)_2SiPc$) and demonstrate its integration as an active semiconducting material in organic thin-film transistors (OTFTs). This compound is easily synthesized and purified, exhibits high solubility, and achieves a hole mobility exceeding 1 $cm^2 V^{-1} s^{-1}$ under ambient conditions, a record high mobility for silicon phthalocyanines (SiPcs). Moreover, SiPcs usually behave as *n*-type semiconductors and $^{iso}(Si_3O)_2SiPc$ unexpectedly displays a unipolar p-type character. The semiconducting behavior was investigated through a combination of density functional theory (DFT) calculations and experimental characterization of thin-film transistors. In particular, the investigation using GIWAXS revealed the high degree of crystallinity with an exceptionally uniform crystalline texture of $^{iso}(Si_3O)_2SiPc$ thin film, supporting efficient charge transport and demonstrating the material's strong potential for high-performance OTFT applications. These results highlight the importance of siloxane based functional groups as an effective strategy to develop high performance, conjugated small molecule based OTFTs.

6.11.2 Context and Contributions

I assisted NL in the fabrication of a set of OTFTs based on $^{iso}(Si_3O)_2SiPc$, with different surface treatments and annealing temperatures. I also assisted in GIWAXS data collection and interpretation, where we were able to demonstrate that the top-performing devices reaching mobilities over 1 $cm^2 V^{-1} s^{-1}$ had molecules that were singularly oriented throughout the film in large, layered sheets. This is an impressive level of order for a tetravalent small molecule, and contributes to its high performance and stability.

6.12 Direct Measurement of Density for Evaporated Thin Films

Trevor Plint, ***Halynne R. Lamontagne****, Joseph Manion, Benoît H. Lessard, 2025, Manuscript Submitted*

6.12.1 Abstract

We report a simple and elegant method for direct measurement of the density of vapor deposited thin films using a combination of profilometry, microscopy, and high-vacuum thermogravimetric analysis (TGA). Density affects fabrication control, optical properties, charge transport, and mechanical properties of thin film devices. Accurate density determination is essential for optimizing device design to ensure film stability, charge balance, and light-matter interactions. Exact mass of the vapor deposited thin films with suitable mass and aspect ratio was determined by high-vacuum TGA. Combined with precise measurements of thickness and area for each film, we captured the true density of individual films as deposited. This method avoids common universalizing assumptions about the degree of crystallinity in a film. Furthermore, this method does not depend on bulk optical or electrical parameters that may vary as a result of the unique nanoscale properties of thin films. We report density values for a range of small molecule semiconductors commonly found in organic electronics such as organic light emitting diodes (OLEDs), organic photovoltaics (OPVs), and organic thin film transistors (OTFTs), and compare them to values calculated by other means. We anticipate that this technique can be used to measure the density of a wide range of vacuum stable thin film materials.

6.12.2 Context and Contributions

In this study, I utilized my extensive PVD experience to assist TP in developing a procedure to fabricate a film of sufficient mass to obtain an accurate trace by thermogravimetric analysis (TGA), while mimicking the deposition conditions experienced in both industrial and academic PVD systems (high and low deposition rates). I also assisted in the microscope imaging of the resulting film, which allowed us to calculate an accurate film area, which when combined with profilometry and TGA, allowed for the determination of film density. This described method does not rely on theoretical calculations, and is a more direct calculation of an important thin-film property.

6.13 Silicon Phthalocyanine-based N-Type Organic Mixed Ionic-Electronic Conductor in Organic Electrochemical Transistors

May Ourabi, Mario C. Vebber, Mélanie Cyr, Forest St-Denis Weintrager, Nicolas Ledos, ***Halynne R. Lamontagne****, Audithya Nyayachavadi, Benoît H. Lessard, Journal of Materials Chemistry C, 2025, Advance Article*

DOI: 10.1039/D5TC02130H

6.13.1 Abstract

Phthalocyanines have evolved from their early role as dyes and pigments into a versatile class of small-molecule semiconductors used in thin-film electronics, including organic photovoltaics and thin-film transistors. Using a silicon phthalocyanine with hydrophilic (2-[2-(2-methoxyethoxy)ethoxy]acetate) axial substitutions, we report the first application of phthalocyanine films as an *n*-type organic mixed ionic-electronic conductor material in organic electrochemical transistors. The devices demonstrate a figure of merit (μC^*) of 0.011 F $cm^{-1}V^{-1}s^{-1}$, volumetric capacitance (C^*) of 79.3 F cm^{-3} and resulting charge mobility (μ) of 1.4 x 10^{-4} cm^2 $V^{-1}s^{-1}$. Characterization of the films using atomic force microscopy and Raman spectroscopy points towards a rearrangement of the thin films post-swelling, which ultimately results in poor cycling stability. Nonetheless, this application broadens the use of phthalocyanines and enlarges the library of organic mixed ionic-electronic conductors to include this inexpensive and biocompatible material.

6.12.2 Context and Contributions

In this study, I assisted in the XRD and GIWAXS analysis and data workup for the PEG-SiPc on different substrates to determine its influence on the final orientation of the film, and its impact on charge transport. I also assisted with the editing of the final manuscript.

Copyright Permissions

Chapter 2:

Reproduced from:

Chloro aluminum phthalocyanine-based organic thin-film transistors as cannabinoid sensors: engineering the thin film response. H. R. Lamontagne, Z. J. Comeau, R. R. Cranston, N. T. Boileau, C. S. Harris, A. J. Shuhendler and B. H. Lessard, *Sens. Diagn.*, 2022, **1**, 1165 **DOI:** 10.1039/D2SD00071G

With permission from the Royal Society of Chemistry (2022)

Chapter 3:

Reproduced from:

Axial Phenoxylation of Aluminum Phthalocyanines for Improved Cannabinoid Sensitivity in OTFT Sensors. H. R. Lamontagne, R. R. Cranston, Z. J. Comeau, C.S. Harris, A. J. Shuhendler, B. H. Lessard, *Adv. Sci.*, 2024, **11** (27), 2305515 **DOI:** 10.1002/advs.202305515

With permission from Wiley-VCH GmbH (2024)

Chapter 4:

Reproduced from:

$(F_5PhO)_2$-F_{16}-SiPc as an air-stable, high-performance n-type semiconductor with poor cannabinoid sensing capabilities. H. R. Lamontagne, M. Cyr, M. C. Vebber, S. Swaraj, C. S. Harris, J. L. Brusso, A. J. Shuhendler and B. H. Lessard, *RSC Appl. Interfaces*, 2024, **1**, 1222 **DOI:** 10.1039/D4LF00147H

With permission from the Royal Society of Chemistry (2024)